Technical Physics Letters, Vol. 27, No. 9, 2001, pp. 709–711. Translated from Pis'ma v Zhurnal Tekhnicheskoĭ Fiziki, Vol. 27, No. 17, 2001, pp. 1–6.

Particularities of the Photoluminescence Spectra of Cr^{4+}:Ca_2GeO_4 Single Crystal Films

O. N. Gorshkov, E. M. Dianov, N. B. Zvonkov, A. P. Kasatkin, V. F. Lebedev, G. A. Maksimov, A. B. Chigineva, and Yu. I. Chigirinskii

Physicotechnical Research Institute, Nizhni Novgorod State University, Nizhni Novgorod, Russia
Scientific Center for Fiber Optics, Institute of General Physics, Russian Academy of Sciences, Moscow, Russia
e-mail: lab10@phys.unn.runnet.ru

Received January 23, 2001

Abstract—It was found that the room-temperature photoluminescence (PL) spectra of Cr^{4+}:Ca_2GeO_4 single crystal films grown by magnetron sputtering on Ca_2GeO_4 bulk single crystal substrates exhibit a sharp emission band in the region of ~1.17 μm with satellites at ~1.21 and 1.27 μm. Particularities of the PL spectra are interpreted within the framework of a model based on the interaction between electrons of the Cr^{4+} center and the oscillations excited in the film. © *2001 MAIK "Nauka/Interperiodica".*

Optical materials doped with chromium in the Cr^{4+} state attract the attention of researchers as a means of generating laser radiation in a wavelength interval from 1.2 to 1.5 μm, a promising range for fiber optic communication lines. Of special interest from the standpoint of creating integrated optical devices is obtaining such materials in the form of films.

Recently [1], we reported on the synthesis of X-ray-amorphous Cr^{4+}:Ca_2GeO_4 films grown by magnetron sputtering on fused quartz substrates. It was demonstrated that the room-temperature photoluminescence (PL) spectrum of these films contains a broad emission band in the region of ~1.3 μm, which virtually coincides with the PL band of Cr^{4+}:Ca_2GeO_4 bulk single crystals measured at the same temperature [2].

Below, we will discuss particularities of the PL spectra of Cr^{4+}:Ca_2GeO_4 single crystal films grown by magnetron sputtering on (110)-oriented calcium germanate (Ca_2GeO_4) bulk single crystal substrates. The film deposition and formation conditions were the same as those used in the synthesis of films on fused quartz substrates (see [1]). The film structure was studied by X-ray diffraction on a DRON-3 diffractometer operating in a "glancing beam" geometry. An analysis of the X-ray diffraction patterns showed that the samples represent single crystal films. The crystal lattice mismatch between film and substrate, determined from an analysis of the X-ray rocking curve, amounted to 5×10^{-4} nm.

The PL spectra were excited at λ = 980 nm by a diode laser operating at an output power of 1 W. The room-temperature PL spectra of the single crystal films (see figure, curve *1*) exhibit a sharp emission band in the region of $\lambda_1 \sim 1.17$ μm with satellites at $\lambda_2 \sim 1.21$ and $\lambda_3 \sim 1.27$ μm. Similar spectra are observed from Cr^{4+}:Ca_2GeO_4 bulk single crystals possessing an olivine structure measured at liquid nitrogen temperature (see figure, curves *3* and *4*) and from Cr^{4+}:Mg_2SiO_4 (forsterite) crystals measured at 10 K [3]. These PL spectra correspond to electron transitions from an excited $^3A_1$ state to $^3A_2$ ground state of a Cr^{4+} center in a distorted tetrahedral crystal field [3]. It should be noted that the room-temperature PL spectrum of a Cr^{4+}:Ca_2GeO_4 bulk single crystal (see inset in the figure and the corresponding spectrum in [2]) appears as a broad band with a maximum at $\lambda_3 \sim 1.25$ μm.

The PL spectra of Cr^{4+}:Ca_2GeO_4 single crystal films exhibit the flowing special features: (i) the frequency of oscillations determined as a mean value for the first and second satellites ($\nu \sim 337$ cm^{-1}) exceeds the analogous values determined for the bulk single crystals of Cr^{4+}:Ca_2GeO_4 ($\nu \sim 132$ cm^{-1}) and Cr^{4+}:Mg_2SiO_4 ($\nu \sim 153$ cm^{-1}) [3]; (ii) the PL spectra of the films display an additional peak situated on a shortwave wing of the sharp band; (iii) the most intense band in the PL spectrum of the film is shifted by ~30 nm toward shorter wavelengths relative to the analogous band in the spectra of bulk single crystals; (iv) the PL spectrum of the film shows relatively weak satellites with $\nu \sim 700$ cm^{-1}, which are more pronounced in the spectra of bulk samples [3, 4]; (v) as the temperature increases from 77 to 300 K, the sharp emission band in the spectrum of the film broadens without any significant change in the position of maximum or in the shape (cf. figure, curves *1* and *2*).

The PL spectra of the bulk single crystals of Cr^{4+}:Ca_2GeO_4 and Cr^{4+}:Mg_2SiO_4 were interpreted [2–4] within the framework of a model based on the interaction of electrons of the Cr^{4+} center with the local oscil-

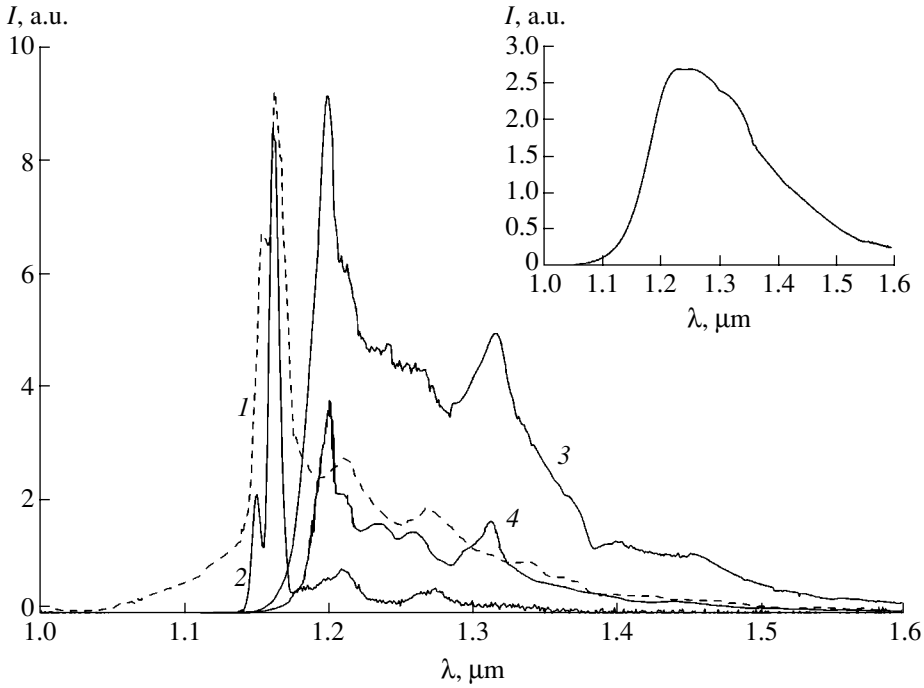

The PL spectra of Cr^{4+}:Ca_2GeO_4: (*1*, *2*) singe crystal films deposited onto (110)-oriented Ca_2GeO_4 bulk single crystal substrate, measured at room temperature and at liquid nitrogen temperature, respectively; (*3*, *4*) bulk single crystals measured at liquid nitrogen temperature in this work and in [2], respectively. The inset shows the room-temperature PL spectrum of the bulk single crystal.

lations of this center and the optical modes of the crystal lattice [5–7]. This interaction is characterized by the Juan–Reece factor S describing a partial conversion of the energy liberated upon the electron transition into the energy of local oscillations or lattice modes. This parameter can be determined using the experimental ratio of the areas of the first satellite and the narrow band (the so-called phononless band). In this model, the transformation of the spectrum with a fine structure (containing both the phononless band and the satellites) to the broad-band spectrum is characterized by the parameter $a = (S/2)\coth(\nu/2kT)$, where ν is the frequency of oscillations excited by the center (determined by the positions of satellites), k is the Boltzmann constant, and T is the absolute temperature. For the transition under consideration, the a value varies from $a \ll 1$ to $a \gg 1$.

In our case, the Juan–Reece factor for $\nu = 337$ cm^{-1} is $S = 0.2$ and the room-temperature value of a is 0.3, which corresponds to the spectrum with a fine structure (this structure is favored by high ν values). According to [3], the bulk single crystals of Cr^{4+}:Mg_2SiO_4 measured at 10 K are characterized by $S = 0.7$. Assuming this factor to depend weakly on the temperature, we obtain $a = 2.2$ for $\nu = 153$ cm^{-1} at room temperature. For Cr^{4+}:Ca_2GeO_4 *a* bulk single crystals measured at liquid nitrogen temperature the spectrum yields a estimate of $S = 0.4$. Making analogous assumptions for S and $\nu = 132$ cm^{-1}, we obtain the room-temperature estimate $a = 1.4$. Thus, the room-temperature parameter a for single crystal films is significantly smaller than the analogous values for the bulk single crystals of Cr^{4+}:Mg_2SiO_4 and Cr^{4+}:Ca_2GeO_4.

In the analysis of factors responsible for the appearance of oscillations with $\nu = 337$ cm^{-1}, we must note that the energy of the crystal lattice oscillations in a bulk single crystal of Ca_2GeO_4 [4] is usually characterized by $\nu \sim 200$ cm^{-1}. In our case, the formation of Cr^{4+}:Ca_2GeO_4 films takes place at a temperature of 450–500°C, which is markedly lower as compared to the temperatures involved in the synthesis of bulk single crystals (e.g., the melt temperature in the Czochralski process for the olivine phase of Ca_2GeO_4 is 1410–1490°C [8]). Therefore, we may expect that the crystal structure of our films is characterized by a considerable density of defects which, in turn, may lead to modification of their phonon spectrum toward increasing frequency of the optical modes. The natural question as to whether such a modification can result in the appearance of a mode with $\nu \sim 337$ cm^{-1} in the phonon spectrum—or whether the observed oscillations should be attributed to oscillations of the Cr^{4+} center—requires additional investigation.

The presence of crystal lattice defects may also account for the observed shortwave shift of the phononless band in the PL spectrum of the film relative to that in the spectrum of the bulk crystal. The optical characteristics of the Cr^{4+} ion are determined by the tetrahedral symmetry of the nearest (oxygen) crystalline envi-

ronment, by the tetrahedral crystal field strength, and by distortions of the tetrahedral symmetry. The presence of defects in the films studied can be manifested by the aforementioned increase in the crystal lattice parameter of the film, resulting in a greater strength of the crystal field corresponding to the tetrahedral environment and in lower distortions of the tetrahedral symmetry. Both these factors may lead to the observed increase in energy of the electron transitions studied.

The above interpretation of particularities of the luminescence spectra of Cr^{4+}:Ca_2GeO_4 single crystal films is not the only possible variant. An alternative explanation can be given proceeding from an assumption that other crystalline phases present in the films [8] account for the appearance of the observed spectral features. However, it should be noted that the X-ray diffraction analysis of the single crystal film samples revealed the presence of a single olivine phase.

Thus, we have experimentally demonstrated for the first time that Cr^{4+}:Ca_2GeO_4 single crystal films feature a weak energy exchange between electrons of the Cr^{4+} center and oscillations excited in the film at room temperature, which leads to a fine structure of the optical emission spectrum.

Acknowledgments. The authors are grateful to T.T. Basiev for fruitful discussions of the results and to V. Petrisevich for indicating the possibility of an alternative explanation of the features observed in the PL spectra of the films, based on the presence of some other phases in the samples. Many thanks go to V.N. Trushin for conducting the X-ray diffraction measurements and to V.V. Dozmarov for kindly providing the plates of Ca_2GeO_4 and Cr^{4+}:Ca_2GeO_4 bulk single crystals for the investigation.

REFERENCES

1. O. N. Gorshkov, E. M. Dianov, N. B. Zvonkov, *et al.*, Kvantovaya Élektron. (Moscow) **30** (3), 261 (2000).
2. V. Petricevic, A. B. Bykov, J. M. Evans, *et al.*, Opt. Lett. **21** (21), 1750 (1996).
3. W. Jia, H. Liu, S. Jaffe, *et al.*, Phys. Rev. B **43** (7), 5234 (1991).
4. M. F. Hazenkamp, H. U. Gudel, M. Atanasov, *et al.*, Phys. Rev. B **53** (5), 2367 (1996).
5. S. I. Pekar, Zh. Éksp. Teor. Fiz. **20** (6), 510 (1950).
6. K. Huang and A. Rhys, Proc. R. Soc. London, Ser. A **204** (1076), 406 (1950).
7. Yu. E. Perlin and B. S. Tsukerblat, *The Effects of Electron-Phonon Interaction in Optical Spectra of Paramagnetic Impurity Ions* (Shtiintsa, Kishinev, 1974).
8. A. K. Shirvinskaya, R. G. Grebenshchikov, and N. A. Toropov, Izv. Akad. Nauk SSSR, Neorg. Mater. **2** (2), 332 (1966).

Translated by P. Pozdeev

Technical Physics Letters, Vol. 27, No. 9, 2001, pp. 712–715. Translated from Pis'ma v Zhurnal Tekhnicheskoĭ Fiziki, Vol. 27, No. 17, 2001, pp. 7–15.

A Discharge with Runaway Electrons: Efficient Process for the Formation of Rydberg States in Oxygen Molecules

V. V. Ivanov, T. V. Rakhimova, and K. V. Savost'yanov

Research Institute of Nuclear Physics, Moscow State University, Moscow, Russia

e-mail: rtv@mics.msu.ru

Received February 20, 2001

Abstract—A new method for exciting high-lying states in oxygen molecules is proposed, which is based on the interaction of O_2 molecules with a low-energy (~10^2–10^4 eV) electron beam formed in a discharge with runaway electrons. An algorithm for calculating the electron energy distribution function (EEDF) using the Monte Carlo simulation technique is developed. The EEDF calculation for a discharge in pure oxygen is performed for a plasma pumped with monoenergetic electron beam in the absence of an external electric field. Efficiencies of the formation of Rydberg and Herzberg states in oxygen molecules under conditions of a quasi-stationary dc discharge and a discharge with runaway electrons are compared. © *2001 MAIK "Nauka/Interperiodica".*

Introduction. Electronegative gas plasmas are widely employed in various modern technologies. Investigation of the mechanisms of formation and loss of negative ions is an important part in the study of bulk and surface processes occurring in the plasma reactors. Some recent experimental investigations [1–5] revealed increased concentrations of negative ions in the afterglow of pulsed dc and ac discharges in electronegative ions, in particular, in oxygen [1–3].

The negative ion formation in the afterglow is related to the process of thresholdless dissociative low-energy electron attachment to highly excited molecules formed in the discharge via the reaction

$$e^- + O_2^* \longrightarrow O^- + O.$$

At a reduced pressure (~10–10^2 Pa) typical of the discharges studied in [1–3], the formation of negative ions is possible only by the mechanism of dissociative electron attachment to oxygen molecules, since triple collisions are not very probable. The electron attachment to the ground and lower metastable states is characterized by a small cross section (~2×10^{-22} m^2) and a high energy threshold (~4 eV).

An analysis of the experimental data obtained by Ding *et al.* [1] indicates that the excited oxygen molecules (O_2^*) occur either in the Rydberg states O_2^*(Ry) with excitation energies $E \sim 9.7$–12 eV [2–3] or in the Herzberg states ($C^3\Delta_u$, $A^3\Sigma_u^+$, $c^1\Sigma_u^-$) with $E \sim 4.5$ eV. In connection this context, it was interesting to perform an experiment in which dominating role of the Rydberg or Herzberg states would allow us to compare their roles in the process of negative ion formation.

We may propose an alternative to using discharge as a method for exciting the high-lying O_2^* levels, which consists in acting upon the gas with a beam of fast electrons. Using traditional electron guns (operating in the energy range from ~10^5 to 10^7 eV) for this purpose does not seem to be expedient because the ionization and excitation cross sections in the high-energy range are small. An electron beam of lower energy (~10^2–10^4) can be obtained using a discharge gap with a perforated electrode [6] called the open discharge gap [7]. The electron beam formation under the open discharge conditions is analogous to the process taking place in the cathode region of a glow discharge. In an open discharge, the electron beam forms in the space between cathode and grid electrode. A considerable proportion of the so-called runaway electrons accelerated in a strong field of the confined discharge leave this space through the grid holes. The region behind the grid is called the drift space.

The purpose of this study was to compare the efficiency of excitation of the Herzberg and Rydberg states in oxygen molecules by a constant electric field of the positive column of a glow discharge to the efficiency of excitation of the same states by an electron beam in the drift space of an open discharge. The comparison was based on the Monte Carlo calculation of the electron energy distribution functions in the two cases of interest.

Problem formulation. A stationary self-consistent field in the discharge is determined by a balance of the electron generation and loss processes. It was reported [1] that negative ions formed in the afterglow stage of a quasi-stationary dc discharge in pure oxygen. The electron temperature in the discharge measured by a probing technique was ~2 eV. According to the results of calculations performed in a two-term approximation [8], this

1063-7850/01/2709-0712$21.00

temperature value corresponds to a field strength of $E/N \sim 4 \times 10^{-16}$ V m^2. Estimates showed that the loss of electrons in the course of dissipative attachment can be compensated neither by ionization (the ionization rate constant is as small as $k_i \sim 10^{-20}$ m^3/s) nor by detachment, since the concentrations of $O_2(a^1\Delta_g)$ and $O(^3P)$ states (involved in the detachment) are small under the experimental conditions studied. Moreover, the rate constant of excitation of the Rydberg states in oxygen exposed to a weak electric field ($E/N \sim 4 \times 10^{-16}$ V m^2) is very small, being several orders of magnitude lower than that for the Herzberg states. The possibility of exciting the Rydberg states in oxygen molecules and the discrepancy between measured electron temperatures and the steady-state discharge operation observed in [1] can be explained by a significantly nonlocal character of the electron energy spectrum related to the influence of near-electrode plasma layers. The role of this factor in the formation of negative ions can be assessed based on the EEDF calculation by the Monte Carlo method.

We employed the Monte Carlo simulation technique for calculating the electron energy distribution function $f(x, \varepsilon)$ in the open-discharge plasma in oxygen pumped with a monoenergetic electron beam in the absence of external electric fields in the drift space.

Calculation procedure. The calculation of the electron energy degradation spectrum $f(x, \varepsilon)$ was based upon Monte Carlo simulation of the motion of a system of individual electrons. Obtaining statistical data in the region of small EEDF values is usually a time-consuming procedure. According to the algorithm employed, the statistics was improved by using the statistical weights of electrons: when an electron appears in the region where the corresponding $f(x, \varepsilon)$ value is small, the weight is reduced by half and another (identical) electron is created. Subsequent statistically independent motions of these electrons ensure a faster accumulation of data in the region of small $f(x, \varepsilon)$ and "smooth" this function, thus markedly reducing the time necessary for the calculation.

The electrons move starting from one point on the grid at the same velocity $V = \sqrt{2U/m_e}$ directed toward the anode, where m_e is the electron mass and U is the initial electron energy in the beam. The equations of motion were solved by the second-order Runge–Kutta method using a step of

$$\Delta t = 0.3\nu_{\max}^{-1}, \quad \nu_{\max} = N \max_{0<\varepsilon<U}\left[\sqrt{2\varepsilon/m_e}\sum_i \sigma_i(\varepsilon)\right],$$

where N is the concentration of main gas molecules, ε is the electron energy, and $\sigma_i(\varepsilon)$ are the cross sections of various processes involving electrons.

In each step, the value of $n[k, s]$ (equal to the time spent by electrons in a cell of the phase space with the coordinates x, ε and the dimensions $x_k \le x < x_{k+1} \equiv x_k + \Delta x$, $\varepsilon_s \le \varepsilon < \varepsilon_{s+1} \equiv \varepsilon_s + \Delta\varepsilon$) increases by $\Delta n = W\Delta t$, where W is the statistical weight of a given electron. The electron density distribution function $F(x, \varepsilon)$ normalized as $\int F(x, \varepsilon)d\varepsilon = 1$ is related to $n[k, s]$ by the equation

$$\frac{n[k, s]}{\sum_s n[k, s]} = F(x_k, \varepsilon_s)\Delta\varepsilon.$$

Using a random number generator and the cross sections $\sigma_i(\varepsilon)$ in the tabulated form, we determine whether a collision with a gas molecule takes place in a given step and (when it does) what the collision type is. In the case of elastic scattering, the electron loses an energy of $\Delta\varepsilon = \varepsilon\frac{2m_e}{M}$ and acquires a random direction of motion. Upon ionization, one of the electrons acquires an energy of $\varepsilon_1 = \varepsilon'\xi^{0.2}$ [9] and the other, accordingly, $\varepsilon_2 = \varepsilon' - \varepsilon_1$ (where ε' is the difference between the primary electron energy and the ionization potential, and $\xi \in [0, 1]$ is a random number). The direction of both electron velocities coincides with that of the primary electron. Exciting various states of the molecule, the electron loses an amount of energy (without changing direction) equal to the corresponding excitation energy. Upon the dissociative attachment reaction, the electron is lost.

If the electron did not collide with a neutral molecule, the same procedure is used to determine whether a recombination event took place. The recombination frequency is defined as $\nu_R = N_+(x)K_R(\varepsilon)$, where the recombination rate constant $K_R(\varepsilon)$ is known in an analytical form and the positive ion concentration $N_+(x)$ is assumed to be equal to the electron concentration $N_e(x)$. The latter is determined from the accumulated distribution $n[k, s]$ using the formula

$$N_e(x_k) = \frac{N_e^0}{\max_k\left(\sum_s n[k, s]\right)}\sum_s n[k, s],$$

where N_e^0 is a given maximum electron concentration.

In cases when the recombination did not take place either, the motion is calculated for the next step in time. Striking the grid, the electron is reflected with a probability of $\mu = 0.75$ (equal to the grid transparency) and is lost with a probability of $1 - \mu$.

When all electrons generated by the given primary electrons will be lost, the next electron of the beam appears on the grid. In addition to the spectrum $n[k, s]$, we determined a sum of the energies of electrons lost on the grid (ε_G) and anode (ε_A), as well as a result of

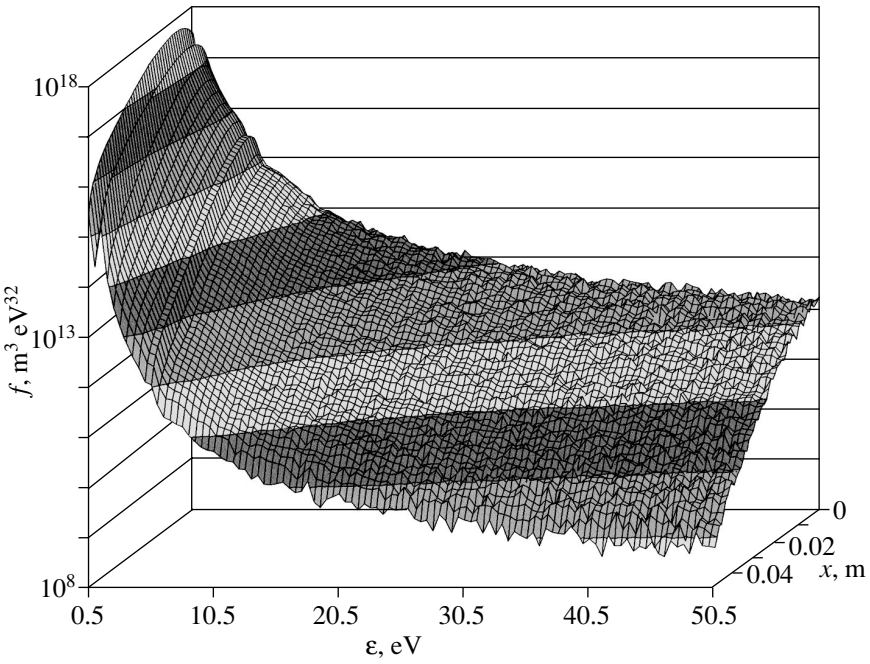

Fig. 1. Electron energy distribution function $f(x, \varepsilon)$ for a plasma pumped with a monoenergetic (U = 5 keV) electron beam in the absence of an external electric field.

recombination ($\varepsilon_R(x)$). Using the spectrum $n[k, s]$, we calculated the energies spent by electrons in the elastic collisions

$$\varepsilon_0(x_k) = \frac{2m_e}{M} N \sum_s \varepsilon_s n[k, s] \sqrt{2\varepsilon_s/m_e}\, \sigma_0(\varepsilon_s)$$

and in the inelastic collisions

$$\varepsilon_i(x_k) = \Delta_t N \sum_\varepsilon n[k, s] \sqrt{2\varepsilon_s/m_e}\, \sigma_i(\varepsilon_s),$$

where Δ_i are the corresponding reaction thresholds.

Comparative data on the relative contributions of various electron energy loss channels

	Electron beam		Electric field
	U = 1 keV	U = 10 keV	$E/N = 1.25 \times 10^{-15}$ V m^2
Grid losses	25%	26%	–
Anode losses	0.3%	4.6%	–
Ionization	32%	30%	3.8%
Herzberg states	2.5%	2.6%	17%
Dissociation $O(^3P) + O(^1D)$	18%	17%	41%
Dissociation $O(^3P) + O(^3P)$	1.7%	1.6%	11%
Rydberg states	15%	13%	14%

The calculation is conducted for a sufficiently large number of electrons in the beam, that is, until all the calculated functions would become sufficiently smooth. This procedure yields an electron energy distribution function $f(x, \varepsilon) = N_e(x)F(x, \varepsilon)\varepsilon^{-1/2}$ normalized as $\int f(x, \varepsilon)\varepsilon^{1/2} d\varepsilon = N_e(x)$, as well as the quantities ε_A, ε_G, $\varepsilon_R(x)$, and $\varepsilon(x)$ referred to the total energy $\tilde{e} = kU$, where k is the total number of electrons in the beam.

Results. The calculation was performed for oxygen at a pressure of $P_{O_2} = 1.33 \times 10^2$ Pa and a maximum electron concentration of $N_e^0 = 10^{18}$ m^{-3}, which allows the electron–electron collisions to be ignored. The drift space length (d = 0.05 m) was selected equal to a characteristic size of the electron beam degradation region. The following types of interactions between electrons and oxygen molecules in the ground state $O_2(X^3\Sigma_g^-)$ were taken into account: elastic scattering; rotational excitation; vibrational excitation; ionization; electron attachment; and excitation of the electron states ($a^1\Delta_g$, $b^1\Sigma_g^+$), a group of the Herzberg ($C^3\Delta_u$, $A^3\Sigma_u^+$, $c^1\Sigma_u^-$) or Rydberg states, or the states dissociating via channels $O_2^* \longrightarrow O(^3P) + O(^3P)$ and $O_2^{**} \longrightarrow O(^3P) + O(^1D)$. The corresponding cross sections $\sigma_i(\varepsilon)$ were taken from [8]. In addition, we made an allowance for the dissociative recombination $K_R(\varepsilon) = 2.8 \times 10^{-14}(\varepsilon/1\ \text{eV})^{-1/2}$ m^3/s.

Figure 1 shows a characteristic degradation spectrum. As is seen, the spectrum of electrons excited by the beam

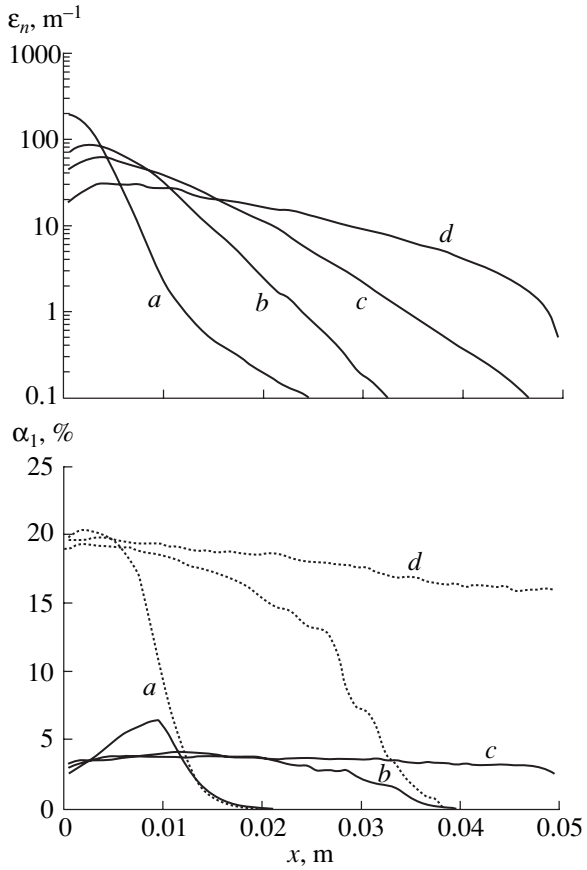

Fig. 2. Spatial distributions of the integral energy $\varepsilon_1(x) = \sum_i \varepsilon_i(x)\frac{1}{\Delta x}$ lost by electrons per unit length and relative energy fractions $\alpha_i(x) = \frac{\varepsilon_i(x)}{\Delta x \varepsilon_T(x)}$ spent for the excitation of Rydberg (---) and Herzberg (—) states for various initial beam energies U = 1 (*a*); 3 (*b*); 5 (*c*); 10 keV (*d*).

has a significantly non-Maxwellian shape strongly enriched with fast electrons. Such a distribution must favor the excitation of most high-lying states and, in contrast, suppress the energy transfer to the low-lying states.

As can be seen from the data presented in Fig. 2, the high-lying levels of oxygen molecules are excited predominantly near the grid. The size of this region is determined by the beam penetration depth, that is, by the primary electron energy. Figures 1 and 2 indicate that the distribution function $F(x, \varepsilon)$ weakly depends on x for the energies $U \geq 5$ keV, while at lower energies the spatial variation becomes significant. At low electron beam energies, the relative contributions of various components are inhomogeneously distributed in space.

For comparison, an analogous calculation was performed for electrons in a preset constant electric field typical of a stationary dc discharge in oxygen ($E/N = 1.25 \times 10^{-15}$ V m^2). The primary electrons appeared on the grid at a thermal energy of ~0.03 eV. The loss energy fractions were calculated in a stationary regime (i.e., with neglect of the losses on electrodes and in the near-electrode regions). The results were consistent with those obtained in a two-term approximation [8, 9].

Comparative data on the relative fractions of the main electron energy loss channels (integrated over space) calculated for the two methods of plasma maintenance are listed in the table. A considerable variation in the law of energy distribution between electrons during the modeled ionization event ($\varepsilon_1 = \varepsilon'\xi$) does not lead to any significant energy redistribution between the interaction channels. A change in the grid transparency results in a proportional redistribution of the corresponding energy fraction between channels. No relative changes take place upon the variation in U either. Data presented in the table indicate that excitation of the Herzberg states is most effective in the positive column of a glow discharge, while the Rydberg states are more favorably excited in the open discharge.

Conclusion. It was demonstrated that the degradation spectrum observed under the beam action is significantly enriched with fast electrons, which favors the excitation of high-lying states and suppresses the energy transfer to low-lying levels. Efficiencies of the formation of Rydberg and Herzberg states in oxygen molecules under conditions of a quasi-stationary glow discharge and a discharge with runaway electrons are compared.

We may suggest that a significant role in the experiment reported in [1] belongs to processes occurring in the region of cathode potential fall. Therefore, it is possible that an analogous experiment in the open discharge would better elucidate the mechanisms of the negative oxygen ion formation.

REFERENCES

1. W. X. Ding, L. A. Pinnaduwage, C. Tav, *et al.*, Plasma Sources Sci. Technol., No. 8, 384 (1999).
2. D. Hayashi and K. Kadota, Jpn. J. Appl. Phys., Part 1 **38** (1A), 225 (1999).
3. S. Panda, D. J. Economu, and M. Meyyapan, J. Appl. Phys. **87** (12), 8323 (2000).
4. L. A. Pinnaduwage, W. X. Ding, D. L. McCorkle, *et al.*, J. Appl. Phys. **85** (10), 7064 (1999).
5. W. X. Ding, D. L. McCorkle, and L. A. Pinnaduwage, J. Appl. Phys. **84** (6), 3051 (1998).
6. A. S. Kovalev, Yu. A. Mankelevich, E. A. Muratov, *et al.*, Fiz. Plazmy **18** (8), 1076 (1992) [Sov. J. Plasma Phys. **18**, 561 (1992)].
7. P. A. Bokhan and A. R. Sorokin, Zh. Tekh. Fiz. **55** (1), 88 (1985) [Sov. Phys. Tech. Phys. **30**, 50 (1985)].
8. V. V. Ivanov, K. S. Klopovskiĭ, D. V. Lopaev, *et al.*, Preprint No. 2000–16/620, NIIYaF MGU (Skobeltsyn Research Institute of Nuclear Physics, Moscow State Univ., Moscow, 2000).
9. T. J. Summerer, W. H. G. Hitchon, and J. E. Lawler, Phys. Rev. A **39**, 6356 (1989).

Translated by P. Pozdeev

Technical Physics Letters, Vol. 27, No. 9, 2001, pp. 716–718. Translated from Pis'ma v Zhurnal Tekhnicheskoĭ Fiziki, Vol. 27, No. 17, 2001, pp. 16–21.

Reconstruction of the Absorption Profile of an Inhomogeneous Planar Optical Waveguide

A. A. Romanenko

Institute of Applied Optics, Academy of Sciences of National Belarus, Mogilev, Belarus

e-mail: ipo@physics.belpak.mogilev.by

Received February 14, 2001

Abstract—An algorithm for reconstructing the imaginary part of permittivity of an inhomogeneous planar optical waveguide is proposed. The algorithm uses information on the spectrum of imaginary parts of the propagation constants of guided modes. Examples illustrating the efficiency of this approach are provided. © *2001 MAIK "Nauka/Interperiodica".*

Reconstruction of the permittivity profile $\varepsilon(y)$ of a planar optical waveguide is of great practical interest [1]. To date, several methods for reconstruction of the $\mathrm{Re}\varepsilon(y)$ distribution have been proposed [2–6]. At the same time, reconstruction of $\mathrm{Im}\varepsilon(y)$ is still not adequately studied. This problem is important for developing the optical waveguide technology [7] and studying mechanisms governing the interaction of activated films with detected components of gases and liquids [8]. At present, a method for the reconstruction of $\mathrm{Im}\varepsilon$ of a homogeneous waveguide is known. It uses the solution of the corresponding dispersion equation under the condition that the complex propagation constants of at least two modes were previously measured [9]. However, this approach cannot be used when $\mathrm{Im}\varepsilon$ noticeably depends on y.

In this paper, a method for reconstructing the $\mathrm{Im}\varepsilon(y)$ function of an inhomogeneous multimode waveguide is proposed. The method uses information on the spectrum of complex propagation constants of all guided modes that allow experimental recording by the prism method [9].

As a rule, absorption in an optical waveguide is a small perturbing factor for the distributions of fields and real parts of the propagation constants of waveguide modes. This fact allows us to use the perturbation theory, which yields the relationship [10]

$$\mathrm{Im}\beta_l = k_0^2 \int_0^d Y_l^2(y)\mathrm{Im}\varepsilon(y)dy \left(2\mathrm{Re}\beta_l \int_{-\infty}^{\infty} Y_l^2(y)dy\right)^{-1}. \quad (1)$$

Here, $l = 1, 2, \ldots, M$, M is the total number of guided modes; $\beta_l = \mathrm{Re}\beta_l + i\mathrm{Im}\beta_l$ are the complex propagation constants of TE modes; d is the waveguide thickness; $Y_l(y)$ is the transverse distribution of the mode field; l is the mode index; and k_0 is the wavenumber in vacuum. We will consider expression (1) as a relationship connecting the unknown function $\mathrm{Im}\varepsilon(y)$ to the spectrum of imaginary parts of the propagation constants of waveguide modes that can be experimentally measured [9]. The function $\mathrm{Re}\varepsilon(y)$, which determines the constants $\mathrm{Re}\beta_l$ and the field $Y_l(y)$, is already assumed to be reconstructed. In order to reconstruct the function $\mathrm{Im}\varepsilon(y)$, we expand it in terms of a set of linearly independent functions $\varphi_n(y)$:

$$\mathrm{Im}\varepsilon(y) = \sum_{n=1}^{M} a_n\varphi_n(y). \quad (2)$$

The unknown amplitudes a_n can be found by the least squares method [11]. Assuming that all constants $\mathrm{Im}\beta_l$ were measured with the same accuracy, we compose the sum

$$I = \sum_{l=1}^{M}\left[\mathrm{Im}\beta_l - k_0^2\int_0^d Y_l^2(y) \times \sum_{n=1}^{M} a_n\varphi_n(y)dy\left(2\mathrm{Re}\beta_l\int_{-\infty}^{\infty} Y_l^2(y)dy\right)^{-1}\right]^2. \quad (3)$$

The condition of minimum for the sum I gives the algebraic system

$$\sum_{j=1}^{M}\alpha_{ij}a_j = b_i \quad (i = 1, 2, \ldots, M), \quad (4)$$

where

$$\alpha_{ij} = \sum_{k=1}^{M} C_{ki}C_{kj},$$

$$C_{ki} = k_0^2\int_0^d Y_k^2(y)\varphi_i(y)dy\left(2\mathrm{Re}\beta_k\int_{-\infty}^{\infty} Y_k^2(y)dy\right)^{-1},$$

$$b_i = \sum_{k=1}^{M} \mathrm{Im}\,\beta_k C_{ki}.$$

Selection of the functions $\varphi_n(y)$ plays an important role in solving this inverse problem, because these quantities determine the degree of conditionality of system (4) [12]. Here, we investigate three sets among all known sets of functions applied in the perturbation theory for optical waveguides [10, 13–15], namely, even trigonometric functions $\cos(n\pi y d^{-1})$ with period $2d$, fields $Y_l(y)$ of waveguide modes, and squared mode fields $Y_l^2(y)$.

Numerical experiments were conducted for waveguides with profiles $\varepsilon(y)$ taking maximum values at the waveguide surface. Distributions $\varepsilon(y)$ were specified in the form

$$\varepsilon(y) = \varepsilon_s + \mathrm{Re}\,\Delta\varepsilon_0 F(y) + i\,\mathrm{Im}\,\Delta\varepsilon_0 f(y). \qquad (5)$$

Here, $\Delta\varepsilon_0$ and ε_s are the permittivity increment at the waveguide surface and the permittivity of substrate, respectively. For calculations, we have chosen the distributions $\varepsilon(y)$ involving monotonic functions $F(y)$ and $f(y)$ of two types:

$$F(y) = F_1(y) = \exp(-(\alpha y d^{-1})^2),$$
$$f(y) = f_1(y) = \exp(-(\gamma y d^{-1})^2), \qquad (6)$$

$$F(y) = F_2(y) = 1 - \mathrm{erf}(\sigma y d^{-1}),$$
$$f(y) = f_2(y) = 1 - \mathrm{erf}(\eta y d^{-1}). \qquad (7)$$

These functions correspond to diffusion techniques [3]. The calculations were performed for $\varepsilon_s = 2.25 - i1 \times 10^{-6}$, $k_0 d = 200$, $\alpha = 2$, $\sigma = 2$, $\mathrm{Re}\,\Delta\varepsilon_0 = 0.1$, and various values of γ and η. For these parameters of the waveguide, the total number of guided modes equals twelve and nine for distributions (6) and (7), respectively. Constants $\mathrm{Im}\,\beta_l$ were calculated by the method of contour integration [16].

Numerical experiments performed with exactly calculated values of constants $\mathrm{Im}\,\beta_l$ have shown that the trigonometric series ensures the most adequate reconstruction of the $\mathrm{Im}\,\varepsilon(y)$ profile. It has been found, however, that the presence of noise in the specified constants $\mathrm{Im}\,\beta_l$ causes a substantial instability of the results of reconstruction. This fact indicates that, in the case of trigonometric functions, system (4) is ill-conditioned. Using expansion (2) with the fields and squared fields of waveguide modes, we obtained systems (4) with dominating diagonal matrix elements α_{ij}. As a result, reconstruction of the $\mathrm{Im}\,\varepsilon(y)$ profile became stable with respect to the noise in constants $\mathrm{Im}\,\beta_l$. The most acceptable results were obtained for squared mode fields. The accuracy of the reconstruction procedure $\mathrm{Im}\,\varepsilon(y)$ can be estimated from Fig. 1. It should be noticed that the plots of reconstructed functions are curves oscillating near plots of exact functions $\mathrm{Im}\,\varepsilon(y)$. Maximum deviations

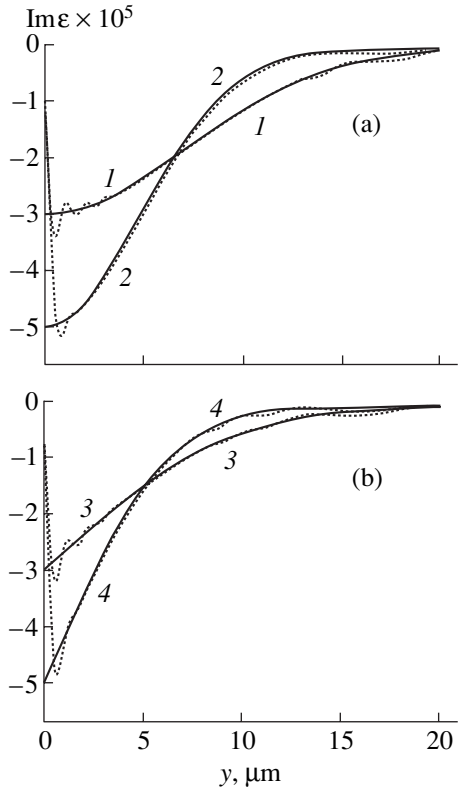

Fig. 1. Reconstruction of the $\mathrm{Im}\,\varepsilon(y)$ functions. Solid curves are the exact functions and dots show the functions reconstructed ones for (a) distribution (6) and (b) distribution (7). Curves *1* and *2* are obtained for $\gamma = 2.0$ and 3.0; curves *3* and *4*, for $\eta = 2.0$ and 3.0, respectively.

of the reconstructed function from the exact one are observed near the waveguide surface. These deviations can be explained by the fact that the mode fields in this region are close to zero. Calculations revealed that, by increasing the thickness d of the optical waveguide (and the total number of waveguide modes), we increase the frequency of oscillations of the reconstructed function and decrease the oscillation amplitude. However, a substantial error in the $\mathrm{Im}\,\varepsilon(y)$ reconstructed near the waveguide surface is still retained.

REFERENCES

1. S. Hosain, J. P. Meunier, E. Bourillot, *et al.*, Fiber Integr. Opt. **14** (1), 89 (1995).
2. J. M. White and P. F. Heidrich, Appl. Opt. **15** (1), 151 (1976).
3. A. I. Voitenkov and V. N. Mogilevich, Kvantovaya Élektron. (Moscow) **10** (10), 2128 (1983).
4. W. Preude and A. Sharma, J. Lightwave Technol. **3** (3), 628 (1985).
5. A. B. Sotskiĭ, A. V. Khomchenko, and L. I. Sotskaya, Radiotekh. Élektron. (Moscow) **39** (10), 1591 (1994).
6. J. Helms, J. Schmidtchen, D. Schuppert, and K. Petermann, J. Lightwave Technol. **8** (5), 625 (1990).

7. O. L. Artemenko, G. V. Litvinovich, and V. K. Matchenya, in *Covariant Methods in Theoretical Physics. Optics and Acoustics. A Collection of Papers* (Minsk, 1991), pp. 22–28.
8. A. V. Khomchenko, E. V. Glazunov, and I. U. Primak, Pis'ma Zh. Tekh. Fiz. **25** (24), 11 (1999) [Tech. Phys. Lett. **25**, 974 (1999)].
9. A. B. Sotskiĭ, A. A. Romanenko, A. V. Khomchenko, and I. U. Primak, Radiotekh. Élektron. (Moscow) **44** (6), 687 (1999).
10. D. Marcuse, *Integrated Optics* (IEEE Press, New York, 1973; Mir, Moscow, 1974).
11. G. A. Korn and T. M. Korn, *Mathematical Handbook for Scientists and Engineers* (McGraw-Hill, New York, 1968; Nauka, Moscow, 1973).
12. A. N. Tikhonov and V. Ya. Arsenin, *Solutions of Ill-Posed Problems* (Nauka, Moscow, 1986; Halsted Press, New York, 1977).
13. V. V. Shevchenko, Radiotekh. Élektron. (Moscow) **31** (5), 849 (1986).
14. V. V. Shevchenko, Diff. Uravn. **15** (11), 2004 (1979).
15. *Integrated Optics*, Ed. by T. Tamir (Springer-Verlag, Berlin, 1975; Mir, Moscow, 1978).
16. A. A. Romanenko and A. B. Sotskiĭ, Zh. Tekh. Fiz. **68** (4), 88 (1998) [Tech. Phys. **43**, 427 (1998)].

Translated by A. Kondrat'ev

Technical Physics Letters, Vol. 27, No. 9, 2001, pp. 719–721. Translated from Pis'ma v Zhurnal Tekhnicheskoĭ Fiziki, Vol. 27, No. 17, 2001, pp. 22–28.

Supraluminal Velocity of a Pulse Envelope Maximum in Amplifying Optical Fiber

A. V. Zolotov, I. O. Zolotovskiĭ, and D. I. Sementsov

Ul'yanovsk State University, Ul'yanovsk, Russia

e-mail: sdi@sdi.ulsu.ru

Received February 12, 2001

Abstract—Frequency-modulated Gaussian pulse propagation in an amplifying fiber is described within the framework of a linear model with an allowance for the second-order dispersion effects. It is demonstrated that the presence of an imaginary part in the group velocity dispersion parameter of the single-mode optical fiber with luminous gain leads to the possibility of the pulse envelope at a supraluminal velocity. © *2001 MAIK "Nauka/Interperiodica".*

An important feature of a pulse propagating in an amplifying medium is the principal possibility for the pulse to move at a velocity exceeding the speed of light in vacuum [1]. This leads to no discrepancies with the basic principles of relativity because photons forming the pulse still move at a velocity of light characteristic of the given medium. However, the luminous gain results in that the photon concentration on the leading pulse front exceeds that on the trailing front so that the "center-of-gravity" of the pulse shifts in the direction of the pulse propagation. Thus, the supraluminal pulse propagation implies that the wave packet envelope maximum moves at the expense of amplification (more pronounced on the leading front) rather than the energy being transferred at this rate.

Although the phenomenon of supraluminal velocity was observed long ago [2, 3], this effect still draws the attention of researchers [4, 5]. However, the cited papers did not analyze the influence of an imaginary component of the dispersion parameters on the pulse envelope propagation velocity. At the same time, it was recently demonstrated [6, 7] that the phase self-modulation related to the imaginary component of the group velocity dispersion significantly affects the dynamics of a pulse propagating in an optical fiber with luminous gain. In particular, the pulse may exhibit compression even in the absence of a frequency modulation and with neglect of the nonlinear effects. Below, we will analyze conditions for the supraluminal velocity of a pulse envelope maximum with an allowance for the complex character (imaginary part) of the group velocity dispersion parameter by solving a dynamic equation for the time envelope of a pulse in a single-mode amplifying optical fiber.

Let us consider a single-mode optical fiber in which an effective index of refraction $N = N_1 - iN_2$ for the pulse-forming mode is complex. This implies complexity of the mode propagation constant $\beta = \beta_1 - i\beta_2 = \omega N/c$, where c is the speed of light in vacuum and ω is the radiation frequency. A dynamic equation for the time envelope of a pulse written in a linear approximation with an allowance for the first- and second-order dispersion effects is as follows [8]:

$$\frac{\partial A}{\partial z} + \frac{1}{u}\frac{\partial A}{\partial t} - i\frac{D}{2}\frac{\partial^2 A}{\partial t^2} = 0. \qquad (1)$$

Here, the complex parameters $u = u_1 - iu_2 \equiv (\partial\beta/\partial\omega)_0^{-1}$ and $D = D_1 - iD_2 = (\partial^2\beta/\partial\omega^2)_0$ represent the group velocity and its dispersion, respectively, and the derivatives are taken at the central pulse frequency ω_0. Let a frequency-modulated Gaussian pulse with a given time envelope enter the fiber. In terms of the running time $\tau = t - z/u_1$, the envelope shape is represented as

$$A(\tau, 0) = A_0 \exp\left[-(1 + i\alpha_0\tau_0^2)\tau^2/2\tau_0^2\right], \qquad (2)$$

where α_0 is the frequency modulation rate in the pulse and τ_0 is the initial pulse width. A solution to Eq. (1) with an allowance for Eq. (2) can be found in the form of $A(\tau, z) = \rho\exp(i\Phi)$, where Φ is the phase of the propagating pulse and ρ is a function describing the pulse amplitude and shape:

$$\rho(\tau, z) = V(z)\exp\left[-\frac{(\tau - Su_2^{-1}z)^2}{2\tau_u^2}\right]. \qquad (3)$$

Here, $V(z)$ and $\tau_u(z)$ are the pulse amplitude function and pulse width depending on the path length traveled by the pulse in the optical fiber, while S is a parameter given by the expression

$$S = \frac{(\alpha_0^2\tau_0^2 + \tau_0^{-2})D_1 z - \alpha_0\tau_0^2}{1 + (\alpha_0^2\tau_0^2 + \tau_0^{-2})D_2 z}. \qquad (4)$$

1063-7850/01/2709-0719$21.00

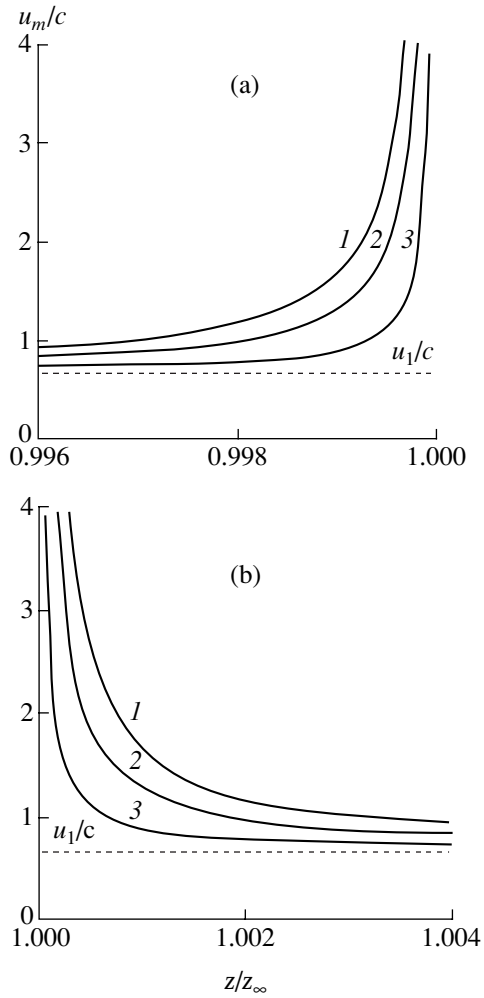

Fig. 1. The plots of relative velocity u_m/c of the pulse envelope maximum versus normalized distance z/z_∞ traveled by the pulse in the fiber.

According to Eq. (3), the velocity of the pulse envelope maximum propagation is determined by the formula

$$u_m = \frac{u_1}{1 + Su_1/u_2}, \tag{5}$$

where u_1c/N_1 is a quantity usually interpreted as the group velocity of the pulse. In order to determine the parameters u_2 and D_2, we will use a relationship between the imaginary part of the propagation constant and the linear gain $2\beta_2(\omega) = \alpha(\omega)$. For a radiation intensity far from saturation of an active medium [9],

$$\alpha(\omega) = \sigma n[1 + (\Delta\omega/\Delta\omega_L)^2]^{-1}, \tag{6}$$

where $\Delta\omega_L$ is the Lorentz linewidth of the gain loop, $\Delta\omega = \omega_0 - \omega_r$ is the detuning of the central pulse frequency from the resonance frequency ω_r of the induced optical transition, σ is the transition cross section, and n is the density of the active generation centers. In this notation, the parameter D_2 is expressed as follows:

$$D_2 = \frac{\sigma n}{\Delta\omega_L^2}\left[1 - 3\left(\frac{\Delta\omega}{\Delta\omega_L}\right)^2\right]\left[1 + \left(\frac{\Delta\omega}{\Delta\omega_L}\right)^2\right]^{-3}. \tag{7}$$

Using relationship (6), the parameter u_2 can be expressed as

$$u_2^{-1} = (\partial\beta_2/\partial\omega)_0 = \frac{\sigma n\Delta\omega_L^2\Delta\omega}{(\Delta\omega_L^2 + \Delta\omega^2)^2}. \tag{8}$$

An analysis of the formula (5) shows that the velocity u_m of the pulse envelope maximum exceeds the group velocity u_1 when $S/u_2 < 0$. In this case, there are two possible situations: for $1 - N_1 < cS/u_2 < 0$, the u_m value is greater than u_1 but still smaller than the speed of light in vacuum; for $-N_1 < cS/u_2 < 1 - N_1$, we deal with the supraluminal propagation whereby $u_m > c$. These situations can be observed for various signs of the central pulse frequency detuning from the resonance $\omega_0 - \omega_r$ and the signs of α_0 and D_1. For example, assuming α_0 and D_1 to be positive, we arrive at the following conditions. In the frequency range $|\Delta\omega| < \Delta\omega_L/\sqrt{3}$, we obtain $D_2 > 0$ and, according to Eq. (8), $u_2 > 0$ for $\omega_0 > \omega_r$. Therefore, a supraluminal velocity of the pulse envelope maximum is reached at a distance of

$$z < z_1 = \frac{\alpha_0\tau_0^4}{1 + \alpha_0^2\tau_0^4}\frac{1}{D_1}. \tag{9}$$

For $\omega_0 < \omega_r$, we obtain $u_2 < 0$ and a supraluminal envelope propagation is observed at $z > z_1$. In the frequency range $|\Delta\omega| > \Delta\omega_L/\sqrt{3}$, where $D_2 < 0$, this propagation regime is attained at $z < z_i$ and $z > z_{3-i}$ ($i = 1, 2$). Here, $z_i < z_{3-i}$ and

$$z_2 = \frac{\tau_0^2}{1 + \alpha_0^2\tau_0^4}\frac{1}{|D_2|}. \tag{10}$$

Figure 1 shows the plots of relative velocity u_m/c of the pulse envelope maximum versus normalized distance z/z_∞ traveled by the pulse in the fiber (z_∞ is the distance at which $u_m \longrightarrow \infty$). The curves were constructed for the following fiber parameters: $\omega_r = 1.8 \times 10^{15}$ s^{-1}; $\sigma n = 456$ m^{-1}; $\Delta\omega_L = 5 \times 10^{12}$ s^{-1}; $\tau_0 = 5 \times 10^{-12}$ s; $\alpha_0 = 10^{22}$ s^{-2}; $D_1 = 6 \times 10^{-26}$ s^2/m; $\Delta\omega = (2, 3, 10) \times 10^{12}$ s^{-1} (Fig. 1a, *1–3*) and $(-2, -3, -10) \times 10^{12}$ s^{-1} (Fig. 1b, *1–3*); the corresponding normalization factors for curves *1–3* are $z_\infty = 3.9$, 40.5, and 14.7 m, respectively. Note that a significant increase in the u_m value is observed within a rather narrow region of z in the vicinity of z_∞. The tendency of u_m to infinity with $z \longrightarrow z_\infty$ is related to a restricted character of the model employed (in particular, with neglect of the high-order dispersion effects and

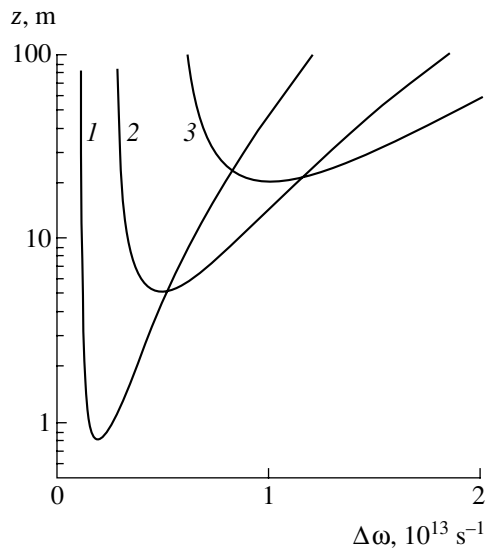

Fig. 2. Plots of the distance z at which the supraluminal propagation of the pulse envelope maximum is developed versus detuning $\Delta\omega$ of the central pulse frequency from the resonance.

the kinetics of inversion in the amplifying fiber transmitting the pulse).

Figure 2 shows the distance z, at which the supraluminal propagation of the pulse envelope maximum is developed, as a function of the detuning $\Delta\omega$ of the central pulse frequency from the resonance calculated for a linewidth $\Delta\omega_L = (2, 5, 10) \times 10^{12}$ s^{-1} (Fig. 2, *1*–*3*). As the gain linewidth grows, the interval of detuning $\Delta\omega$ and the minimum distance z_m (at which the supraluminal propagation effect is manifested) tend to increase. A minimum of this dependence corresponds to a detuning $\Delta\omega$ equal to the linewidth $\Delta\omega_L$. These points are most convenient for observing the supraluminal propagation effect.

The above analysis indicates that taking into account the complex character (imaginary part) of the dispersion parameter in the optical fibers with luminous gain provides for the possibility of realization of a supraluminal velocity of the pulse envelope propagation in this fiber. The effect is possible not only for pulses of the exponential shape (as was pointed out in [1]) but for the Gaussian pulses (possessing a steeper envelope) as well.

REFERENCES

1. A. N. Oraevskiĭ, Usp. Fiz. Nauk **168** (12), 1311 (1998) [Phys. Usp. **41**, 1199 (1998)].
2. N. G. Basov *et al.*, Zh. Éksp. Teor. Fiz. **50**, 23 (1966) [Sov. Phys. JETP **23**, 16 (1966)].
3. R. Ambartsumyan *et al.*, Pis'ma Zh. Éksp. Teor. Fiz. **4**, 19 (1966) [JETP Lett. **4**, 12 (1966)].
4. A. Yu. Andreev and D. A. Kirzhnits, Usp. Fiz. Nauk **166**, 1135 (1996) [Phys. Usp. **39**, 1071 (1996)].
5. R. Y. Chiao, A. E. Kozhekin, and G. Kurizki, Phys. Rev. Lett. **77**, 1254 (1996).
6. I. O. Zolotovskiĭ and D. I. Sementsov, Zh. Tekh. Fiz. **70** (10), 57 (2000) [Tech. Phys. **45**, 1288 (2000)].
7. I. O. Zolotovskiĭ and D. I. Sementsov, Kvantovaya Élektron. (Moscow) **30** (9), 794 (2000).
8. G. Agrawal, *Nonlinear Fiber Optics* (Academic, San Diego, 1995; Mir, Moscow, 1996).
9. *Handbook of Lasers*, Ed. by A. M. Prokhorov (Sov. Radio, Moscow, 1978).

Translated by P. Pozdeev

Technical Physics Letters, Vol. 27, No. 9, 2001, pp. 722–724. Translated from Pis'ma v Zhurnal Tekhnicheskoĭ Fiziki, Vol. 27, No. 17, 2001, pp. 29–34.

Supersonic Flow Regimes with a Pulsating Laser Radiation Energy Supply

V. I. Yakovlev

Institute of Theoretical and Applied Mechanics, Siberian Division, Russian Academy of Sciences, Novosibirsk, Russia

e-mail: yakovlvi@itam.nsc.ru

Received February 26, 2001

Abstract—A comparative analysis of the gas flow regimes behind the region of laser energy supply to a supersonic jet is performed depending on the laser radiation focusing conditions. A relationship established between the energy and gasdynamic parameters reveals a significant difference in the flow parameters (velocity, stagnation pressure) behind the extended and localized (point) thermal plasma sources for the identical initial conditions in a supersonic jet with the Mach numbers M = 1.5–10. © *2001 MAIK "Nauka/Interperiodica"*.

It was demonstrated [1, 2] that the gas flow parameters behind an extended optical breakdown region formed in a supersonic jet are determined by laser plasma dynamics. This flow regime is possible provided the breakdown plasma region is characterized by a sufficiently large length to diameter ratio l/d, as determined by the laser radiation focusing. In the case of $l \approx d$, the conditions for the laser detonation wave maintenance are violated and the process character significantly changes so as to correspond to a local instantaneous energy deposition. This condition was used in the numerical investigations of the relationship between spatiotemporal energy parameters of the thermal source and the flow structure in the vicinity of this source and streamlined bodies [3–6]. An analytical model corresponding to a strong point explosion was also used to calculate the required shock wave configuration caused by a series of laser pulses [7]. As will be shown below, the possibilities of an analytical approach within the framework of the same model can be significantly extended so as to determine, besides the characteristic scale, the gasdynamic parameters and establish a relationship between these parameters and the energy characteristics using generalized numerical data on the postexplosion flow determined in a broad range of conditions with an allowance for the counterpressure [8, 9].

The purpose of this study was to analyze the structure of a quasi-stationary flow in a supersonic jet with pulsating laser-initiated breakdown under short-focusing conditions (based on a point explosion model). Another task was to evaluate parameters of the medium behind the breakdown region depending on the energy characteristics of the laser radiation and the flow velocity (Mach number). In order to reveal the characteristic features of the flow regime with instantaneous local energy deposition, we will perform a comparative analysis of these results with the data obtained using a model [1, 2] taking into account a finite (albeit large) rate of the energy supply behind the optical detonation wave (extended source model) for the same values of the average laser radiation power and the initial experimental flow conditions.

The measured average absorbed laser radiation power (equal to the product of the pulse energy by the pulse repetition rate f) is N = 1.6 kW (at f = 100 kHz). It is assumed that (in contrast to the extended source model) the energy is instantaneously absorbed at the point of radiation focusing (i.e., the basic conditions of the point explosion model are fulfilled). Assuming the frequency is sufficiently high to form a quasi-stationary flow (this condition is formulated below), we determine the initial energy parameter (energy per unit length) $E_0 = N/u_\infty$, where u_∞ is the flow velocity. As a result, we determine the spatiotemporal scales of a point explosion with cylindrical symmetry: $r^0 = (E^0/P_\infty)^{1/2}$ and $t^0 = r^0(r_\infty/P_\infty)^{1/2}$ (equal to r^0 = 8.4 mm and t^0 = 54 μs for an experiment with E^0 = 4 J/m). For the numerical analysis, the radial distribution of the flow parameters at various time instants upon explosion were determined using tabulated data [8] for the gasdynamic parameters presented as functions of the dimensionless variables $\xi = (r_i/r_n)^2$ and $q = (a_\infty/c)^2$, where r_i and r_n are the radii of selected points and of the shock wave, respectively; a_∞ is the sound velocity in the incident flow; and c is the shock wave velocity. For a fixed distance x from the point of explosion (radiation focusing), $t = x/u_\infty$ and the dimensionless parameter t/t^0 determines the value of q.

Figure 1a shows plots of the relative pressure P_0/P_∞, sound velocity a_0/a_∞, and radial velocity (expansion) of the medium v_0/a_∞ versus q (increase in q corresponds to going away from the point of explosion) calculated for the effective adiabate exponent γ = 1.3 (*1*) and 1.67 (*2*) in the central part of the flow. Also indicated

are the intervals of q corresponding to the Mach numbers $M_\infty = 2$ and 10 for $x = 5$–30 mm. A common feature of these solutions is the fact that virtually constant levels of $P_0/P_\infty \cong 1$, $a_0/a_\infty \cong 5$, and $v_0/a_\infty \cong 0$ are established for $q \geq 0.35$ with a relative deviation not exceeding a few percent; note also that the velocity changes sign at $q = 0.6$–0.8. An isobaric flow with the steady-state parameters is determined by the coordinate $x^* = u_\infty(t/t^0)t^0$, where $t/t^0 \cong 0.11$–0.13 (depending on γ) for $q = 0.35$.

Figure 1b presents the radial profiles of the relative density ρ/ρ_n for $\gamma = 1.3$ (the patterns for other γ are analogous) and two fixed values of $q = 0.6$ and 0.8 (corresponding to $x = 7.6$ and 24.4 mm, respectively). These data are depicted in addition to the calculated shock wave configuration r_n (curves *1* and *2*), the experimental data for an argon flow with $M_\infty = 2$ [1, 2], and the level of density ρ_∞ in the unperturbed flow. Once the distribution of the latter parameter is known, we may estimate its average value in the central region as $\rho_0 \cong 0.03$–$0.04\rho_\infty$ (as well as the sound velocity $a_0 \cong 5a_\infty$). This value can be adopted at the point r_0 (closest to the axis) so as to eliminate the singularity of the point-explosion solution at $r = 0$. This choice is also justified by the fact that, according to estimates, the spatial scale of the heat and mass transfer processes in argon at high temperatures is close to r_0.

The inner and outer boundaries of the characteristic low-density (and high-temperature) region are indicated by r_0 and r_1 lines (lying below *Ox*) in Fig. 1b. As x increases, the former boundary remains virtually constant (r_0 does not exceed 0.9–1.2 mm), whereas the outer boundary radius exhibits a significant (several-fold) growth indicating expansion of the region of nearly constant density gradient. This behavior differs the process under consideration from the energy deposition behind the optical detonation wave front where the thermal trace boundary (curve *3*) represents a weak shock wave separating high-speed plasma jet from the main gas flow [2].

A dependence of the flow parameters on the power N is manifested in the relationship between E^0, r^0, and t^0 values, which vary in a correlated manner in proportion to $N^{1/2}$. The t/t^0 and q values decrease, while the shock wave radius and the gasdynamic parameters increase. Figure 1b also indicates ($10E^0$ arrows) a change in r_0, r_1, and r_n upon a tenfold increase in the laser power. A most significant (2.5- to 3-fold) growth is observed for r_0, while the shock wave radius exhibits a minimum change. Thus, the effect of increase in the laser power is manifested by the increasing size of the low-density region and by attaining a stationary flow regime faster ($q > 0.35$).

The condition of a quasi-stationary flow regime with instantaneous energy supply appears as $u_\infty/f \sim r_0$ (or r_1, which is smaller than 1 mm), with the corresponding

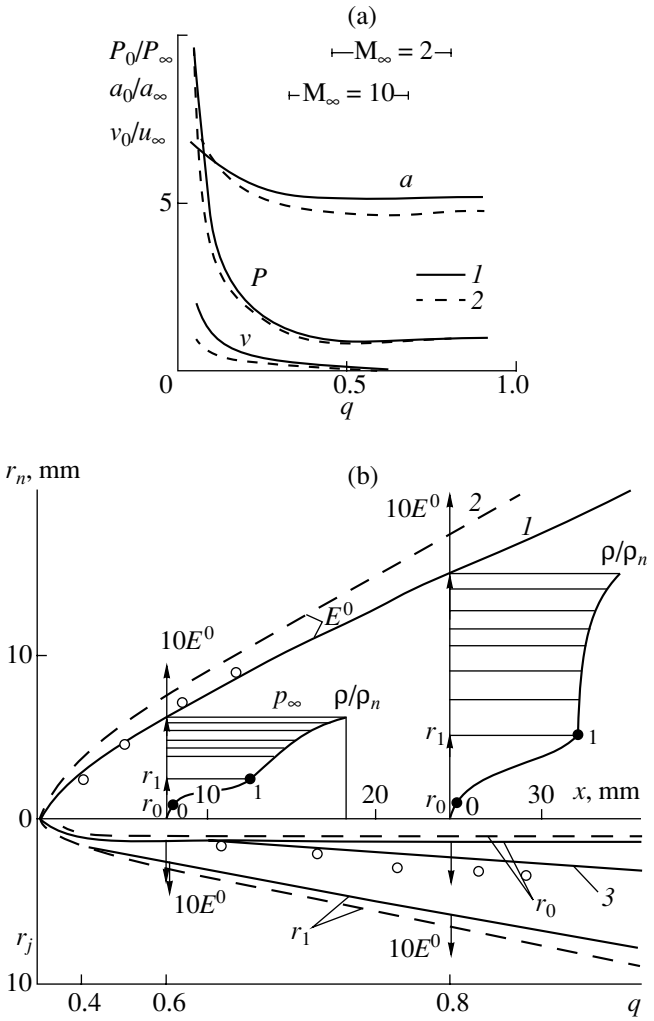

Fig. 1. Plots of (a) gasdynamic parameters of the flow in the central region and (b) the wave structure in the vicinity of the energy supply region in a supersonic flow with $M_\infty = 2$ versus distance (parameter q) from the point of explosion (radiation focusing).

frequency above 400 kHz. In comparison to an extended source (for which $u_\infty/f \sim l$), the short-focusing conditions require a higher frequency. Under a less rigid condition $u_\infty/f \sim r_n$ (when a spherically symmetric solution should be used), the f value decreases several times (at the expense of increasing inhomogeneity of the distribution of parameters). In both energy supply regimes, the required frequency increases with the flow velocity (Mach number).

In order to determine the average values of the velocity characteristics of a quasi-stationary flow (Mach number, stagnation pressure), we use a general property of the solution for the velocity of medium expansion in the central region of the explosion: $v/a_\infty \cong 0$. This condition implies that the average axial velocity u_0 of medium in the isobaric region (with a radius of r_0) at the flow center is close to the incident

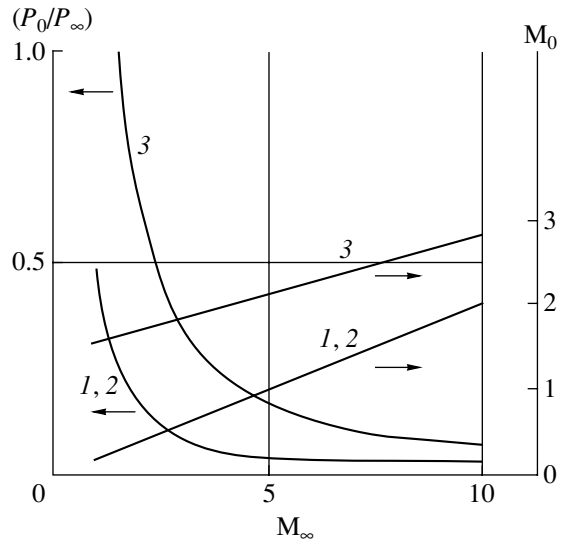

Fig. 2. Plots of the velocity parameters of the flow (Mach number, relative stagnation pressure) behind the energy supply region in a supersonic flow versus M_∞: (*1*, *2*) point explosion model; (*3*) extended source model.

flow velocity ($u_0 \cong u_\infty = M_\infty a_\infty$). Under these conditions (Fig. 1a), the sound velocity acquires a virtually constant value $a_0 = Ka_\infty$ with a coefficient of $K \cong 5$ (varying within 10% for various γ). As a result, we may determine the Mach number in the central region of the flow: $M_0 = M_\infty/K \cong M_\infty/5$. This result is presented in Fig. 2 (curves *1* and *2*) in comparison with the data (curve *3*) obtained using an extended source model with analogous initial conditions and the same average radiation power at the point where the isobaric conditions are fulfilled. These data indicate that (for M_∞ = 1–10) the Mach number in the flow behind the energy supply region is always smaller as compared to that in the main flow and is minimum in the explosion regime (in the latter case, the flow is subsonic for $M_\infty < 5$).

Figure 2 also shows the relative variation of the stagnation pressure $(P_0/P_\infty)^*$ determined using the known relationship between the gasdynamic parameters of the flow for both quasi-stationary regimes of energy supply. It is demonstrated for the first time that, provided an equal average radiation power, the drag parameters are significantly different (being three times smaller under the short-focusing conditions with small M_∞) at a considerable (more than one order of magnitude) general decrease with an increasing Mach number of the incident flow. The established decrease in the rate of variation of the $(P_0/P_\infty)^*$ value at large M_∞ implies that (under otherwise equal conditions) the energy supply effects (e.g., for the body streamlining) will vary rather weakly in the velocity range above $M_\infty \cong 5$. In addition, since the integral effects of the energy supply also depend on the ratio of the transverse dimensions of a streamlined body and the region featuring a significant change in the flow parameters (with a radius not exceeding r_1), these effects will increase with the power only within certain limits determined by the ratio of the above dimensions.

REFERENCES

1. P. K. Tret'yakov and V. I. Yakovlev, Dokl. Akad. Nauk **365** (1), 58 (1999) [Dokl. Phys. **44**, 178 (1999)].
2. V. I. Yakovlev, in *Proceedings of the International Conference on the Methods of Aerophysical Research, Novosibirsk–Tomsk*, 2000, Part 3, p. 139; Pis'ma Zh. Tekh. Fiz. **27** (9), 13 (2001) [Tech. Phys. Lett. **27**, 356 (2001)].
3. P. Yu. Georgievskiĭ and V. A. Levin, Pis'ma Zh. Tekh. Fiz. **14** (8), 684 (1988) [Sov. Tech. Phys. Lett. **14**, 303 (1988)].
4. S. V. Guvernyuk and A. B. Samoĭlov, Pis'ma Zh. Tekh. Fiz. **23** (9), 1 (1997) [Tech. Phys. Lett. **23**, 333 (1997)].
5. N. A. Korotaeva and A. P. Shashkin, in *Proceedings of the International Conference on the Methods of Aerophysical Research, Novosibirsk–Tomsk*, 2000, Part 2, p. 100.
6. V. N. Zudov, in *Proceedings of the International Conference on the Methods of Aerophysical Research, Novosibirsk–Tomsk*, 2000, Part 3, p. 162.
7. L. N. Myrabo and Yu. P. Raizer, AIAA Pap., No. 94-2451 (1994).
8. V. P. Korobeĭnikov, P. I. Chushkin, and K. V. Sharovatova, *Gas-Dynamic Functions of Point Explosion* (Vychisl. Tsentr Akad. Nauk SSSR, Moscow, 1969).
9. V. P. Korobeĭnikov, *Problems of the Theory of Point Explosion* (Nauka, Moscow, 1985).

Translated by P. Pozdeev

Technical Physics Letters, Vol. 27, No. 9, 2001, pp. 725–727. Translated from Pis'ma v Zhurnal Tekhnicheskoĭ Fiziki, Vol. 27, No. 17, 2001, pp. 35–39.

X-ray Irradiation at Subthreshold Energies Modifies the Surface Micromorphology of Epitaxial Silicon Layers on Sapphire

A. N. Kiselev, V. A. Perevoshchikov, V.D. Skupov, and D. O. Filatov

Nizhni Novgorod State University, Nizhni Novgorod, Russia

e-mail: spm@phys.unn.runnet.ru

Received March 21, 2001

Abstract—Atomic force microscopy investigations revealed a change in the surface microrelief of the heteroepitaxial silicon films on sapphire substrates after pulsed X-ray irradiation at an energy of $E \leq 140$ keV.

The problem of increasing the stability of semiconductor devices with respect to the action of external factors (temperature, radiation, pressure) is currently important in modern microelectronics. Among various means of solving this problem, the main method consists in using structures of the "silicon on dielectric" type as a base for creating integrated circuits, whereby a thin silicon device layer is deposited onto single crystal (sapphire, spinel, etc.) or amorphous (SiO_2, Si_3N_4) dielectric substrates. Most widely used for the special-purpose intermediate-scale integrations are structures of the "silicon on sapphire" (SOS) type.

The heteroepitaxial character of the "device" layers in SOS structures accounts for a high level of residual stresses and structural defects in this system, which may lead to the development of aging process and degradation of the device parameters [1]. These negative phenomena may proceed in the SOS structures irradiated at both over- and subthreshold energy levels [2, 3]. The latter case is most interesting, since it is virtually not studied in practice and important from the standpoint of understanding the nature of degradation processes accompanying the low-energy irradiation.

The purpose of this study was to examine before and after X-ray irradiation the surface of 0.6-μm-thick (001)-oriented *n*-Si films grown by monosilane pyrolysis on 540-μm-thick α-Al_2O_3 $(01\bar{1}2)$ substrates. The samples were studied in a TMX-2100 Accurex scanning probe microscope operated in the noncontact atomic force microscopy (AFM) mode. The epitaxial heterostructures were irradiated from the side of silicon films in a pulsed mode by continuous X-ray radiation with $E_{max} \leq 140$ keV. The radiation pulse width was $\Delta t_r = 150$ ns, the fluence per pulse was 0.142–0.162 R, and the total fluence (irradiation dose) was 1.52 ± 0.46 R.

The experiments showed that the presence of a natural oxide layer on the initial silicon films changes the surface morphology by increasing the height of some roughnesses up to 50 nm at an average roughness of 8 nm (Fig. 1a). Depressions in the silicon dioxide layer contained "columnar" formations, presumably representing microinclusions of single-crystal SiO_2. Removal of the silicon dioxide layer by etching in a hydrofluoric acid decreased the maximum roughness height to 30 nm and the average surface roughness to 5 nm. This treatment also significantly changed the histogram of the lateral microrelief size distribution, the shape of which approached the Gauss curve (Fig. 1b). After X-ray irradiation of the films, the lateral microrelief size distribution shifted toward smaller dimensions, while the envelope shape became closer to the Poisson distribution. The maximum height of microroughnesses reached 40 nm, and the average roughness height increased to ~7 nm (Fig. 1c). Some local regions of silicon films in the irradiated structures contained islands possessing dimensions ranging within 0.1–0.3 μm with a [111] planar orientation (Fig. 2).

In addition to the AFM investigation, we have studied the silicon films by ellipsometry at a wavelength of $\lambda = 0.63$ μm using an LEF-601 instrument. These measurements showed that X-ray irradiation led to an increase in the index of refraction from $n_0 = 2.331$ to $n = 3.821$, while the extinction coefficient dropped from $k_0 = 3.006$ to $k = 1.770$. At the same time, the values of dispersion for both parameters increased by more than one order of magnitude. Changes in the *n* and *k* values not only proceed during the irradiation but continue after termination of the exposure and last for about one month in the samples kept under normal conditions.

The obtained results can be explained by changes in micromorphology of the film surface as a result of the dislocation structure rearrangement under the action of elastic waves (the dislocation density in heterostructures may reach up to 10^9–10^{10} cm^{-2} [1]). The elastic

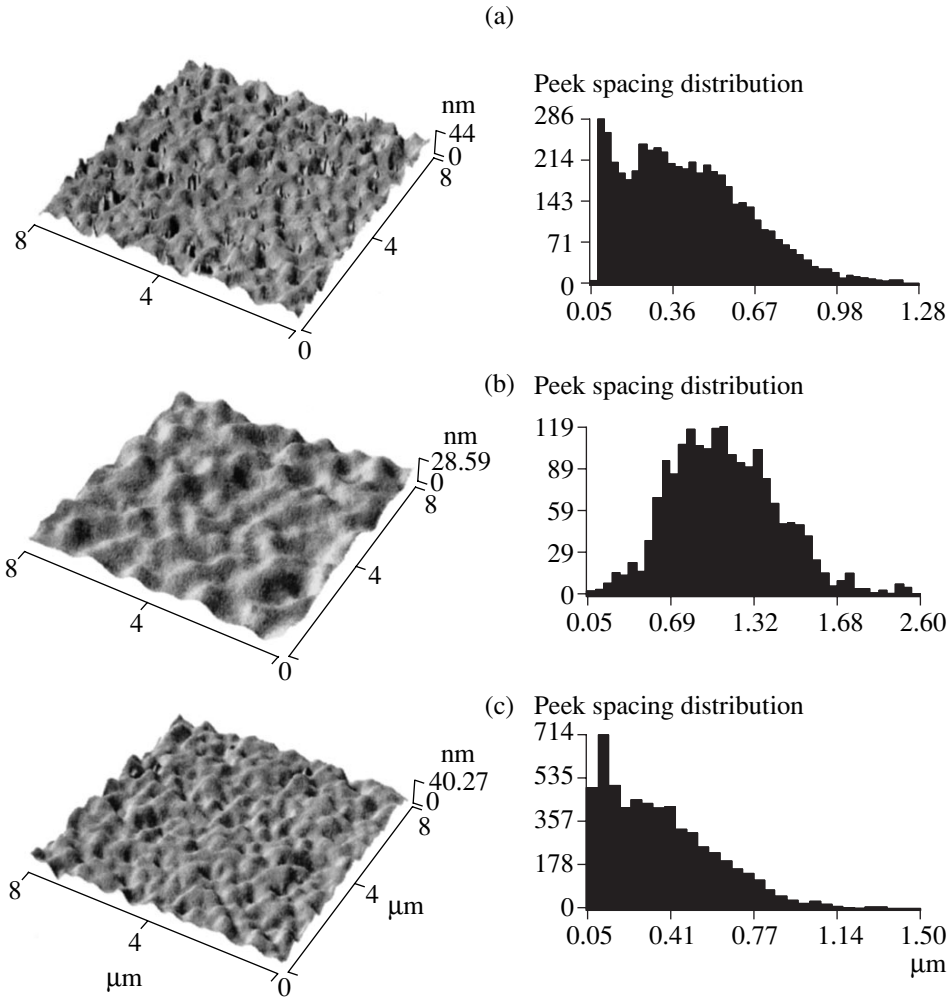

Fig. 1. AFM microtopographs and histograms of the lateral microrelief size distribution for SOS structures (a) in the initial state, (b) after silicon dioxide layer removal, and (c) after X-ray irradiation.

waves arise in the sapphire substrate due to the Coulomb repulsion of positively charged aluminum ions and oxygen ions ionized by the X-ray radiation. The pressure amplitude in the elastic wave originating from a single emission center can be evaluated as [4]

$$P_0 = \frac{q_1 q_2 e^2}{4\pi\varepsilon_0\varepsilon d^4},$$

where q_1 and q_2 is the multiplicity of ionization for the neighboring ions, e is the electron charge, ε_0 and ε are the permittivities of vacuum and substrate material, and d is the distance between ions. Ignoring the wave absorption in the heterostructure components and taking into account only waves generated in sapphire near the silicon film–substrate interface, the total pressure amplitude due to the jth source can be expressed as [5]

$$P = P_0 R[2\pi j\tau_i]^{1/2} = P_0 R[2\pi\tau\tau_i\sigma_i N_0 WDR]^{1/2},$$

where $R = \tau_i c$ is the size of the region of synchronous emission of the group of waves during the time τ_i of the electron excitation relaxation at the "selected" ion pair [4] (c is the speed of light), σ_i is the ionization cross section of the ith shell of oxygen ($\sigma \cong 10^{-18}$ cm^2 for the k-shell), N_0 is the number density of atoms (per unit volume), W is the probability of ionization of the ith level ($W \cong \exp\left\{-\frac{E_i}{E_0}\right\}$, E_i is the ionization energy of the ith level, and E_0 is the primary radiation energy), and D is the primary radiation flux density. For the X-ray radiation with $E_0 \le 2$ MeV, the latter quantity can be expressed as [6]

$$D = \frac{1.9\times 10^9}{\Delta t_r E_0}\left[\frac{\text{quanta}}{\text{cm}^2\ \text{s}}\right].$$

Calculations performed for a silicon film irradiated under the aforementioned conditions (assuming ioniza-

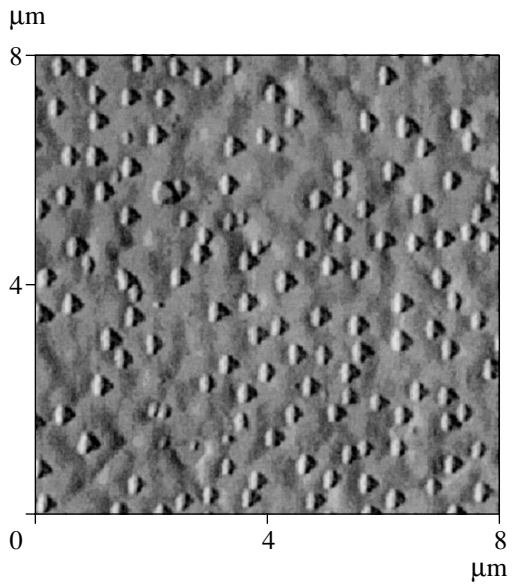

Fig. 2. An AFM microtopograph of the (001)-oriented surface of an irradiated silicon film showing [111]-oriented islands formed in the depressions.

tion of the oxygen *k*-shell, E_k = 0.532 keV) yield an effective pressure wave amplitude of $P \cong 6$ MPa. In a thin silicon layers with a strongly developed substructure, the action of such a pressure may lead to both a conservative and nonconservative rearrangement of dislocations, in particular, to the formation of 60° dislocation pileups at the {111} faces of the {001} octahedra near the film surface at the site of high initial local elastic stress development. Apparently, these very pileups and the related microcracks are observed in the form of [111]-oriented islands in the AFM topographs of the heterostructure surface.

REFERENCES

1. V. S. Papkov and M. B. Tsybul'nikov, *Epitaxial Silicon Layers on Dielectric Substrates and Related Devices* (Énergiya, Moscow, 1979).
2. A. S. Adonin, A. V. Bespalov, T. S. Kitichenko, *et al.*, Mikroélektronika **29** (4), 279 (2000).
3. S. V. Obolenskiĭ and V. D. Skupov, Poverkhnost, No. 5, 75 (2000).
4. M. I. Klinger, Ch. B. Lushchik, T. V. Mashovets, *et al.*, Usp. Fiz. Nauk **147** (3), 523 (1985) [Sov. Phys. Usp. **28**, 994 (1985)].
5. P. V. Pavlov, Yu. A. Semin, and V. D. Skupov, Fiz. Tekh. Poluprovodn. (Leningrad) **20** (3), 503 (1986) [Sov. Phys. Semicond. **20**, 315 (1986)].
6. V. L. Vinetskiĭ and G. A. Kholodar', *Radiation Physics of Semiconductors* (Naukova Dumka, Kiev, 1979).

Translated by P. Pozdeev

Technical Physics Letters, Vol. 27, No. 9, 2001, pp. 728–730. Translated from Pis'ma v Zhurnal Tekhnicheskoĭ Fiziki, Vol. 27, No. 17, 2001, pp. 40–45.

A Noncollinear Shear Surface Wave on a Moving Domain Boundary in a Ferromagnet

E. A. Vilkov, V. G. Shavrov, and N. S. Shevyakhov

Ul'yanovsk Department, Institute of Radio Engineering and Electronics, Russian Academy of Sciences, Ul'yanovsk, Russia

e-mail: ufire@mv.ru

Received February 17, 2001

Abstract—The possibility of the existence and the properties of a noncollinear shear surface wave on a moving domain boundary in a ferromagnet are considered. © *2001 MAIK "Nauka/Interperiodica".*

Noncollinear surface (boundary) waves were apparently originally described as a special object in [1], in the context of investigation of the parametric transformation of electroacoustic waves in a ferroelectric crystal by means of moving domain walls. The term "noncollinear wave" reflects the ability of an electroacoustic wave (established in [1] and refined in [2]) to deviate from its normal toward the direction of the domain wall (DW) motion while retaining the boundary localization and the stationary character of propagation (i.e., to be noncollinear with respect to the initial direction along DW observed in the static case).

An attempt to prove the existence of analogous noncollinear shear surface waves (NSSWs) on moving DWs in ferromagnets was made in [3]. However, an analysis of the dispersion relationship in that study was based on rather rough estimates obtained by the perturbation method, which hindered judging on the NSSW properties with sufficient clarity and reliability. In addition, a representation of the magnetostatic scattering fields employed in [3] essentially excluded the possibility of making allowance for the backscattered waves. In this study, both these disadvantages are removed and the complete spectrum of NSSWs existing on a moving DW in a cubic ferromagnetic crystal is described based on the exact quantitative calculation.

Consider a DW with an (010) orientation relative to the 0*y* axis of the laboratory *x*0*yz* frame of reference, and let this DW to move in the 0*y* direction at a velocity of $V_D < c_t$, where $c_t = (\lambda/\rho)^{1/2}$ is the shear wave velocity with neglect of the magnetostriction, λ is the shear modulus, and ρ is the ferromagnet density. Together with the frequency ω being selected below the forbidden band of the nonexchange spectrum of magnetoelastic waves, the above requirement of the structural stability of DWs in bulk (nonfilm) samples allows us to use the model of a geometrically thin DW with the current coordinate $y_D = V_D t$. Let the shear waves propagate in the *x*0*y* plane and possess shifts in the domains $\mathbf{u}_j \parallel z \parallel \mathbf{M}_s^{(j)}$ (where $M_s^{(1)} \uparrow\downarrow M_s^{(2)}$, $j = 1$ for $y > y_D$, $j = 2$ for $y < y_D$). The internal fields $\mathbf{H}_i^j \parallel z$ are determined by the anisotropic magnetic field H_a. For the 180° DW, we may write $M_s^{(j)} = (-1)^{j+1} M_s$, $H_i^{(j)} = (-1)^{j+1} H_a$, where M_s is the spontaneous magnetization.

Taking into account the above circumstance in the adopted propagation geometry and using the Maxwell equations, a linearized equation of motion of the magnetic moment, and the equation of motion of the theory of elasticity in a nonexchange magnetostatic approximation, we obtain the following initial system of equations:

$$\rho \frac{\partial^2 u_j}{\partial t^2} = \lambda \nabla^2 u_j + \frac{(-1)^{j+1}\beta}{4\pi M_s} \nabla^2 \varphi_j,$$
$$\left(\frac{\partial^2}{\partial t^2} + \omega_k^2\right) \nabla^2 \varphi_j = -4\pi\gamma\beta\omega_0 (-1)^{j+1} \nabla^2 u_j. \quad (1)$$

Here, ∇ is the Hamiltonian in the *x*0*y* pane; φ_j is the magnetostatic potential; $\omega_0 = \gamma H_a$ is the homogeneous precession frequency; $\omega_k = [\omega_0(\omega_0 + \omega_M)]^{1/2}$ is the magnetoacoustic resonance frequency; $\omega_M = 4\pi\gamma M_s$ is the magnetization frequency; γ is the gyromagnetic ratio; and β is the magnetoelastic coefficient. Using (by analogy with [1–3]) the method of transition to the frame of reference moving with DW, one may demonstrate, proceeding from (1) and assuming that only a low-frequency (quasi-acoustic) branch of the magnetoelastic wave spectrum ($\omega < \omega_k$) is activated and that the solution is limited, that there is a single possible NSSW representation:

$$\varphi_j = \Phi_j - \frac{4\pi\gamma\beta\omega_0(-1)^{j+1}}{\omega_k^2 + [i\omega + s(-1)^j V_D]^2} u_j,$$
$$u_j = U_j \exp i(kx + py - \omega t) \exp[(-1)^j s(y - y_D)], \quad (2)$$

$$\Phi_j = F_j \exp[i(kx - \Omega t)] \exp[(-1)^j |k|(y - y_D)].$$

In these expressions, Φ_j are the potentials of the scattering fields of the magnetic poles induced in DWs by the propagating NSSW; k and p have the meaning of the longitudinal and transverse components of the total NSSW wavevector $\mathbf{K} = \mathbf{k} + \mathbf{p}$; s is the NSSW amplitude decay coefficient; and Ω is the frequency of the NSSW oscillations in the DW rest system. Note that, due to the NSSW noncollinearity ($p \neq 0$), the frequencies of oscillations of the shear displacements and scattering potentials are different and related by a Doppler relationship $\omega = \Omega + \mathbf{K}\mathbf{V}_D = \Omega + pV_D$. Taking into account that expressions (2) describe a solution to Eqs. (1), we obtain the following relationships

$$p = \frac{V_D}{c_t}\frac{\omega}{c_t}\frac{\omega_k^2 - 2\omega^2 - s^2c_t^2(1 - 2V_D^2/c_t^2) + K^2c_t^2}{\omega_L^2 - \omega^2 + s^2V_D^2},$$

$$K^2 = (\omega_L^2 - \omega^2 + s^2V_D^2) \times \frac{(\omega_k^2 - \omega^2 + s^2V_D^2)[s^2(1 - V_D^2/c_t^2) + \omega^2/c_t^2] - \chi\omega_0^2 s^2}{(\omega_L^2 - \omega^2 + s^2V_D^2)^2 + 4s^2\omega^2V_D^2} + 4s^2\omega^2\frac{V_D^2}{c_t^2}\frac{\omega^2 - \chi\omega_0^2 + s^2c_t^2(1 - V_D^2/c_t^2)}{(\omega_L^2 - \omega^2 + s^2V_D^2)^2 + 4s^2\omega^2V_D^2}, \quad (3)$$

where $\omega_L^2 = \omega_k^2 - \chi\omega_0^2$ and $\chi = \gamma\beta^2/\lambda M_s\omega_0$ is the dimensionless magnetoelastic coupling constant of the ferromagnet.

A dispersion relationship for NSSWs follows from the condition of zero determinant of a system of homogeneous algebraic equations obtained by substituting expressions (2) into the standard boundary conditions of continuity for displacements, stresses, potentials, and normal magnetic induction components on the DWs. The resulting dispersion relationship can be reduced to the following form:

$$s + \frac{\chi\omega_0\sigma G(\omega, V_D)[(\omega^2 - s^2V_D^2 - \omega_k^2)^2 + 4s^2V_D^2\omega^2]}{[(\omega^2 - s^2V_D^2 - \omega_k^2)^2 + 4s^2V_D^2\omega^2] + \chi\omega_0^2[(\omega^2 - s^2V_D^2 - \omega_k^2) - 2pV_D\omega]}|k| = 0, \quad (4)$$

where $\sigma = k/|k|$ and $G(\omega, V_D)$ is the function describing reaction of the magnetic subsystem in the form of the scattering fields. The latter function is determined by the formula

$$G(\omega, V_D) = \frac{\omega^2 - s^2V_D^2 - \omega_k^2}{(\omega^2 - s^2V_D^2 - \omega_k^2)^2 + 4s^2V_D^2\omega^2} \times \left[\omega - \frac{\omega_0\omega_M(\omega - \sigma\omega_0)}{(\omega - \sigma\omega_0)^2 + s^2V_D^2} + \frac{\sigma\omega_M s^2V_D^2}{(\omega - \sigma\omega_0)^2 + s^2V_D^2} \times \frac{(\omega - \sigma\omega_0)^2 + s^2V_D^2 + \omega_0\omega_M}{(\omega - \sigma\omega_0)^2 + s^2V_D^2 - \sigma\omega_M(\omega - \sigma\omega_0)}\right] + \frac{2s^2V_D^2\omega}{(\omega^2 - s^2V_D^2 - \omega_k^2)^2 + 4s^2V_D^2\omega^2} \times \frac{(\omega - \sigma\omega_0)^2 + s^2V_D^2 + \omega_0\omega_M - 2\sigma\omega_M\omega}{(\omega - \sigma\omega_0)^2 + s^2V_D^2 - \sigma\omega_M(\omega - \sigma\omega_0)}. \quad (5)$$

The poles of the $G(\omega, V_D)$ function determine the ferromagnetic resonance (FMR) frequencies for the scattering fields

$$\omega = \sigma\omega_0 + \frac{\sigma\omega_M \pm \sqrt{\omega_M^2 - 4s^2V_D^2}}{2}, \quad (6)$$

where the zeros indicate the presence of an antiresonance response of the magnetic subsystem. Equation (6) only holds for the forward ($\sigma = 1$) waves; in the static case $V_D = 0$, this equation determines a spectral doublet $\omega = \omega_0$ and $\omega = \omega_0 + \omega_M$ of the magnetostatic surface waves on an immobile DW for the orthogonal propagation toward spontaneous magnetization fields in the domains [4].

Expressions (3) are conveniently used for sequentially excluding the quantities p and K^2 from (4), where $|k| = \sqrt{K^2 - p^2}$. The resulting one-dimensional nonlinear equation of the type $\mathcal{F}(\omega, s) = 0$ can be solved by standard numerical methods, which allows the s value to be determined using a given frequency ω. Then we may substitute ω and s back into Eq. (3) to find all other NSSW characteristics. A typical NSSW spectrum presented in the figure refers to the most interesting case of close χ and ω_M/ω_0 values. The horizontal dashed lines I and III indicate the FMR frequency ω_0 for the forward waves ($k > 0$) and the frequency of truncation of the spectrum of backscattered ($k < 0$) waves $\omega^* = \omega_0(\sqrt{1 + 4\omega_M/\omega_0} - 1)/2$ (reflecting the antiresonance response of the magnetic subsystem). Since the ω^* value is usually smaller than ω_L, the spectrum of backscattered NSSWs weakly localized on DW (see the dashed line for $V_D = 0$ and the solid line for $V_D \neq 0$ at $k < 0$) is virtually identical to the acoustic spectrum. An increase in the slope of the quasi-acoustic parts of this spectrum as a result of the DW motion (this effect takes

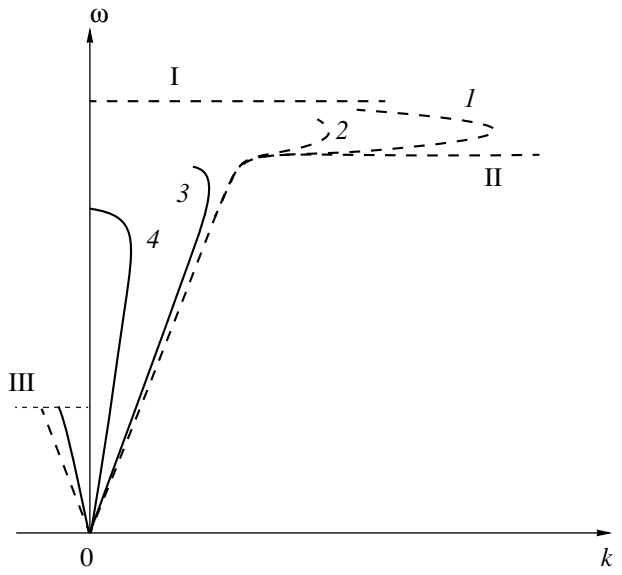

Total spectrum of a noncollinear shear surface wave on a moving domain wall in a ferromagnet: (*1*, *2*) slow ($V_D \ll c_t$) DW motions; (*3*) moderate DW velocity; (*4*) fast DW motion ($V_D \simeq c_t$) at a subsonic velocity.

place for curves *1–4* enumerated in the order of increasing velocity of the DW motion; dashed curve II corresponds to the case $V_D = 0$) is related to an invariance of k (but not of K) with respect to V_D variations.

An analysis of the behavior of the dispersion curves *1–4* shows that the main changes in the spectrum under the action of DW motions take place within a narrow frequency band (in the figure this band is depicted in a greater scale): $\omega_0(1 - \chi) \le \omega \le \omega_0$. The DW motion at a small velocity (see the fragments of branches *1* and *2*) leads to a looplike deviation of these branches from the shortwave asymptotic limit of the NSSW spectrum on a static DW (dashed line II) to FMR I level (this deviation is characteristic of a twofold degeneracy of modes). The elongation of loops toward the shortwave side of the spectrum increases with decreasing V_D. This circumstance suggests the possibility of violation of the geometric DW criterion. At the turning point of the loop (representing a root singularity of the modes I and II degenerate as a result of the DW motion; the role of these modes is the same as that of the doublet of FMR, lines in the spectrum of magnetostatic surface waves on the moving DW [5]), the NSSW group velocity exhibits a break and the boundary localization of this wave becomes maximum (the NSSW localization depth at this point is on the order of the wavelength).

Curves *1–3* terminate (being truncated) at the points where the total NSSW wavenumber K coincides with the wavenumber of the magnetoelastic shear bulk wave and $s \equiv 0$. The asymptotic part of the spectrum of the latter wave for $\chi \ll \omega_M/\omega_0$ is situated well above the FMR level and the curves of types *1* and *3* will terminate on the FMR curve. An exception is offered by the dispersion branches of the type of curve *4* corresponding as a rule to the subsonic regimes of DW motion and lying above the linear part of the spectrum of the magnetoelastic shear bulk wave (a specific branch of "fast" NSSWs existing only on a moving DW and characterized by weak boundary localization). These branches always terminate on the frequency axis at the points $s = 0$, $K \equiv p$, where the binding of NSSW to DW by magnetic bands ceases because the wave front is parallel to DW. An analogous (but not complicated by the frequency dispersion) detachment of the electroacoustic wave from a moving DW in a ferroelectric crystal (essentially degeneracy of NSSW into a bulk shear wave) was observed in [2].

Acknowledgments. this study was supported by the Federal Targeted Program "Integration," project no. A 0066.

REFERENCES

1. N. S. Shevyakhov, Akust. Zh. **45** (4), 570 (1999) [Acoust. Phys. **45**, 509 (1999)].
2. Yu. V. Gulyaev, O. Yu. El'meshkin, and N. S. Shevyakhov, Radiotekh. Élektron. (Moscow) **45** (3), 351 (2000).
3. E. Vilkov, V. Shavrov, and N. Shevyakhov, in *Proceedings of the Moscow International Symposium on Magnetism, Moscow, 1999*, Part 2, p. 209.
4. I. A. Gilinskiĭ and R. G. Mints, Zh. Éksp. Teor. Fiz. **59** (4), 1230 (1970) [Sov. Phys. JETP **32**, 673 (1971)].
5. E. A. Vilkov, Pis'ma Zh. Tekh. Fiz. **26** (20), 28 (2000) [Tech. Phys. Lett. **26**, 907 (2000)].

Translated by P. Pozdeev

Technical Physics Letters, Vol. 27, No. 9, 2001, pp. 731–733. Translated from Pis'ma v Zhurnal Tekhnicheskoĭ Fiziki, Vol. 27, No. 17, 2001, pp. 46–50.

High-Voltage GaAs Diodes with Subnanosecond Gate Voltage Recovery

V. I. Korol'kov, A. V. Rozhkov, and L. A. Petropavlovskaya

Ioffe Physicotechnical Institute, Russian Academy of Sciences, St. Petersburg, 194021 Russia

Received April 4, 2001

Abstract—High-voltage GaAs switching diodes with subnanosecond characteristic times of reverse current decay on switching from forward to reverse bias were studied. The diode structures studied had impurity concentration profiles in the base region close to those of the charge-storage diodes and operated in the regimes corresponding to those employed in silicon-based high-voltage fast-recovery drift diodes. The application prospects of the proposed GaAs diodes are demonstrated, for example, in the devices generating pulses with a front width of several hundred picoseconds, a current of several hundred amperes, and a voltage of a several kiloelectronvolts at a frequency of up to several hundred kilohertz. © *2001 MAIK "Nauka/Interperiodica".*

Most of the semiconductor switching devices with positive current feedback (avalanche transistors, thyristors, dinistors, etc.) are highly sensitive to the current localization effects [1, 2]. As a rule, the switching inhomogeneities lead to a catastrophic degradation development and device failure. These current instability problems are absent in devices where the switching process occurs during a single period of carrier transit through the base region. This class of switching devices includes charge-storage diodes (CSDs) [3], fast-recovery drift diodes (FRDDs) [4], and some other diode structures used for the generation of pulses with steep fronts.

We have studied p^+–p–i–n–n^+ diode structures grown by liquid-phase epitaxy (LPE) from a limited volume of GaAs solution melt in gallium. The depth-concentration profiles of impurities in the –*p*-, –*i*-, and –*n*-layers were typical of the CSD structures [3]. The dopant concentration gradient in the base regions reached three orders of magnitude: from a residual impurity concentration $\ll 10^{14}$ cm^{-3} in the *i*-layer to $\sim 5 \times 10^{16}$ cm^{-3} at the n–n^+ interface. The sample diode structures had the following geometric characteristics: $W_p = 30$ μm; $W_i + W_n = 60$ μm; diode diameter, ≅1 mm. The nonequilibrium carrier lifetimes τ_p measured in the *n*-base layer by the Lacks method did not exceed 100 ns. The maximum gate voltages in the diodes studied were ~1 kV.

The process of pulse formation in the switching diodes described in detail in [3–5] consists of two characteristic stages. Since some features of these stages are important for understanding the results of our experiments and the parameters controlling the switching process are employed in the data presentation, we will briefly characterize the two steps of switching.

In the first stage, the diode transmits a forward current pulse with the duration (t_F) and amplitude (I_F) determining the efficiency of the diffusion modulation in the base region. The depth L_D of the nonequilibrium carrier penetration into the base region was limited ($L_D \ll W$, W being the base region size) both by the forward current pulse duration ($t_F \le \tau_p$, as in FRDDs) and by the electric field (related to the dopant concentration gradient) hindering the nonequilibrium carrier penetration deep into the base (as in CSDs). At the same time, the amount of charge accumulated in the diffusion region was controlled by the amplitude of the forward current, the density of which could be varied from 20 to 500 A/cm^2. In our experiments, the forward current pulse duration was ~100 ns (Fig. 1) and the charge Q_F accumulated during passage of the forward current varied from 50 to 250 nC.

In the second stage, the diode structure switches from forward to reverse bias and the nonequilibrium carriers are dissipated in the diffusion region. The loss rate of holes via the p–n junction is controlled predominantly by the reverse current buildup rate, that is, by the reverse voltage pulse parameters. In our experi-

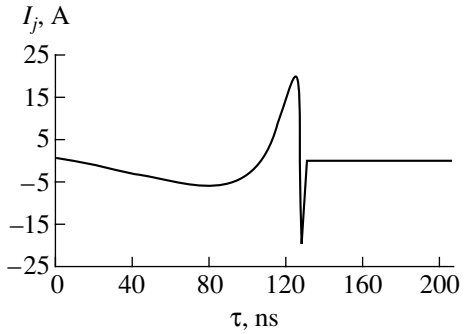

Fig. 1. A typical oscillogram of the current illustrating two stages of the switching process in p^+–p–i–n–n^+ GaAs-based diode structures.

1063-7850/01/2709-0731$21.00 © 2001 MAIK "Nauka/Interperiodica"

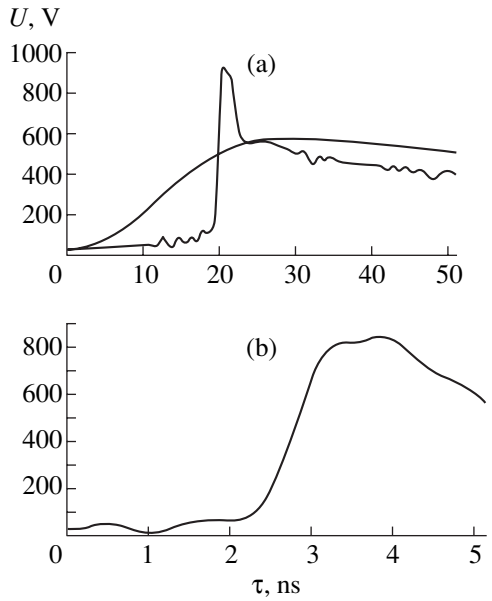

Fig. 2. A typical oscillogram of the voltage pulse measured in a 50-Ω load: (a) initial switching pulse; (b) output pulse formed in a p^+–p–i–n–n^+ GaAs-based diode structure.

ments, the reverse voltage buildup time t_R was about 20 ns (Fig. 1), which is mach smaller as compared to the nonequilibrium carrier lifetime in the base region. Since the charge carried by the reverse current I_R in switching diodes corresponds to Q_F, the reverse current amplitude by the time t_0 when the hole concentration decays to zero is strictly controlled by the amplitude and duration of the forward current pulse. Beginning with t_0, the diode features recovery of the voltage drop across the appearing space charge region. The reverse current decay time corresponds to the front width Δt of the voltage pulse formed in the load. Figure 2 shows a typical oscillogram of the voltage pulse measured in a 50-Ω load and the shape of the initial switching pulse. The curves show evidence of a subnanosecond voltage buildup in the diode studied. Such times correspond to the carrier drift velocity in the base region, $V_n = j/q(p + n)$, the maximum values of which a limited by the saturation velocity $V_s = 10^7$ cm/s.

One might expect that the diodes studied (with a variable impurity depth–concentration profile in the base region different from that typical of FRDDs) would exhibit a more complicated dependence of the carrier drift velocity on the reverse current density. However, some general trends (in common with the silicon-based FRDDs) in the voltage recovery rate variation dU/dt were still retained in the GaAs switching diodes under consideration. For example, an increase in the reverse current and the reverse voltage amplitude led to an increase in dU/dt, while an increase in the reverse voltage buildup time t_R reduced the dU/dt value. At the same time, we established a number of particularities.

(i) An increase in the reverse current was not accompanied by the limitation of the voltage recovery rate dU/dt in a broad range of current densities (up to 2000 A/cm^2). The ratio of the values of voltage at the time instants corresponding to the gate voltage buildup start (t_0) and finish ($t_0 + \Delta t$) remained virtually unchanged in a wide range of the reverse current densities. A characteristic "pedestal" preceding the subnanosecond voltage growth did not exceed 75–80 V at a reverse current density of 1500A/cm^2.

(ii) The duration of the reverse voltage recovery stage reached subnanosecond values beginning with a reverse current density of ~100 A/cm^2 and did not exceed 0.5 ns at a current density of 2000 A/cm^2.

(iii) Despite a small nonequilibrium carrier lifetimes in the base n-layer ($\tau_p \le 100$ ns), the reverse voltage buildup rate depended on the forward current pulse duration. Indeed, the reverse voltage recovery time observed for $t_F \sim \tau_p$ amounted to several hundred picoseconds already at a reverse current density of ≥100 A/cm^2; in the regime of dc forward pumping, the voltage recovery times exceeded 2 ns even for a reverse current density of ~1000 A/cm^2.

The results presented above demonstrated the possibility of using the effect of field-induced nonequilibrium carrier dissipation in GaAs diodes for the formation of high-voltage pulses with nanosecond pulse front duration. A remarkable feature is that the range of working current densities is expanded up to 2000 A/cm^2 (exceeding more than one order of magnitude the value for silicon-based FRDDs). The modern technology of GaAs-based high-voltage p–n junctions provides for the materials with injection and gating properties sufficiently homogeneous in the device plane, which makes it possible to obtain diodes with a diameter of 5 mm and above. Such diodes are capable of switching current pulses several hundred amperes in amplitude. According to the results of our preliminary experiments, a serial array of three switching diodes ensured their synchronous switching at a voltage pulse amplitude of 2.5 kV.

In the course of our experiments, the switching diodes operated at temperatures well above 100°C. This is important because, even for GaAs possessing a small thermal conductivity, the high working temperatures allow us to expect that the good switching properties will be retained even at very high pulse repetition frequencies. Estimates showed that the maximum working frequencies limited by heat evolution may reach up to several hundred kilohertz.

Acknowledgments. The authors are grateful to V.A. Kozlov for fruitful discussions in the preliminary stage of work and to S.V. Shendereĭ for valuable advice, interest in this study, and discussion of results.

REFERENCES

1. S. A. Garyainov and I. D. Abezgauz, *Semiconductor Devices with Negative Resistance* (Énergiya, Moscow, 1970).
2. A. V. Gorbatyuk, Preprint No. 962 (Leningrad, 1985).
3. S. A. Eremin, O. K. Mokeev, and Yu. R. Nosov, *Semiconductor Charge-Storage Diodes* (Sov. Radio, Moscow, 1966).
4. I. V. Grekhov, V. M. Efanov, A. F. Kardo-Sysoev, and S. V. Shendereĭ, Pis'ma Zh. Tekh. Fiz. **9** (7), 435 (1983) [Sov. Tech. Phys. Lett. **9**, 188 (1983)].
5. V. M. Tuchkevich and I. V. Grekhov, *Novel Principles of High-Power Switching by Semiconductor Devices* (Nauka, Leningrad, 1988).

Translated by P. Pozdeev

Technical Physics Letters, Vol. 27, No. 9, 2001, pp. 734–736. Translated from Pis'ma v Zhurnal Tekhnicheskoĭ Fiziki, Vol. 27, No. 17, 2001, pp. 51–56.

1.55–1.6 μm Electroluminescence of GaAs Based Diode Structures with Quantum Dots

A. E. Zhukov, B. V. Volovik, S. S. Mikhrin, N. A. Maleev, A. F. Tsatsul'nikov, E. V. Nikitina, I. N. Kayander, V. M. Ustinov, and N. N. Ledentsov

Ioffe Physicotechnical Institute, Russian Academy of Sciences, St. Petersburg, 194021 Russia

Received April 24, 2001

Abstract—Laser diode structures on GaAs substrates with an active region employing laterally associated InAs quantum dots obtained by low-temperature MBE exhibit electroluminescence at a wavelength of 1.55–1.6 μm in a temperature range from 20 to 260 K. © *2001 MAIK "Nauka/Interperiodica".*

In recent years, considerable attention has been devoted to the development of longwave lasers operating in the region of 1.3 and 1.55 μm wavelengths. These sources, intended for use in fiber optic communication lines, have to replace the existing edge-emitting laser diodes based on materials of the InGaAsP/InP system [1]. In this context, of special interest are the investigations aimed at creating surface-emitting lasers on GaAs substrates. Using GaAs-based materials, it is quite easy to form a high-*Q* resonator with the aid of distributed Bragg mirrors based on Al(Ga)As/GaAs or Al(Ga)O/GaAs. The main problem, however, is to select a proper material and find the corresponding epitaxial growth conditions for obtaining an active region capable of emitting in the aforementioned wavelength range. Indeed, even the well developed technology of InGaAs quantum dots does not allow us to create effective sources operating at a wavelength longer than 1.2 μm.

The main approaches used to move into the region of long wavelengths with GaAs-based materials are still related to employing nitrogen-containing InGaAsN structures with In(Ga)As quantum dots (QDs). Both technologies were demonstrated to provide for the obtaining of monolithic surface-emitting lasers operating at a 1.3-μm wavelength in a continuous single-mode regime with a room-temperature output power of 550 μW (InGaAsN, 1.284 μm [2]), 650 μW (InAs/InGaAs QD, 1.305 μm [3]), and 750 μW (InGaAsN, 1.269 μm [4]).

At the same time, achievements in the region of 1.55 μm are much less significant. Systems based on the nitrogen-containing compounds were demonstrated to produce room-temperature photoluminescence at 1.52 μm in the structures with InGaAsN quantum dots [5] and GaAsSbN quantum wells [6]; laser generation was observed in a diode structure with InGaAsN quantum wells [7]. In the latter case, a threshold current density was 47 kA/cm^2 probably because of a poor quality of highly stressed $GaIn_{0.38}AsN_{0.05}$ quantum dots with a high nitrogen content. The optical range achievable with GaAs can be significantly increased using InAs quantum dots deposited at low temperatures (320–350°C). Recently [8], we observed a room-temperature photoluminescence in the 1.65–1.72 μm range. However, to our knowledge, no data on the elec-

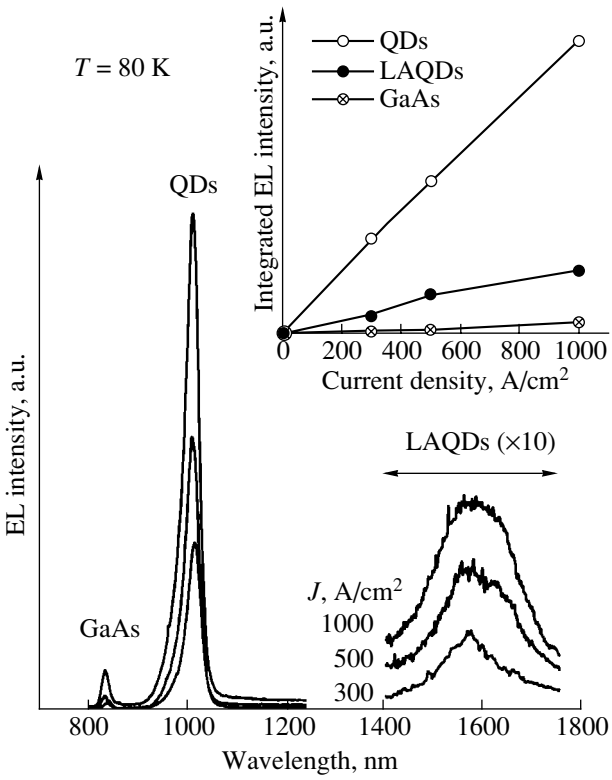

Fig. 1. The EL spectra of laser diode heterostructures measured at 80 K for various pumping current densities. The EL bands due to the recombination of charge carriers in the GaAs matrix and the emission from spatially separated and laterally associated quantum dots are denoted by GaAs, QD, and LAQD, respectively. The inset shows the plots of integral EL intensity versus pumping current density for the three emission components.

1063-7850/01/2709-0734$21.00 © 2001 MAIK "Nauka/Interperiodica"

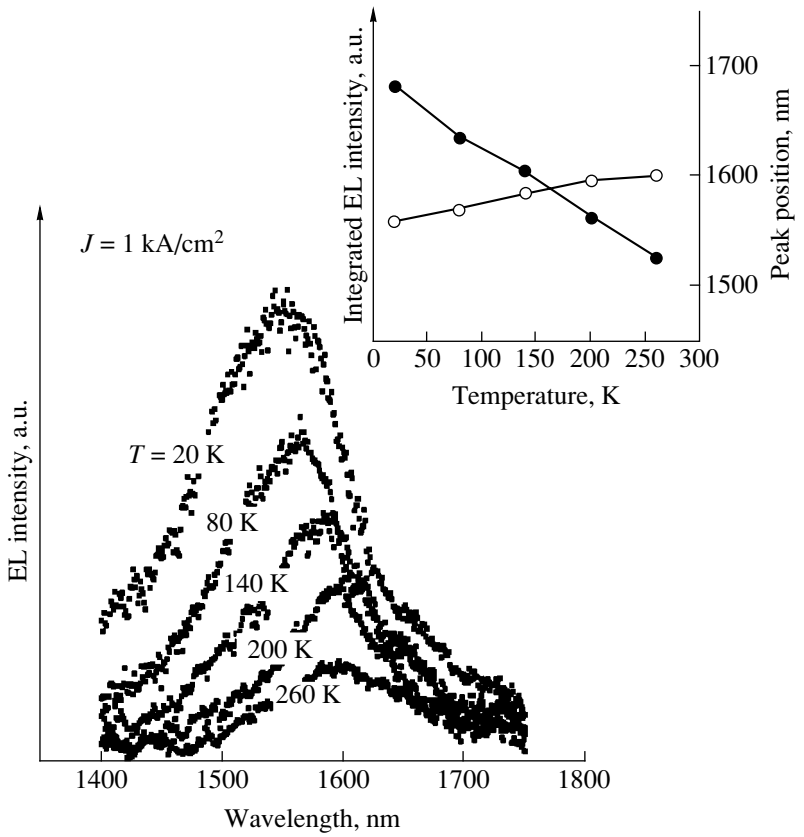

Fig. 2. The EL spectra in the region of emission from laterally associated quantum dots (LAQDs) measured at a constant pumping current density (1 kA/cm^2) and various temperatures. The inset shows the plots of integral intensity and LAQD emission peak position versus temperature.

troluminescence in such structures were published so far.

Below, we report for the first time on the electroluminescence (EL) observed in a 1.55–1.6 μm wavelength range in GaAs-based structures with a nitrogen-free active region.

In the system studied, the active region was based on the self-organizing arrays of InAs quantum dots formed by molecular beam epitaxy (MBE) at a substrate temperature of 320°C. As was demonstrated in [8], the low-temperature MBE growth of InAs leads to the formation of both spatially isolated islands (quantum dots emitting at a wavelength of 1–1.1 μm) and the conglomerates of such islands connected in the interfacial plane. These laterally associated quantum dots (LAQDs) are responsible for the appearance of a long-wave band with a maximum in the range 1.55–1.75 μm depending on the deposition parameters (amount of deposited InAs and substrate temperature).

The epitaxial growth was effected in a Riber 32P MBE system with solid sources. An active region containing five layers of low-temperature-grown QDs separated by 50-nm-thick GaAs interlayers was confined between doped (5×10^{17} cm^{-3}) $Al_{0.3}Ga_{0.7}As$ layers that served as charge carrier injectors. The contacts were fused into *n*-GaAs substrate and a *p*-GaAs overlayer. The electroluminescence was studied in a temperature range from 20 to 260 K using the diode structures excited by current pulses at a frequency of 5 kHz and a pulse duration of 0.3 μs. The emission was detected by a cooled Ge photodiode (North Coast).

Figure 1 shows the EL spectra of diode heterostructures measured at 80 K for various pumping current densities. The spectra display three EL bands in the regions of 800–850, 900–1100, and 1400–1750 nm attributed to the recombination of charge carriers in the GaAs matrix and the emission from spatially separated QDs and laterally associated QDs. The LAQD emission band maximum at this temperature is observed at 1.57 μm. The integral EL intensities in the three spectral regions are presented as functions of the pumping current densities in the inset to Fig. 1. The band of the spatially separated QDs dominates in the EL spectra, exceeding the LAQD emission in the total intensity by a factor of about five. We believe that this difference is explained by different surface densities of the corresponding QDs (5×10^{10} versus $1–2 \times 10^{10}$ cm^{-2}, respectively). The integral EL intensity of the 1.57-μm band related to LAQDs increases virtually linearly with the pumping current density in the entire range studied (up to 1 kA/cm^2).

Figure 2 shows the EL spectra in the region of LAQD emission measured at a constant pumping current density (1 kA/cm^2) and various temperatures in the 20–260 K range. The integral intensity of the LAQD emission band decreases exponentially with the temperature, while the EL peak position gradually shifts toward longer wavelengths. The full width at half maximum (FWHM) of this band amounts to about 120 nm and is virtually independent of the temperature. This indicates that the QD size scatter is the main factor responsible for the broadening of the LAQD emission band.

The maximum temperature at which the LAQD emission band intensity significantly exceeded the noise level of the experimental setup was 260 K. The peak of this band was observed at 1.6 μm. To our knowledge, this is the maximum wavelength in the near IR range for all current-pumped GaAs-based laser diode structures reported so far.

Thus, we have demonstrated the possibility of significantly increasing the wavelength attainable with GaAs-based structures directly pumped by a pulsed current. The EL band of laterally associated InAs quantum dots formed by low-temperature MBE is observed in a wavelength range of 1.55–1.6 μm at temperatures up to 260 K. Although the emission bend due to spatially separated QDs dominates in the EL spectrum, the active region of the proposed heterostructures shows good prospects for use in the vertically emitting lasers and LEDs for the 1.55-μm range because a desired emission component can be selectively amplified (attenuated) with the aid of an optical microresonator.

Acknowledgments. This study was supported by the Federal Program "Physics of Solid State Nanostructures" (project no. 99-2014), by the Russian Foundation for Basic Research (project no. 00-02-17006a), and by the NanOp Program.

REFERENCES

1. V. M. Ustinov and A. E. Zhukov, Semicond. Sci. Technol. **15**, R41 (2000).
2. G. Steinle, H. Riechert, and A. Yu. Egorov, Electron. Lett. **37** (2), 93 (2001).
3. J. Lott, N. Ledentsov, V. M. Ustinov, *et al.*, in *Proceedings of the IEEE LEOS 13th Annual Meeting, Río Grande, Puerto Rico, 2000*, IEEE Catalog Number: OOCH37080, p. 304.
4. A. W. Jackson, R. L. Naone, M. J. Dalberth, *et al.*, Electron. Lett. **37** (6), 355 (2001).
5. M. Sopanen, H. P. Xin, and C. W. Tu, Appl. Phys. Lett. **76** (8), 994 (2000).
6. G. Ungaro, G. Le Roux, R. Teissier, and J. C. Harmand, Electron. Lett. **35** (15), 1246 (1999).
7. M. Fischer, M. Reinhardt, and A. Forchel, Electron. Lett. **36** (14), 1208 (2000).
8. M. V. Maximov, A. F. Tsatsul'nikov, B. V. Volovik, *et al.*, Appl. Phys. Lett. **75** (16), 2347 (1999).

Translated by P. Pozdeev

Technical Physics Letters, Vol. 27, No. 9, 2001, pp. 737–739. Translated from Pis'ma v Zhurnal Tekhnicheskoĭ Fiziki, Vol. 27, No. 17, 2001, pp. 57–62.

On the Mechanism of Laser-Induced Graphite Conversion into Pyrocarbon in a Subsurface Layer of Cast Iron

G. I. Kozlov

Institute for Problems of Mechanics, Russian Academy of Sciences, Moscow, Russia

Received March 11, 2001

Abstract—Based on the original experimental results and on the analysis of published data, the author suggests a consistent variant of the possible mechanism of carbon phase transitions in a subsurface layer of cast iron subjected to a special laser treatment. The phase transitions involve the formation of carbyne followed by its decomposition during cooling and conversion into pyrocarbon. © *2001 MAIK "Nauka/Interperiodica".*

Previous communications [1, 2] reported on the formation of superhard structures in a subsurface layer of copper-plated gray iron under conditions of a special laser processing. The formation of superhard structures was accompanied by phase transformations, whereby graphite contained in the cast iron converts into pyrocarbon. The latter carbon phase possesses a globular shape, which indicates that the formation of pyrocarbon involves several phase transitions including the graphite conversion into liquid state. Then a question naturally arises as to whether such a liquid graphite can exist?

An analysis presented below for the first time gives some considerations concerning the formation of pyrocarbon and the possible molecular structures of liquid carbon corresponding to various values of thermodynamic parameters.

An analysis of the microstructure of the zone of laser action (Fig. 1) shows that the formation of globules (some of which possess a nearly spherical shape) in a melted subsurface layer of cast iron under laser treatment conditions is actually indicative of the possible existence of a liquid phase. However, it was necessary first to check for the elemental composition of the globules. For this purpose, the globules were studied in a scanning electron microscope of the CAMSCAN CS44C-100S type equipped with an energy-dispersive LINC ISIS–L200D X-ray analyzer. This analysis showed that some globules are composed of virtually pure carbon, whereas the others contain impurities of silicon (up to 7.1%), chromium (up to 4.5%). and iron (up to 1.1%). This difference in the elemental composition of various globules is probably related to the dynamics of the whole pattern of phase transitions and diffusion processes accompanying the laser processing. An increase in the duration of this treatment will apparently lead to a decrease in the impurity concentration. Thus, we may consider the globules as carbon structures formed from melt.

The question concerning the possible existence of a liquid graphite phase, which was repeatedly formulated by various researchers, still remained unanswered. Until recently, it was believed that graphite heated above 3800 K at a normal pressure exhibits sublimation and (bypassing the liquid state) converts into a vapor state. However, when graphite is heated up to the high temperatures indicated above at a pressure exceeding 100 atm, the graphite exhibits a transition to a liquid state. Hence, the melted graphite can actually be obtained. Indeed, evidence of the graphite fusion was reported by some researchers studying the phenomenon of laser-induced graphite heating at pressures $p >$ 100 atm. An exhaustive review of such experiments can be found, e.g., in [3]. Asinovskiĭ *et al.* [4] suggested that the fusion of graphite can take place below $p <$ 100 atm, but the traces of this phenomenon are difficult to detect because the melted carbon film is very thin and evaporates immediately upon the formation. By extrapolating the curves of the phase equilibria corre-

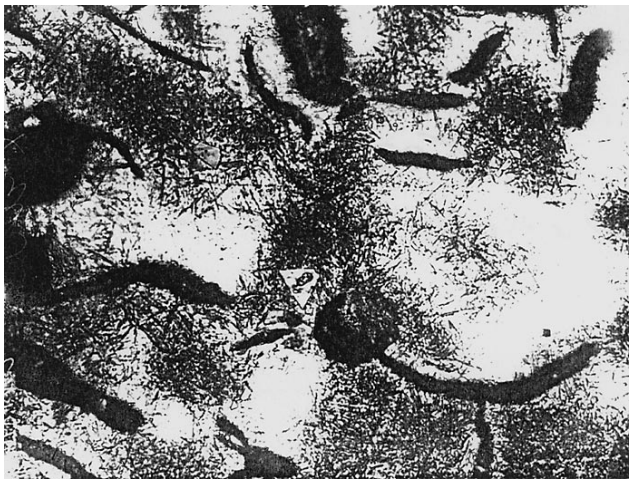

Fig. 1. Micrograph of the zone of laser action showing carbon globules (magnification, ×400).

1063-7850/01/2709-0737$21.00 © 2001 MAIK "Nauka/Interperiodica"

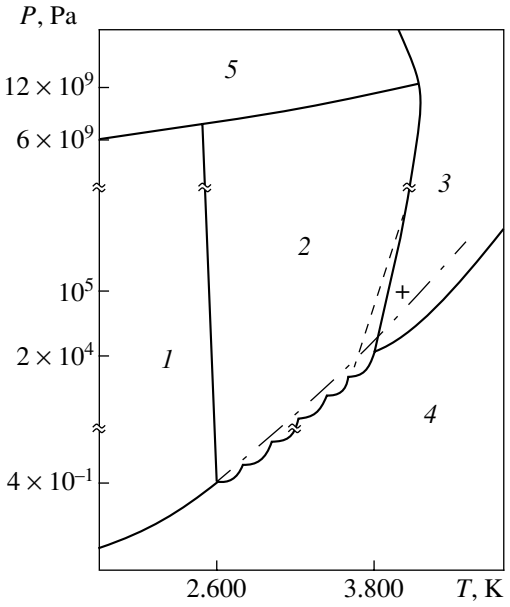

Fig. 2. The phase diagram of carbon proposed by Whittaker [5] and modified so as to take into account the triple point (+) determined in [4]: (*1*) graphite; (*2*) carbyne; (*3*) liquid; (*4*) vapor; (*5*) diamond.

sponding to graphite melting and boiling, the same researchers recently determined coordinates of the "solid–liquid–vapor" triple point which correspond to $p_+ = 1$ atm and $T_+ = 4000$ K. It should be emphasized that these values significantly differ from those reported previously ($p_+ = 100$ atm; $T_+ = 5000$ K).

However, the possibility that the laser-induced graphite heating may give rise to a phase transformation with the graphite conversion to carbyne was not considered in [4]. Therefore, it is not quite clear which crystalline and liquid phases refer to the aforementioned triple point and whether a considerable scatter in the triple point coordinates evidenced above can be due to these changes in the phase composition. In this context, it should be noted that the phase transition from graphite to carbyne may only partly take place during the laser pulse action upon the graphite surface. Therefore, a graphite–carbyne mixture of a certain composition is probably formed in the laser action zone, to which the above parameters p_+ and T_+ may refer. Since the composition of this mixture in different experiments may vary, this circumstance probably accounts for the aforementioned significant scatter in the values of p_+ and especially T_+.

An analysis of the phase diagram of carbon proposed by Whittaker [5] and modified so as to take into account the triple point determined in [4] (Fig. 2) shows that, at temperatures above 2600 K, graphite converts into carbyne and, hence, cannot exist in the liquid form. In addition, the phase diagram indicates that carbyne is stable at temperatures from 2600 to 3800 K in a broad range of pressures (up to the boundary of the diamond region). The triple-point parameters in the carbyne region somewhat differ from the values given above and amount to $p_+ = 0.2$ atm and $T_+ = 3800$ K. Therefore, carbyne heated above 3800 K converts into liquid. It was sometimes pointed out that the liquid carbyne must be transparent, colorless, and possess low emission properties, which agrees with a remark made in [6] about a "sufficiently transparent" film of melted carbon. From this we may infer that the triple-point coordinates determined in [4] probably also refer to carbyne. Thus, a carbyne rather than graphite liquid must exist in this system! By the same token, a diamond liquid must exist at the diamond phase boundary at still higher pressures! Of course, all these considerations are only valid provided that the hypothetical Whittaker's carbon phase diagram reflects real pattern and the carbyne region does in fact exist.

It should be emphasized that the existence of carbyne is not seriously doubted at present. This substance, found under natural conditions, is obtained in the form of thin films using a special laboratory technology. As is seen from the phase diagram of carbon presented in Fig. 2, carbyne can be obtained provided that two conditions are satisfied: first, it is necessary to reach a region of the phase diagram of carbon in which carbyne is a thermodynamically stable phase; second, this carbyne phase has to be retained in the course of cooling down to normal conditions (this implies a relatively rapid quenching, since a gradual decrease in the temperature may give rise to reverse processes in which carbyne readily decomposes and converts into graphite). According to [5], the ratio of the forward and reverse reactions (of the carbyne formation and decomposition, respectively) is approximately 1 : 500. It is the high decomposition rate of carbyne that allows this carbon phase to be obtained only in the form of thin films on a substrate.

As for the molecular structure of carbyne, note that the dissociation of graphite at temperatures above 2600 K involves the breakage of simple bonds and the formation of long molecular chains with triple bonds. These chains may associate to form a hexagonal structure of some carbyne modification. Upon the formation of triple bonds, atoms in the chain come closer to one another and the density of carbyne significantly increases as compared to that of graphite. Indeed, the densities of various carbyne modifications range from 2.68 to 3.43 g/cm^3, while the density of graphite never exceeds 2.25 g/cm^3. The triple bond formation indicates that liquid carbyne must be composed of molecules of the polyine type $(–C\equiv C–)_n$ stable at high temperatures.

The whole body of data presented above suggests that, under the conditions of our experiments on the laser treatment of a cast iron surface, graphite occurring in the subsurface layer is heated in globules and converted into carbyne (or carbyne liquid if the temperature is sufficiently high). During the subsequent sponta-

neous cooling of the subsurface layer, carbyne decomposes and converts into a nontransparent pyrocarbon representing a mixed carbyne–graphite structure. The experiments are in progress and the detailed results will be reported in the journal *Technical Physics* (Zhurnal Tekhnicheskoi Fiziki).

Acknowledgments. This study was partly supported by the Russian Foundation for Basic Research, project no. 00-01-00212.

REFERENCES

1. G. I. Kozlov, Pis'ma Zh. Tekh. Fiz. **25** (24), 61 (1999) [Tech. Phys. Lett. **25**, 997 (1999)].
2. G. I. Kozlov, Pis'ma Zh. Tekh. Fiz. **26** (11), 84 (2000) [Tech. Phys. Lett. **26**, 490 (2000)].
3. M. A. Sheĭndlin, Teplofiz. Vys. Temp. **10** (3), 630 (1981).
4. É. I. Asinovskiĭ, A. V. Kirillin, and A. V. Kostanovskiĭ, Teplofiz. Vys. Temp. **35** (5), 716 (1997).
5. A. G. Whittaker, Nature **276**, 695 (1978).
6. É. I. Asinovskiĭ, A. V. Kirillin, A. V. Kostanovskiĭ, and V. E. Fortov, Teplofiz. Vys. Temp. **36** (5), 740 (1998).

Translated by P. Pozdeev

Technical Physics Letters, Vol. 27, No. 9, 2001, pp. 740–742. Translated from Pis'ma v Zhurnal Tekhnicheskoĭ Fiziki, Vol. 27, No. 17, 2001, pp. 63–69.

Highly Efficient Polymeric Dye Laser Pumped at 1.06 μm

V. I. Bezrodnyi and A. A. Ishchenko

Institute of Physics, National Academy of Sciences of Ukraine, Kiev, Ukraine

e-mail: bezrod@iop.kiev.ua

Received March 11, 2001

Abstract—A tunable dye laser using a polyurethane-based active element pumped at 1.06 μm was obtained for the first time. The laser, employing polymethine dye 2696_y, has an energy conversion efficiency of 43% and can be tuned within a $\Delta\lambda = 63$ nm wavelength interval. © *2001 MAIK "Nauka/Interperiodica".*

Attractive properties of the dye lasers are a broad tunable spectral range and a high quantum efficiency. In comparison with the lasers of other types, these devices are significantly cheaper and their manufacturing technology is simpler. The dye lasers predominantly employ the active media of two types, liquid and solid. The latter possess several practical advantages over the former, as manifested by a higher thermal and optical characteristics. The solid-state lasers can be employed in a broader temperature interval; in particular, they can operate at low temperatures. These devices are usually energy-pumped with a second-harmonic radiation of a neodymium laser [1] and, less frequently, with the third-harmonic radiation of this laser or with the radiation of XeCl [2] or N_2 lasers [3]. However, these pumping sources provide for the effective dye laser generation only in the visible spectral range.

In the dye lasers with polymeric active media and laser pumping sources, there are principal difficulties in shifting the working frequency range toward the near IR (NIR) region. In order to solve these problems, it necessary either to create luminophors capable of providing a very large Stokes shift or to develop dyes strongly absorbing in the NIR range and admitting effective pumping via the second- or higher order electron transitions. The development of dyes producing Stokes shifts on the order of 500 nm and above in combination with high quantum efficiencies of the fluorescence is hardly probable [4], the more so that this shift would drop in a polymer matrix in comparison with dye solutions.

Pumping into high-order electron transitions offers poor prospects, primarily because such conditions lead to significant drop in the photostability of dyes. This is also frequently accompanied by a decrease in the conversion efficiency as a result of increasing the probability of nonradiative transitions, which is related to the participation of higher excited states. In addition, the emission of pumping sources operating in the UV range falls within the absorption range of many polymers, which would lead to degradation of the active elements and decrease the conversion efficiency. There are perfect pumping sources operating in the NIR range, such as neodymium lasers ($\lambda = 1.06$ μm), which can be used to obtain tunable NIR radiation in the 1.1–1.5 μm wavelength interval. However, this approach encounters difficulties with lasing even in the case of liquid active media solutions [5]. The stable and effective operation in the NIR range is hindered by the small fluorescence lifetimes and the low photochemical stability of the available dyes [4].

Below, we report for the first time on the obtaining of highly effective lasing in the NIR range using a tunable dye laser based on a new stained polymeric active medium. The polymer matrix was based on a polyurethane composition synthesized using the process of diol polycondensation with diisocyanate by the scheme

$$n\text{HO–R–OH} + n\text{OCN–R'–NCO}$$

$$\longrightarrow \text{–[–O–R–O–CO–NH–R'–NH–CO–]}_n\text{–},$$

where n is the number of molecules and R, R' are the aliphatic or aromatic hydrocarbon groups.

The proposed polymer composition was cured, by analogy with epoxy polymers, using a polycondensation reaction. However, in contrast to the epoxy polymers, this reaction proceeds under mild conditions (room temperature, neutral media). For this reason, dyes of any classes can be introduced into such a polymeric medium in the polymerization stage without risk of decomposition (neither complete nor partial). It must be noted that, using this polymeric medium as a matrix, we created a series of laser-resistant and stable passive laser gates for Q-modulated ruby [6] and neodymium lasers operating at a wavelength of 1.06 μm [7] or even in the region of 1.32–1.35 μm [8]. This polymer composition was also employed in the active media for dye lasers operating in the visible range [9], showing excellent results with respect to photostability and durability. The selected polyurethane matrix possesses rubberlike properties in a broad temperature interval, which allows the device to be operated at high pulsed loads without introducing special plasticizing additives. The polymeric active element was designed as a triplex system,

with the polymer matrix confined between two optical plates the outer surfaces of which can be coated with antireflection films. A high adhesion (≈100 kg/cm^2) of this polymer to glass substrates excludes the need in additional gluing compositions for the manufacture of laser elements.

The spectral transparency range (for $T \cong 100\%$) of a 1-cm-thick unstained polymer matrix measured with a Shimadzu UV-3100 spectrophotometer ranged from 0.32 to 2.2 μm. This transmission region indicates that the given polymer can be used in dye lasers pumped with the first harmonic of a neodymium laser. We have measured the radiation strength of the polyurethane based matrix at $\lambda = 1.064$ μm of a single-mode YAG laser operating in a single-pulse regime. The threshold for the single-pulse fracture of the polymer at a pulse duration of 20 ns and laser spot size of 100 μm was $E_d \geq 16$ J/cm^2.

The active elements for the lasers and the samples for spectral analyses were prepared by the methods described elsewhere [6–8]. The stained compositions were prepared using polymethine dye 2696$_y$, with a peak of the main absorption band in a polyurethane matrix observed at 1.079 μm. This dye possesses a high absorption cross section in this polymer (6.3×10^{-16} cm^2 at $\lambda = 1.064$ μm). Dye 2696$_y$ has a relatively large time (~50 ps) of the excited state relaxation in liquid systems [10]. The relaxation time for this dye measured in a polyurethane matrix using the method and experimental facility described in [11] was 100 ± 10 ps.

We have studied the spectral properties of a polyurethane-based composition containing dye 2696$_y$. The absorption contour of this compound is not distorted when molecules are embedded into the polymer matrix (Fig. 1, curve *1*), coinciding with the curves measured in the best liquid solvents. Therefore, no aggregation of the dye molecules that might be responsible for a change in the absorption contour takes place in the matrix employed for the working dye concentration interval from 10^{-5} to 0.5×10^{-3} mol/l. An investigation of the fluorescence spectrum was performed on a specially designed setup, in which the dye molecules in a 1-mm-thick sample with the initial transmittance $T_0 = 0.5$ at $\lambda = 1.064$ μm were excited by radiation of a neodymium YAG laser into a region of the $S_0 \longrightarrow S_1$ transition. The fluorescence signal was detected with a Ge photodetector sensitive in the 0.6- to 1.8-μm spectral range. The dispersive spectral instrument was an SPM-2 monochromator. The true fluorescence spectrum presented in Fig. 1 (curve *2*) was calculated with an allowance for the spectral sensitivity of the detector. As is seen from this spectrum, the fluorescence band of dye 2696$_y$ in polyurethane (as well as of other cationic tricarbocyanines in polar liquid solvents) is narrower as compared to the absorption band [12]. This is evidence [12] that the electrostatic interactions between the polar groups of the polymer and the distributed

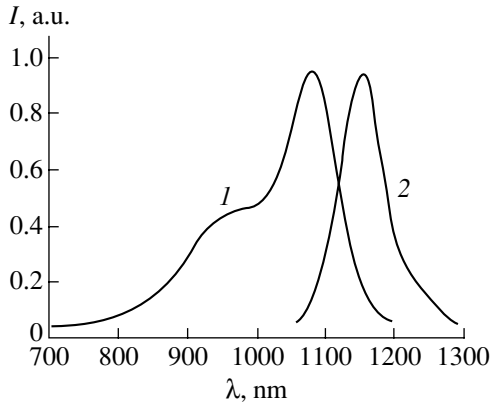

Fig. 1. Absorption (*1*) and fluorescence (*2*) spectra of dye 2696$_y$ in a polyurethane matrix.

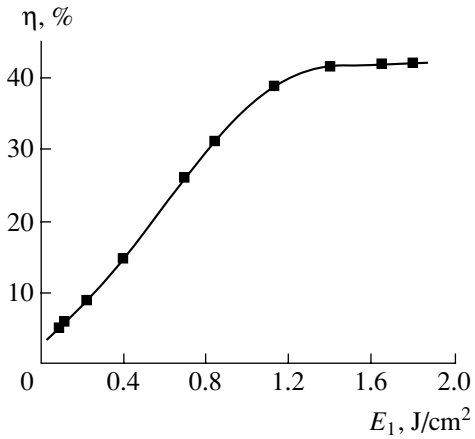

Fig. 2. The plot of conversion efficiency versus pumping energy for a dye laser with polymeric active element.

charge in the dye chromophore are weaker in the excited state than in the ground state [12]. As is seen from Fig. 1, the ratio of intensities of the absorption and fluorescence bands in the polyurethane matrix allows the system to be pumped using neodymium lasers ($\lambda = 1.06$ μm) to obtain effective lasing above 1.1 μm.

The generation characteristics were studied using active elements with a 2-mm-thick polymer layer possessing an optical density of $D = 5$ at the pumping wavelength. The lasing process was studied using two variants of the resonator: nondispersive (resonator 1) and dispersive (resonator 2). Resonator 1 comprised two 15-cm-spaced flat mirrors with the reflection coefficients 99.5 and 40% in the 1.1–1.2 μm spectral interval. The pumping in a quasi-longitudinal mode was effected with a YAG laser operated in a single-pulse regime ($\tau_i = 15$ ns) at a repetition rate of 1 Hz. The active element was mounted at the output mirror and adjusted at the Brewster angle relative to the lasing direction. The pumping radiation was focused in the active element with a long-focus lens ($F = 1$ m). The angle between the pumping and lasing beams was 12°.

Figure 2 shows a plot of the conversion efficiency $\eta = E_2/E_1$ versus the pumping energy E_1 excess over threshold. After the initial growth of η with the pumping intensity, the efficiency ceases to depend on E_1 and tends to a maximum level of $\eta_{max} = 43\%$ under the experimental conditions studied. When the polymeric active elements were replaced with a cell containing a standard solution of the same dye, we obtained a maximum conversion efficiency of 44%, which is approximately the same as the value attained with the polymer matrix. In this study, we did not aim at determining the optimum conditions favoring the maximum conversion efficiency, which depends primarily on the optical density at the pumping wavelength.

In order to determine the tuning wavelength interval of a laser employing the polymeric active element, we used a system with resonator 2. This device also is comprised of two flat mirrors with the reflection coefficients 99.5 and 40% in the 1.1–1.2 μm spectral interval. The dispersive elements were represented by two 60° prisms made of a K8 glass. In this case, the total resonator length was 16 cm. The tuning interval determined with the aid of an SPM-2 monochromator ranged from 1125 to 1188 nm, thus amounting to $\Delta\lambda = 63$ nm (at a maximum pumping intensity). It must be pointed out that the obtained conversion efficiency and tuning interval width are comparable with those of the best samples of polymeric active elements known in the visible spectral range, pumped at 532 nm. For example, investigations of the dye lasers employing a polyurethane-based matrix and Rhodamine 6G dye reported in [9] gave a conversion efficiency of 34% and a tuning interval width of 42 nm.

Thus, we have succeeded in obtaining an effective tunable generation in the range of >1100 nm using a dye laser with a polymeric active element pumped at 1.06 μm. These results indicate that such media are promising for the creation of tunable lasers operating both in the visible and in the near-IR range very important for practical applications.

REFERENCES

1. A. Costela, I. García-Moreno, J. Barroso, *et al.*, Appl. Phys. B: Laser Opt. **B70** (3), 367 (2000).
2. S. Wu and C. Zhu, Opt. Mater. **12** (1), 99 (1999).
3. A. Costela, I. García-Moreno, J. Barroso, *et al.*, Appl. Phys. B: Laser Opt. **B67** (2), 167 (1998).
4. A. A. Ishchenko, *Structure and Spectral-Luminescent Properties of Polymethine Dyes* (Naukova Dumka, Kiev, 1994).
5. A. Seilmeier, W. Kaiser, B. Sens, *et al.*, Opt. Lett. **8** (4), 205 (1983).
6. V. I. Bezrodnyi, N. A. Derevyanko, and A. A. Ishchenko, Kvantovaya Élektron. (Moscow) **23** (4), 353 (1996).
7. V. I. Bezrodnyi, L. V. Vovk, N. A. Derevyanko, *et al.*, Kvantovaya Élektron. (Moscow) **22** (3), 245 (1995).
8. V. I. Bezrodnyi, N. A. Derevyanko, A. A. Ishchenko, *et al.*, Kvantovaya Élektron. (Moscow) **22** (8), 853 (1995).
9. V. I. Bezrodnyi and A. A. Ishchenko, Kvantovaya Élektron. (Moscow) **30** (12), 1043 (2000).
10. A. A. Ishchenko, Kvantovaya Élektron. (Moscow) **21** (6), 513 (1994).
11. R. Grigonis, M. Eidenas, V. Bezrodnyi, *et al.*, in *Ultrafast Processes in Spectroscopy*, Ed. by O. Svelto (Plenum, New York, 1996), p. 101.
12. A. Ishchenko, V. Svidro, and N. Derevyanko, Dyes Pigm. **10** (2), 85 (1989).

Translated by P. Pozdeev

Technical Physics Letters, Vol. 27, No. 9, 2001, pp. 743–745. Translated from Pis'ma v Zhurnal Tekhnicheskoĭ Fiziki, Vol. 27, No. 17, 2001, pp. 70–75.

Switching Waves in Thick Bistable Interferometers at an Oblique Radiation Incidence

I. N. Dyuzhikov

Institute of Radio Engineering and Electronics, Russian Academy of Sciences, Moscow, Russia

Received March 15, 2001

Abstract—Special features of the switching wave propagation in thick ($L/\lambda \sim 100$) Fabry–Perot interferometers were studied by numerical modeling. It is shown that the effects related to a change in the phase adjustment of the interferometer are comparable with an angular correction to the switching wave velocity. *© 2001 MAIK "Nauka/Interperiodica".*

Waves switching wide-aperture bistable interferometers (BSIs) from one stable state to another were studied in sufficient detail both theoretically and experimentally (see the monograph [1] and references therein). In most cases, the radiation was normally incident onto a nonlinear BSI layer; the general case of oblique incidence was considered only for thin-layer BSIs in which variations of the phase adjustment can be ignored: $\delta \approx \dfrac{nL\gamma^2}{2\lambda} \ll 1$ (γ is the incidence angle, nL is the BSI optical thickness, and λ is the radiation wavelength) [2]. The experimental data reported for comparatively thick ($L/\lambda \sim 100$) BSIs of the Fabry–Perot type are poorly described by a thin-layer model and require the angular dependence of δ to be taken into account, since a change in the radiation incidence angle within 0–0.05 rad leads to the δ value variation by a factor of nearly 2π.

This study is devoted to the numerical modeling of the switching waves propagating in thick BSIs of the Fabry–Perot type in the case of oblique radiation incidence. The geometry of the problem is schematically depicted in Fig. 1a. A plane wave obliquely incident onto a nonlinear layer confined between mirrors $R1$ and $R2$ propagates in this layer at an angle γ relative to the normal. The absorption of light is accompanied by the photoproduction of charge carriers with a concentration N and a photorefraction of $n = n_0 + \sigma N$. The problem is assumed to be homogeneous in the direction perpendicular to the plane of the figure. The parameters of the nonlinear medium were taken equal to those of InSb at 77 K [3].

The switching wave front propagation is described by the equation of diffusion with a nonlinear source and a linear recombination terms:

$$\frac{\partial N}{\partial t} = D\frac{\partial^2 N}{\partial x^2} + G(I_0, x) - \frac{N}{\tau}, \qquad (1)$$

where N is the carrier concentration, τ is the carrier lifetime, and D is the carrier diffusion coefficient. The intensity of radiation inside the nonlinear layer is conveniently represented as a superposition of the two

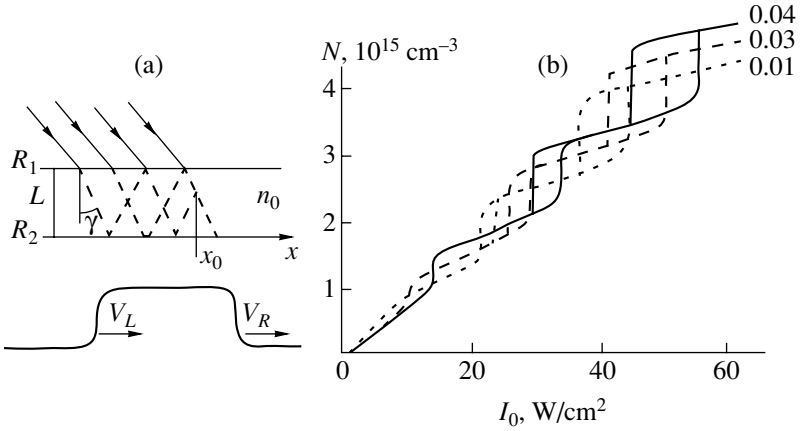

Fig. 1. Switching waves in a bistable Fabry–Perot interferometer: (a) geometry of the problem; (b) output characteristics for three angles of incidence.

1063-7850/01/2709-0743$21.00 © 2001 MAIK "Nauka/Interperiodica"

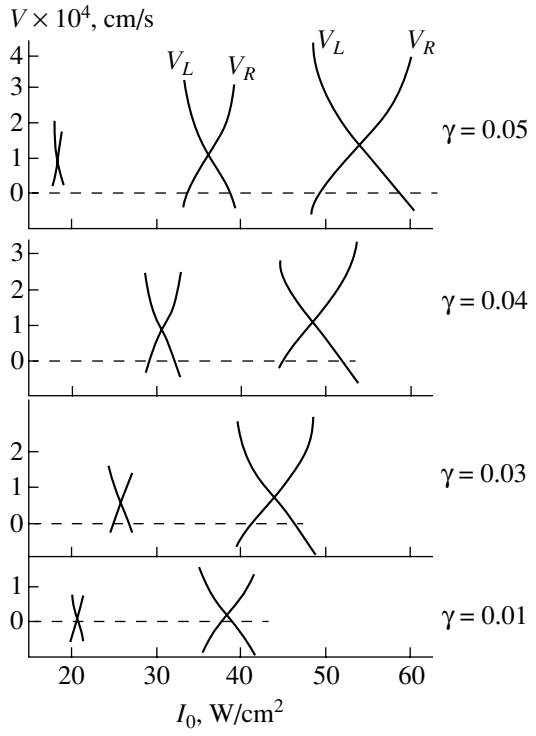

Fig. 2. The switching wave velocities in the lower orders of interference.

groups of waves propagating in the opposite directions. Taking into account that the waves in each group exhibit interference, the source can be described by the relationship

$$G(I_0, x) = (I_F + I_B)\frac{1 - \exp(-\alpha L)}{h\nu L}\eta, \qquad (2)$$

where $h\nu$ is the quantum energy, $\eta \approx 1$ is the internal quantum yield, and α is the absorption coefficient. A special feature of this problem is the nonlocal and unipolar character of the source, since the phase of the interfering rays carries information about the state of the region of medium extending from the entrance to x_0.

For the rays propagating in the forward direction, the expression describing the total intensity is

$$I_F = I_0(1 - R_1)\sum_0^m (R_1R_2\exp(-2\alpha L/\cos\gamma))^m \times \cos\left(\delta_m - 2mn_0\left(\frac{L}{\lambda}\right)\tan\gamma\sin\gamma\right), \qquad (3)$$

where $\delta_m = \frac{2Lm}{\cos\gamma}\int_{x_m}^{x_0} n\,dx$ is the phase increment ($x_m = x_0 - 2mL\tan\gamma$). The rays propagating in the back direction are described by an analogous expression. Taking into account that the intensity drops in geometric progression with increasing m, the sum in Eq. (3) was restricted to the rays with $I \geq (10^{-3}–10^{-4})I_0$. Equation (1) was approximated using an implicit scheme and the system of Eqs. (1)–(3) was solved by the Seidel iteration method.

At the normal incidence, the threshold intensity and the position of the bistable region with respect to intensity depend on the initial phase adjustment of the resonator. A similar pattern is observed for the oblique incidence, whereby a variation of the incidence angle leads to the corresponding change in δ. Another significant factor is the sign of the nonlinearity, since a negative nonlinear additive ($\Delta n < 0$) increases the threshold and expands the region of existence of the bistability; a positive additive produces the opposite effect.

Figure 1b shows the output characteristics of a BSI calculated for three angles of incidence at $\Delta n < 0$. The step of discretization with respect to intensity was selected equal to $\sim 10^{-3}$ of the maximum value. The exposure at each point was 4τ, which corresponds to a total sweep cycle duration of 1.6×10^{-4} s. This exposure is quite sufficient for monostable regions and the central parts of bistable regions; only in the regions featuring jumps from one to another branch would this selection result in a 10–15% loop broadening as compared to the stationary case. A characteristic difference of this case from the situation considered in [1] is that the low-order bistable region shifts toward high intensity with increasing γ and smoothly passes to the next order upon generation of a new hysteresis loop. Another distinction is a considerable expansion of the bistable region accompanying the shift toward higher intensities (Fig. 2). Here, an increase in the amplitude of V_R and V_L results in that the bistability is retained in the lower orders and at the angles exceeding the values predicted in [1–2].

An angular additive to the velocity qualitatively changes the dynamics of switching. Depending on the intensity, the transition from one to another branch may proceed in a traditional manner, whereby the waves propagate in the opposite directions and each bistable region contains 1 or 2 such domains at the edge. At the center of the bistable region, the switching waves move in the same direction and the system switches into a state characterized by a higher transition rate. In this case, an infinite BSI will exhibit drift and expansion of the second phase, whereby the left part (according to Fig. 1) remains in the initial state. For finite-size BSIs, this region is monostable if no special measures are taken (e.g., by coiling BSI into a ring). An illustrative example is offered by the interval 18 W/cm^2 < I_0 < 19 W/cm^2 in Fig. 2 ($\gamma = 0.05$). An exact model predicts bistability in this region, whereas an allowance for the spatial effects leads to monostable behavior.

This behavior of BSIs is directly related to splitting of the Maxwell switching wave intensity (at which the wave is immobile) into two components differing for the left and right switching waves. The magnitude of this splitting is a characteristic parameter of the angular

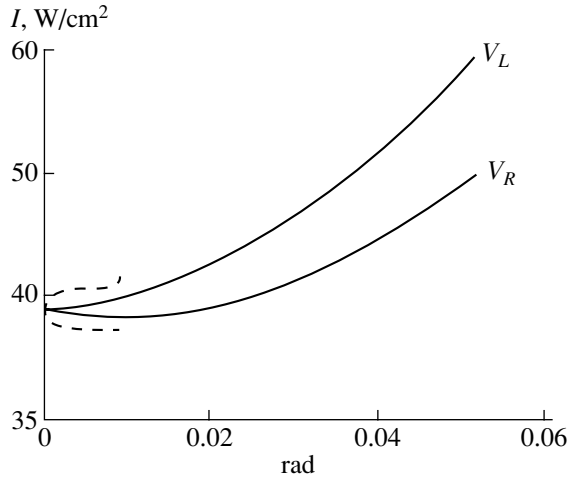

Fig. 3. Angular dependence of the Maxwell intensity of switching waves.

effect that directly influences the region of existence of the bistability. Figure 3 shows the angular dependence of the Maxwell switching wave intensity in the second order of interference. Here, the dashed curve qualitatively depicts the same relationships calculated with neglect of the phase shift [2]. As is seen, the phase additive for InSb with $L/\lambda \approx 10^2$ is close in order of magnitude to the angular splitting, so that the existence of bistability is determined by competition between the two effects.

It should be emphasized that the relationships illustrated in Figs. 2 and 3 refer to a radiation propagating at an angle of γ inside the interferometer. On the passage to an external angle, the corresponding angular scale should be increased by a factor of about four.

REFERENCES

1. N. N. Rozanov, *Optical Bistability and Hysteresis in Distributed Nonlinear Systems* (Nauka, Moscow, 1997).
2. N. N. Rozanov and A. V. Fedorov, Izv. Akad. Nauk SSSR, Ser. Fiz. **52** (3), 529 (1988).
3. A. V. Grigor'yants and I. N. Dyuzhikov, Fiz. Tverd. Tela (Leningrad) **32** (3), 909 (1990) [Sov. Phys. Solid State **32**, 537 (1990)].

Translated by P. Pozdeev

Technical Physics Letters, Vol. 27, No. 9, 2001, pp. 746–748. Translated from Pis'ma v Zhurnal Tekhnicheskoĭ Fiziki, Vol. 27, No. 17, 2001, pp. 76–81.

The Effect of Mechanical Activation on the Synthesis of Biocompatible $Ca_{10}(PO_4)_6(OH)_2$

N. A. Zakharov, Yu. P. Toporov, V. A. Klyuev, and V. P. Orlovskiĭ

Institute of General and Inorganic Chemistry, Russian Academy of Sciences, Moscow, 117907 Russia

Received February 27, 2001

Abstract—The effect of mechanical activation on the course of reactions involved in the synthesis of calcium hydroxyapatite $Ca_{10}(PO_4)_6(OH)_2$ was studied; the composition, crystallographic parameters, spectroscopic characteristics, and dielectric properties of the products were determined. The role of the composition of initial components on the rate of synthesis is analyzed. © *2001 MAIK "Nauka/Interperiodica".*

Calcium hydroxyapatite $Ca_{10}(PO_4)_6(OH)_2$ (CHA), which is close in composition to the inorganic components of teeth and bone tissues in animals and humans [1], finds increasing application in dentistry, orthopedics, and neurosurgery [2]. The growing use of CHA and related materials in medicine and some other fields [3] poses an important task of developing new methods of CHA synthesis and optimizing the existing technologies.

The arsenal of methods employed for the CHA synthesis is rather broad and can be classified into solution [4], solid-state [5], and hydrothermal [6] processes. However, all existing technological schemes possess serious disadvantages related either to a considerable duration of the process (caused by the limited solubility of reagents [4] or by the diffusion character of reactions [5]) or to the difficulties in monitoring the product purity and dispersity [6]. This circumstance stimulates the search for new competitive CHA synthesis technologies.

Good results in the synthesis of special-purpose materials were obtained by introducing the methods of physical (mechanical) activation into chemical processes [7, 8]. The action of mechanical factors upon solids initiates electron transitions, which is manifested by the phenomena of mechanoemission and conductivity buildup in crystals, as well as by the development of mechanochemical reactions [9, 10]. Below, we report on the implementation of mechanical activation into the known methods of CHA synthesis. We will analyze the influence of mechanical activation on the process features and on the physicochemical properties of the reaction products.

The process of mechanically activated CHA synthesis was conducted according to reactions 4a and 4b (see the table below) using initial components of the analytical purity grade. The stage of mechanical activation was implemented in a centrifugal activator of the ATO-2 type. The synthesized CHA samples were studied by methods of chemical analysis, X-ray diffraction (Ni-filtered CuK_α radiation), X-ray photoelectron spectroscopy (XPS), and IR absorption spectroscopy. The dielectric characteristics (ε and $\tan\delta$) were determined

The main characteristics of CHA synthesis by various methods and the properties of reaction products

No.	Method, initial components	Activation time	Annealing temperature, °C (time, h)	Unit cell parameters, Å		ε	$\tan\delta$	Refs.
				a	*c*	(at 20°C)		
1	Synthesis in aqueous solution		1000 (8 h)	9.432	6.881	8.8	0.04	[4]
2	Alkoxo method		500 (1 h)	9.415	6.885	8.9	0.05	[14]
3	Solid-state synthesis $6(NH_4)_2HPO_4 + CaCO_3$		1000 (18 h)	9.416	6.875			[12]
4	Synthesis with mechanical activation							
	(a) $6(NH_4)_2HPO_4 + 10CaCO_3$	30	500 (1 h)	9.417	6.878	9.1	0.09	
	(b) $6CaHPO_4 + 4CaO$	10	500 (1 h)	9.415	6.874	9.0	0.08	
5	ASTM data			9.418	6.884			ASTM card 9-432

1063-7850/01/2709-0746$21.00

on the samples of CHA-based ceramics (sintered at 1000°C) with silver paste electrodes (fused at 500°C).

The CHA synthesis with mechanical activation according to reactions 4a and 4b (see table) yields amorphous products exhibiting no X-ray diffraction reflections typical of fine-crystalline CHA. However, even a 1-h annealing at a relatively low temperature of 500°C leads to the formation of an intermediate product possessing a sufficient degree of crystallinity (see figure). Further increasing the annealing temperature (to 600–900°C) does not affect the character of the IR absorption spectra of CHA samples. According to Lerner *et al.* [11], the high degree of crystallinity of the synthesized CHA is shown by the good resolution of the IR absorption bands at 600 and 1100 cm^{-1}.

This result is achieved at the annealing temperatures that are significantly lower in comparison to those required in the case of samples synthesized in aqueous solutions [4] or in the solid state [12]. In contrast to the solid-state synthesis (see table) [12], the process with mechanical activation provides for the removal of undesired phases (such as β-$Ca_3(PO_4)_2$ and CaO hindering some applications) by annealing samples at lower temperatures and durations. In addition, a decrease in the annealing temperature eliminates the presence of defect calcium apatite $Ca_9(HPO_4)(PO_4)_5(OH)$ and oxoapatite $Ca_{10}(PO_4)_6O$ phases in annealed samples, the intense formation of which takes place at temperatures above 500°C [13].

Interpretation of the X-ray diffractograms of CHA samples synthesized in the mechanical activation regime according to reactions 4a and 4b (see table) followed by a thermal treatment above 500°C gave results coinciding with the indexes of samples prepared by the alkoxo process [14] and corresponding to those of the CHA standard (ASTM card 9-432). In the products of both mechanically activated reactions, the resolution of diffraction peaks characteristic of the CHA structure allows the substances to be identified as a single-phase CHA possessing a high degree of crystallinity. The unit cell parameters of both products ($P6_3/m$) point symmetry group satisfactorily agree with the ASTM data and with the structural characteristics of CHA obtained by other methods (see table).

According to the results of chemical analyses and XPS data for the standard CHA samples obtained from aqueous solutions, which are successfully used in implants, the Ca/P atomic ratio was 1.61. The product synthesized with mechanical activation according to reaction 4b (see table) was characterized by Ca/P = 1.5.

In the course of mechanical activation, the processed reagents interact with metal balls and walls of the activator. According to the XPS data, the content of Fe, Ti, and Cr impurities in CHA synthesized by reaction 4b was 8.16, 1.94, and 0.66 at.%, respectively. Deviation from the stoichiometry and the related decrease in the Ca/P ratio in the product obtained with mechanical activation (in contrast to CHA synthesized from an aqueous solution) is probably explained by a partial substitution of Fe, Ti, and Cr ions for Ca in the crystal lattice.

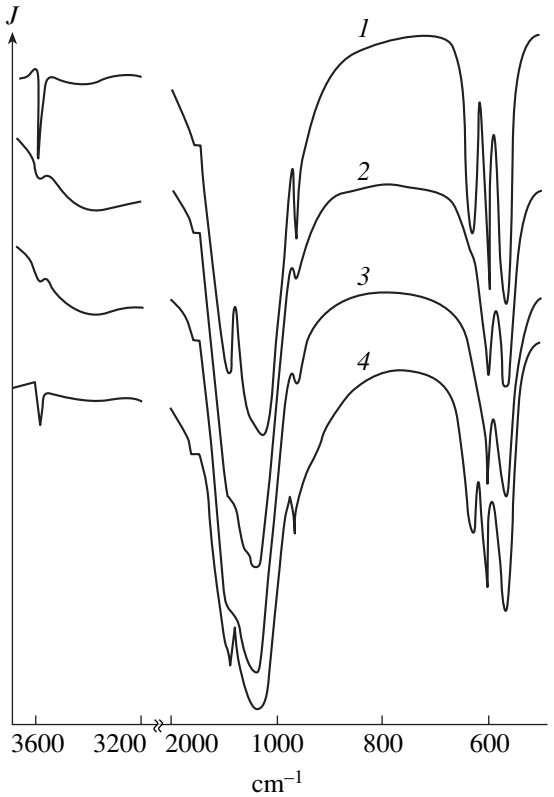

IR spectra of CHA synthesized by various methods: (*1*) in aqueous solution [4], (*2*) with mechanical activation by reaction 4a; (*3*, *4*) with mechanical activation by reaction 4b. The samples were measured (*1*–*3*) before and (*4*) after 1-h annealing at 500°C (*J* is the optical transmission).

The dielectric characteristics of CHA synthesized with mechanical activation were close to the analogous values for the samples obtained from an aqueous solution or by the alkoxo method (see table). Some increase in the $\tan\delta$ value of CHA synthesized with mechanical activation can be related to the presence of additional structural defects formed as a result of the nonisovalent calcium replacement.

It must be noted that the presence of Fe in CHA synthesized with mechanical activation, which imparts an ivory tint to the substance [15], is not fatal. In the dentistry, a important task is the search for implant materials having various tints (e.g., providing optimum cosmetic treatment for the enamel), since pure CHA is an ice-white substance. There is no doubt that the proposed method of colored CHA synthesis with mechanical activation is more effective in comparison to the solution process [15].

Thus, the obtained results allow us to conclude that the CHA synthesis can be significantly intensified by using a process with mechanical activation. The activation process leads to the formation of oxides in a

hydrated state, changes the reaction type toward hydrothermal, and favors an increase in reactivity of the protons produced in the course of the mechanical activation [7]. From this we may infer that the reaction rate of, for example, calcium hydroxide with calcium phosphates during the CHA formation increases in the series

$$CaHPO_4 < CaHPO_4 \cdot 2H_2O < Ca(H_2PO)_2 \cdot H_2O.$$

REFERENCES

1. L. L. Hench, J. Am. Ceram. Soc. **74** (7), 1487 (1991).
2. E. C. M. Driessens, *Bioceramics of Calcium Phosphate*, Ed. by K. de Groot (CRC Press, Boca Raton, 1983).
3. A. S. Vlasov and T. A. Karabanova, Steklo Keram., Nos. 9–10, 23 (1993).
4. V. P. Orlovskiĭ, Zh. A. Ezhova, and G. V. Rodicheva, Zh. Neorg. Khim. **37** (4), 881 (1992).
5. H. Monma, J. Ceram. Soc. Jpn. **28** (10), 97 (1980).
6. H. Yosimura, H. Suda, K. Okamoto, *et al.*, Nippon Kagaku Kaishi **21** (10), 1402 (1991).
7. E. G. Avvakumov, *Mechanical Methods of Chemical Process Activation* (Nauka, Novosibirsk, 1986).
8. G. Heinike, *Tribochemistry* (Akademie-Verlag, Berlin, 1984; Mir, Moscow, 1987).
9. B. V. Deryagin, N. A. Krotova, and Yu. A. Khrustalev, Vestn. Akad. Nauk SSSR, No. 6, 106 (1976).
10. Yu. A. Osip'yan and V. F. Petrenko, Dokl. Akad. Nauk SSSR **226** (4), 803 (1976) [Sov. Phys. Dokl. **21**, 87 (1976)].
11. E. Lerner, R. Azoury, and R. Sarig, J. Cryst. Growth **97**, 725 (1989).
12. P. A. Arsen'ev, A. A. Evdokimov, S. A. Smirnov, *et al.*, Zh. Neorg. Khim. **37** (12), 2649 (1992).
13. J. Zhan, X. Zhan, J. Chen, *et al.*, J. Mater. Sci.: Mater. Med. **4**, 83 (1993).
14. V. P. Orlovskiĭ, N. A. Zakharov, S. M. Speranskiĭ, *et al.*, Zh. Neorg. Khim. **42** (9), 1422 (1997).
15. R. Homung and A. Engler, J. Mater. Sci. Lett. **11**, 858 (1992).

Translated by P. Pozdeev

Technical Physics Letters, Vol. 27, No. 9, 2001, pp. 749–751. Translated from Pis'ma v Zhurnal Tekhnicheskoĭ Fiziki, Vol. 27, No. 17, 2001, pp. 82–87.

The Structure and Properties of a Hard Alloy Coating Deposited by High-Velocity Pulsed Plasma Jet onto a Copper Substrate

A. D. Pogrebnyak*, M. V. Il'yashenko*, V. S. Kshnyakin*, Yu. N. Tyurin, and Yu. F. Ivanov*****

** Institute of Surface Modification, Sumy, Ukraine*

*** Paton Institute of Electric Welding, National Academy of Sciences of Ukraine, Kiev, Ukraine*

**** Institute of High-Current Electronics, Siberian Division, Russian Academy of Sciences, Tomsk, Russia*

Received March 19, 2001

Abstract—Using a plasmatron operating in specially calculated regimes, tungsten carbide (WC) based coatings were deposited onto a copper crystallizer plate. It was found that a local hardness of the WC–Co coating may reach up to 1.3×10^4 N/mm^2 and the coating adhesion to substrate may be as high as 270 MPa. The elemental and phase compositions of coatings were studied by Rutherford backscattering spectroscopy, X-ray diffraction, and transmission electron microscopy with electron diffraction. The surface morphology and depth–composition profiles of the coatings were studied by optical and scanning electron microscopy. The coating is composed of WC crystal grains with hexagonal close packed (hcp) lattice, α- and β-Co grains, and cubic WC grains. The average size of the hcp WC grains is 0.15 μm and that of the cobalt particles is about 25 nm. In addition, the grain boundaries contain W_3Co_3C particles with an average size of 15 nm. © *2001 MAIK "Nauka/Interperiodica".*

Pulsed beams of charged particles and plasmas have been extensively used for the surface modification of various materials since the beginning of 1980s [1–4]. The action of such concentrated energy fluxes upon a solid sample leads to a high-rate (10^{-3}–10^{-8} s) heating of the surface layer followed by its rapid quenching with a fast heat removal in depth of the processed target. As a result, the target material exhibits significant structural and phase transformations, including the formation of metastable phases, dispersed nanoinclusions, amorphous layers, and high densities of dislocations and nonequilibrium point defects frequently accompanied by the ion-beam-induced mixing [1, 2]. Pulsed energy fluxes are also employed for depositing thin films, applying coatings, and obtaining dispersed nanoparticle powders [2]. In particular, by introducing a WC–Co powder (VK-12 grade) into a pulsed high-velocity plasma jet, one may obtain a coating of this composition with good adhesion to a copper crystallizer plate (solving this task is important for the molding technology).

The sample coatings were prepared using a pulsed plasmatron supplied with a VK-12 powder with an average particle size of 35–56 μm. Using preliminary mathematical modeling and variation of the plasmatron parameters, nozzle geometry, the distance from the nozzle to substrate surface, and the reaction chamber dimensions, we determined optimum values of the pulsed plasma jet velocity, plasma temperature, and optimum nozzle to substrate spacing. These parameters were as follows: jet plasma temperature, 2.4×10^4 K; jet velocity, ~7 km/s; jet power density, up to 10^7 W/cm^2; nozzle to substrate spacing, 30 mm. The gas mixture components and powdered material were supplied to the plasmatron in a continuous regime. The jet pulse duration was 0.3 ms.

Figure 1 shows the Rutherford backscattering (RBS) spectrum of He^+ ions for a tungsten carbide–cobalt coating. As is seen, the spectrum displays the

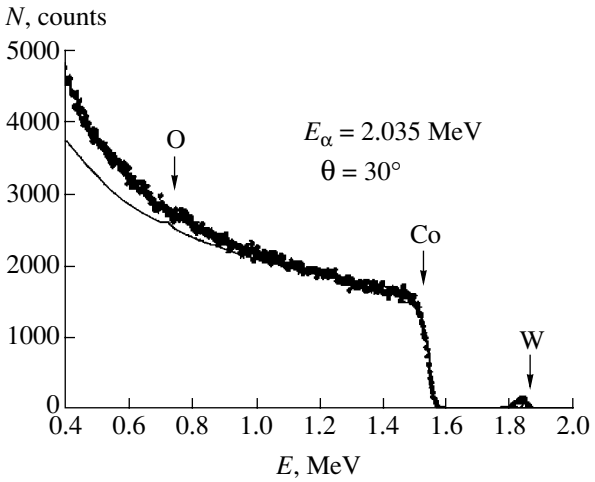

Fig. 1. RBS He^{4+} spectrum of a WC-Co coating on a copper crystallizer surface.

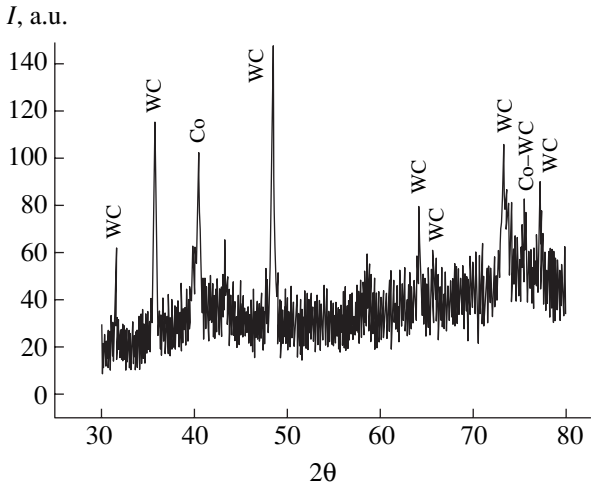

Fig. 2. X-ray diffractogram (CuK_α radiation; Sunya, Japan) of a WC–Co coating deposited by a pulsed plasma jet onto a copper crystallizer surface.

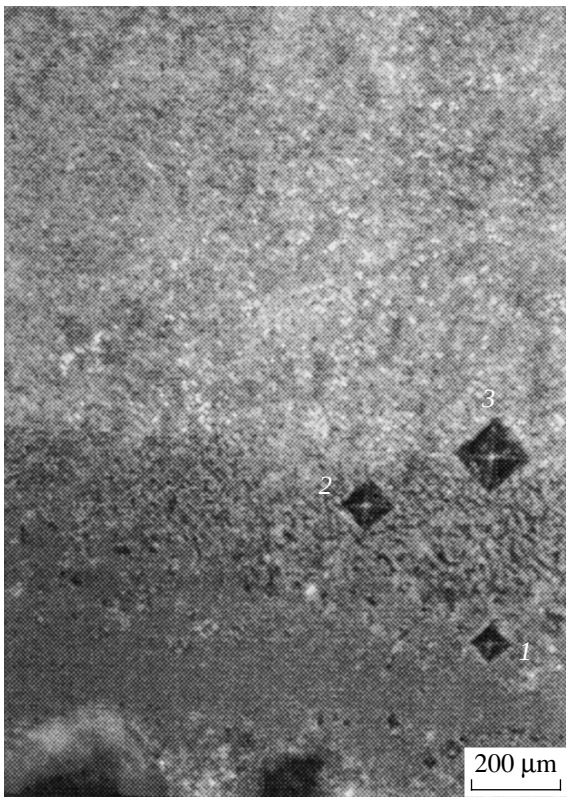

Fig. 3. Micrograph of the transverse cross section of a WC–Co coating on a copper substrate with indenter pyramid marks: (*1*) in the middle of the coating; (*2*) near the film-substrate interface; (*3*) at the film–substrate interface.

peaks of tungsten and oxygen and a kinematic threshold of Co. The relative content of Co, W, C, and O in the surface layer with a thickness of 2.8 μm corresponded to the following composition: WC_{89}; Co_8; C_2; O_2. Note that the concentration of tungsten on the film surface was very small (~1 at. %), while the carbon concentration reached 30 at. %. As is known [7, 8], the tungsten carbide films deposited by the HVOE and HEP techniques are characterized by the tungsten content increased up to 84.38 and 87.98%, respectively. This may even be accompanied by the partial amorphization of complex phases at the carbide and cobalt grains [8]. The cobalt content also changed to reach 12.98% (HVOE) and 9.22% (HEP), while the carbon concentration decreased from 4.09% in the initial powder to 2.5% (HVOE) and 2.52% (HEP). In our case, the coating contained phases which were mostly present in the initial powder, although some other phases formed in the course of rapid quenching appeared as well.

The X-ray diffraction analysis performed on a DRON-3 diffractometer using K_α–Cu radiation showed that the main phase in the coating was WC with an hcp lattice. The presence of other phases was evidenced by reflections in the 37°–47° angular interval (Fig. 2). Unfortunately, the diffraction peaks observed in this interval exhibited overlap, hindering the identification of phases. The interplanar spacings calculated for the reflections that could be resolved suggested the presence of the following phases: W_2C, Co_7W_6, Co_3W, W, and Co. Complex phases occurring in the intergranular regions may be amorphous, in agreement with [8, 9]. This state is explained by a high-temperature cycle involved in the coating formation.

Additional analysis of the sample structure and phase composition was performed with the aid of the transmission electron microscopy with electron diffraction. According to these data, the coating has a polycrystalline structure including grains of the hcp WC phase and the cubic α-Co, β-Co, and WC phases. The average size of the hcp WC grains is 0.15 μm and that of the cobalt particles is about 25 nm. In addition, the grain boundaries contain W_3Co_3C particles with an average size of 15 nm. A dislocation substructure was observed inside the cubic WC grains.

Figure 3 shows a micrograph of the transverse cross section of a WC–Co coating with prints of a diamond indenter pyramid used for the microhardness measurements (scale: 1 cm ~ 200 μm). As is seen from this image, the coating contains local regions possessing significantly different microhardnesses (ranging from 8×10^3 to 1.3×10^4 N/mm^2). The adhesion of coating to substrate was determined for the films deposited onto M-00 grade copper plates. This characteristic, determined after about ten measurements of the groove made by a diamond pyramid scribing the sample surface, was calculated by the formula $H_u = 4P/b^2$ (here P is the load and b is the groove width). The results of these measurements showed that the adhesion is on the average 250 MPa (ranging from 210 to 280 N/mm^2).

Acknowledgments. The authors are grateful to O.P. Kul'ment'eva for the fruitful discussion of results.

This study was partly in parts by the Tsukuba National Institute of Metal Research (Ibaraki, Japan) and Ukrainian Scientific-Technological Center (project no.1472).

REFERENCES

1. V. I. Boĭko, A. N. Valyaev, and A. D. Pogrebnyak, Usp. Fiz. Nauk **169** (11), 1243 (1999).
2. A. N. Valyaev, Kishimoto Naoki, and A. D. Pogrebnyak, *Modification of Materials Properties and Synthesis of Thin Films under Irradiation by Intense Electron and Ion Beams* (Vostochno-Kazakhstanskiĭ Tekhnicheskiĭ Univ., Ust'-Kamenogorsk, 2000).
3. V. L. Yakushev, B. A. Kalin, and V. I. Pol'skikh, Metally, No. 4, 74 (1994).
4. Yu. N. Tuyrin and A. D. Pogrebnjak, Surf. Coat. Technol. **111**, 269 (1999).
5. A. D. Pogrebnyak, Yu. N. Tyurin, Yu. F. Ivanov, *et al.*, Pis'ma Zh. Tekh. Fiz. **26** (21), 53 (2000) [Tech. Phys. Lett. **26**, 960 (2000)].
6. *Surface Modification and Alloying by Laser, Ion and Electron Beams*, Ed. by J. M. Poate, G. Foti, and D. C. Jacobson (Plenum, New York, 1983; Mashinostroenie, Moscow, 1987).
7. J. Nerz, B. Kushner, and A. Rotoliko, J. Therm. Spray Technol. **1** (2), 147 (1992).
8. C. J. Li, A. Ohmori, and J. Harada, J. Therm. Spray Technol. **5** (1), 69 (1996).
9. R. B. Bhagat, M. F. Amatean, A. Papyrin, *et al.*, ASM Thermal Spray Society, 1997, pp. 361–376.

Translated by P. Pozdeev

Technical Physics Letters, Vol. 27, No. 9, 2001, pp. 752–754. Translated from Pis'ma v Zhurnal Tekhnicheskoĭ Fiziki, Vol. 27, No. 17, 2001, pp. 88–94.

A Physical Mechanism of Dense Smoke Suppression in a Closed Room by Admitting a Charged Aqueous Aerosol

V. V. Salov, S. O. Shiryaeva, V. A. Salov, and A. S. Golovanov

Yaroslavl State University, Yaroslavl, Russia

e-mail: shir@uniyar.ac.ru

Received March 21, 2001

Abstract—It is experimentally demonstrated that the rapid suppression of an optically dense aerosol (smoke) by a strongly charged aqueous aerosol is related to acceleration of the volume diffusion and to electrostatic repulsion of the charged agglomerates. *© 2001 MAIK "Nauka/Interperiodica".*

Introduction. The phenomenon of suppression of an optically dense aerosol (dust, smoke, or mist) with a characteristic time of ~100 s upon introduction of a strongly charged (unipolar) liquid-droplet aerosol has been known for more than half a century [1]. However, the lack of an adequate theoretical interpretation of this phenomenon hinders its effective practical implementation, although experimental data are continuously being accumulated [2–5].

In the first step of theoretical rationalization of the phenomenon [1], a determining role was attributed (without any reasonable estimates) to the electrical coagulation of aerosols. However, this explanation disagrees with the experimentally observed small characteristic times of the aerosol suppression. Driven by electric induction forces rapidly decaying with distance, the electrostatic coagulation of dust, smoke, or mist droplets on coarse (~30 μm) charged water drops may lead to a significant decrease in the aerosol concentration only within a time period two to three orders of magnitude greater than that experimentally observed [2–5].

Previously [6, 7], theoretical notions about the physical laws governing the suppression of optically dense aerosols by strongly charged drops were developed based on a model of the Rayleigh decay of the latter aerosol, accompanied by the emission of hundreds of finely dispersed strongly charged droplets [8]. The latter particles possess a high mobility and coagulate at a high rate with the smoke of dust particles, which is followed by electrostatic repulsion of the resulting charged agglomerates. The idea proposed in [6, 7] provided a good agreement with experimental data, as demonstrated by a calculation performed for a model idealized optically dense aerosol.

However, it is still unclear what physical mechanism accounts for an increase in the optical characteristics of the aerosol. There are four possible variants: (i) coagulation of strongly charged water droplets with several particles of the initial aerosol, accompanied by electrostatic repulsion of these particles leading to an increase in their spacing; (ii) coagulation of water droplets with the aerosol particles leading to the formation of large agglomerates precipitating under the action of gravity; (iii) coagulation of water droplets with the aerosol particles leading to the formation of large agglomerates, followed by their repulsion manifested in the increasing spacing; (iv) a combination of the second and third mechanisms. Only direct experimental evidence may help elucidating a real mechanism involved in the optically dense aerosol suppression. This problem is considered below.

Experimental. The experiments were carried out in an aerosol chamber with a volume of 24 m^3. The smoke was produced in a flameless regime using a smoke generator operated at a temperature of ≈670 K. The amount of smoke was evaluated by measuring the optical density of the medium with the aid of a transmittance meter. The light source was an LGN-105 laser oriented along a diagonal of the experimental chamber. The photodetector was based on an FD-27K photodiode, and the photoinduced current $I(t)$ was measured and recorded in relative units with a PDP 4-002 recording potentiometer. In parallel, the smoke particle number density was estimated with the aid of an VDK-4 ultramicroscope. The volume concentration of smoke was determined by weighing substance trapped on an AFA-DP-3 absolute filter. The volume charge of the dispersed phase was measured with an VK-2-16 electrometer.

The smoking process was terminated upon reaching a preset value of the photocurrent. The medium was allowed to equilibrate and homogenize for 10 min. The initial parameters of the smoked medium were as follows: T = 298 K; relative humidity, E = 70%; particle number density, $n = 7 \times 10^6$ cm^{-3}; average particle diameter, $d \approx 0.3$ μm; volume smoke concentration, $C = 0.3$ g/m^3; visual range for a 100 × 100 cm white object, L = 0.3 m. The smoke with these characteristics

1063-7850/01/2709-0752$21.00 © 2001 MAIK "Nauka/Interperiodica"

exhibited spontaneous decay within a time period of ≈200 min.

Upon forming a homogeneous smoky aerosol, a charged aqueous aerosol was admitted to the chamber. The latter aerosol was produced by pneumatic spraying water with induction charging of the droplets [9]. The dispersing gas was compressed air at a pressure of $\approx 3 \times 10^6$ Pa, with the spray torch oriented along the large diagonal of the chamber. The water droplet radius r distribution in the spray torch was described by a function of the type [10]

$$dN \sim r^p \exp(-\beta r^q) dr,$$

where $p \approx 2$ and $q \approx 0.75$. The distribution maximum corresponded to $r \approx 2$ μm.

Results and discussion. The experiments showed that the most rapid decrease in the number density of aerosol particles was provided by acting upon the smoke with water droplets possessing an average diameter of $d_* \approx 5$ μm, carrying a charge q corresponding to the Rayleigh parameter $W \approx 0.2$ of the limiting value (unity); the quantity $W = q^2/2\pi\sigma d^3$ characterizes stability of a droplet with respect to the intrinsic uncompensated charge [8], σ being the surface tension of water. The aqueous aerosol was produced by spraying a total mass of $m = 40$ g of water during 90 s. After termination of the spraying, the resulting aerosol system exhibited a rapid decay within 40–50 s. As a result, the number density of smoke particles decreased by 93%, the visual range increased from 0.3 to 4.5 m, and the volume smoke concentration C was the same as that observed upon spontaneous decay. These data indicate that the action of the charged aerosol species upon the smoked medium has a volume character and the probable physical reason of the observed effect reduces to a rapid joint coagulation of the smoke and water aerosol particles.

The decay kinetics of the aerodispersed system was studied by monitoring the photocurrent measured with the transmittance meter (Fig. 1). The response current increases with decreasing particle number density n. In Fig. 1, curve *1* corresponds to the optimum smoke suppression regime ($d = 5$ μm, $m = 40$ g). As the amount of sprayed water increases, the monotonic variation of $I(t)$ breaks. Upon spraying $m = 65$ g of water, a short-time unstable mist is formed in the system. The $I(t)$ curve drops sharply before the end of spraying (curve *2*), which is indicative of worse conditions for light transmission through the combined aerodispersed system. After evaporation and decay of the mist, the current $I(t)$ begins to increase even at a higher rate than in the former case (curve *2* in Fig. 1), the growth continuing until complete decay of the resulting aerosol.

The results of our experiments showed that the brownian coagulation accompanying the natural evolution of a smoke with a particle number density of $\sim 10^6$ cm^{-3} in a closed volume of the experimental chamber does not lead (even over a few hours) to a significant increase in the radius of agglomerated smoke particles, which would be sufficient to switch on the gravity factor (precipitating coarse particles on the chamber bottom). This is evidenced by the curve of the photocurrent versus volume smoke concentration $I = I(C)$ experimentally measured during the natural aerosol decay in the absence of external factors. These data are depicted by open circles in Fig. 2, the first point corresponding to 5 min after the start of the process, the second point was measured in 20 min, the third and subsequent points were measured at a 40 min interval (the last, 7th point corresponds to a total time period of 200 min). The corresponding theoretical calculation by the Bouguer law is depicted by curve *1*. The Bouguer curve

$$F/F_0 = \exp(-\gamma l) \quad (1)$$

indicates the attenuation factor for a light beam that traveled a distance l in a medium with the extinction coefficient γ. For the considerations presented below, it is important to note that the extinction coefficient γ is proportional to the square linear size (cross section area) of the scattering center [11]. In addition, formula (1) yields an analogous relationship for the photocurrent intensity measured at the output of the aerosol chamber:

$$I/I_0 = \exp(-\gamma l). \quad (2)$$

Curves *1* and *2* in Fig. 2 were calculated using relationship (2).

The experimental points (denoted by crosses in Fig. 2) measured upon introducing (for ≈180 s) a charged aqueous aerosol (4 g per m^3) into the chamber fit to the theoretical curve *2*. This curve corresponds to

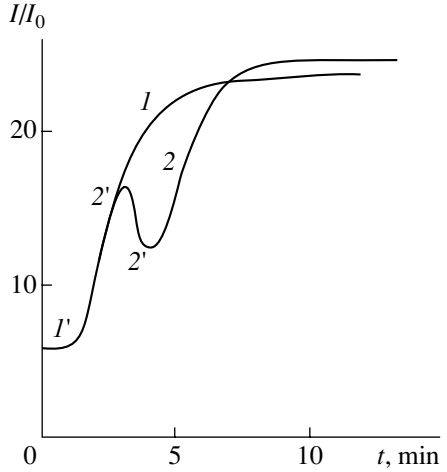

Fig. 1. The relative optical transmittance kinetics of an aerosol system upon introduction (within 90 s) of a highly dispersed strongly charged aqueous aerosol at a total amount of $m = 40$ g (*1*) and 90 g (*2*); points *1*' and *2*' indicate the start and end of spraying. Curve *2* shows a temporal decrease in the system transparency upon spraying, reflecting the mist formation.

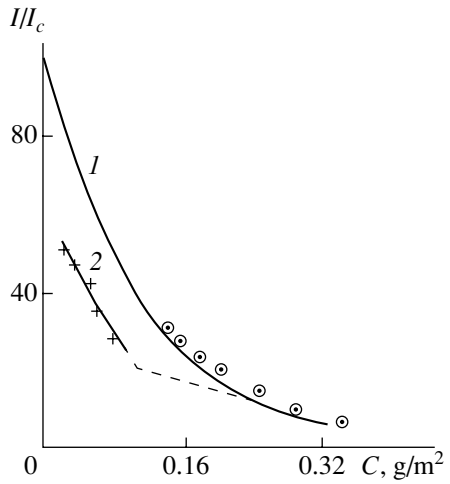

Fig. 2. Plots of the relative transmittance versus volume smoke concentration C for the aerosol system studied. Open circles represent experimental data for the smoke not treated with a charged aqueous aerosol (curve *1* depicts the corresponding Bouguer plot). Crosses present the experimental data for a smoke treated with a charged aqueous aerosol and curve *2* shows the corresponding Bouguer plot.

a four times greater extinction coefficient γ in the Bouguer law as compared to the value for curve *1*. This fact is indicative of the coarsening (doubling) of the characteristic linear size of the smoke particles in the stage of charging upon introduction of the charged aqueous aerosol (dashed line in Fig. 2). Upon termination of the aqueous aerosol spraying, no further coarsening of the smoke particles and changing of the γ value were observed, as indicated by the tight fit of the experimental points to the monotonic cure *2* corresponding to the Bouguer law with a large extinction coefficient. Note that the first experimental point in this series of experiments was obtained 15 min after aerosol admission and the subsequent points were measured at a 25 min time interval.

It should be emphasized that the experimental data depicted in Fig. 2 for the first time directly indicate a physical mechanism involved in the rapid suppression of an optically dense aerosol under the action of a strongly charged liquid-droplet aerosol. In the initial stage, the electrostatic polarization forces ensuring the attraction of neutral to charged particles lead to coarsening of the aerosol species; in the final stage, the mechanism of electrostatic repulsion between coarse charged (unipolar) particles is operative.

When a 100% relative humidity was developed in the aerosol chamber, the smoke particles absorbed water vapor until saturation and no effect of the accelerated decay of the smoke was observed upon introduction of the charged liquid-droplet aerosol.

Conclusion. The effect of rapid suppression of an optically dense aerodispersed system upon introduction of a strongly charged liquid-droplet aerosol is related to the accelerated coagulation of aerosol particles, followed by their coarsening and electrostatic repulsion of the charged agglomerates (in a closed room, this is accompanied by the loss of agglomerated smoke aerosol on the room walls).

REFERENCES

1. L. M. Levin, *Investigations on Physics of Coarsely Dispersed Aerosols* (Akad. Nauk SSSR, Moscow, 1961).
2. L. M. Makal'skiĭ, in *Application of Electron-Ion Technology in National Economy: Collection* (Mosk. Énerg. Inst., Moscow, 1991), pp. 202–215.
3. V. A. Salov, in *Proceedings of the 16th Conference of Commonwealth of Independent States on Problems of Evaporation, Burning, and Gas Dynamics of Disperse Systems, Odessa, 1993*, p. 42.
4. N. Kh. Kopyt, V. A. Salov, and S. I. Esipovich, in *Proceedings of the 18th Conference of Commonwealth of Independent States on Disperse Systems, Odessa, 1996*, p. 90.
5. V. A. Salov and V. V. Salov, in *Proceedings of the 19th Conference of Commonwealth of Independent States on Disperse Systems, Odessa, 2000*, p. 165.
6. A. I. Grigor'ev, V. A. Salov, Yu. V. Syshchikov, and S. O. Shiryaeva, Zh. Prikl. Khim. (Leningrad) **63** (7), 1524 (1990).
7. S. O. Shiryaeva, I. D. Grigor'eva, and V. A. Salov, Pis'ma Zh. Tekh. Fiz. **20** (5), 76 (1994) [Tech. Phys. Lett. **20**, 212 (1994)].
8. A. I. Grigor'ev and S. O. Shiryaeva, Zh. Tekh. Fiz. **61** (3), 19 (1991) [Sov. Phys. Tech. Phys. **36**, 258 (1991)].
9. Kh. F. Tammet, *Works on Electroionization and Electroaerosols* (Riga, 1963), vol. 140, p. 28.
10. D. G. Pazhi and V. S. Galustov, *Sprayers of Liquids* (Khimiya, Moscow, 1979).
11. P. Reist, *Introduction to Aerosol Science* (Mcmillan, New York, 1984; Mir, Moscow, 1987).

Translated by P. Pozdeev

Technical Physics Letters, Vol. 27, No. 9, 2001, pp. 755–757. Translated from Pis'ma v Zhurnal Tekhnicheskoĭ Fiziki, Vol. 27, No. 18, 2001, pp. 1–7.

The Effect of Photocurrent Amplification in an In_2O_3–GaSe Heterostructure

S. I. Drapak and Z. D. Kovalyuk

Institute for Problems in Materials Science, National Academy of Sciences of Ukraine, Chernovtsy, Ukraine

e-mail: chimsp@unicom.cv.ua

Received January 16, 2001

Abstract—The effect of photocurrent amplification in an In_2O_3–GaSe heterostructure with the barrier plane perpendicular to the base semiconductor layer was experimentally observed. At a reverse bias of $U = 10$ V, the gain reached $M \approx 82$ and the absolute current sensitivity amounted to 30–32 A/W. An analysis of the current–voltage characteristics allowed a mechanism of the charge transfer through dielectric to be determined that is always operative on the surface of gallium monoselenide in the heterostructures fabricated by spraying. It is suggested that the mechanism of conductivity can be modified by changing the barrier plane orientation from parallel to perpendicular to the GaSe layers. © *2001 MAIK "Nauka/Interperiodica".*

Some phenomena observed in In_2O_3–GaSe heterojunctions with introduced thin Ga_2O_3 interlayers were reported previously. For the first time, we present the results of investigation of a heterostructure exhibiting a considerable internal amplification of the photocurrent, in which a thin dielectric layer is represented by a natural Ga_2O_3 oxide possessing a conductivity close to the intrinsic value of the base semiconductor.

The sample structure was prepared by depositing a layer of the transparent conducting indium oxide In_2O_3 with strongly degenerate free electron gas ($n \cong 10^{20}$–10^{21} cm^{-3}) by spraying an ethanol solution of indium chloride at $T = 400$°C onto the surface of a *p*-GaSe single crystal ($p \cong 10^{16}$ cm^{-3}) parallel to the *C* axis (in bulk-grown GaSe, the samples with mirror cleavage surfaces of this orientation are encountered rather frequently). The barrier contact area was 8–10 mm^2. The ohmic contacts were prepared using a silver paste composition.

Figure 1 shows a qualitative energy band diagram of the sample heterostructure. The surface band bending φ_0 in GaSe was determined from the capacitance–voltage (*C–U*) characteristics [3] and the Fermi level position was calculated by the formula [4]

$$E_F - E_V = kT\ln(N_V/p),$$

where E_F and E_V are the energy positions of the Fermi level and the valence band top, respectively, in the base semiconductor; k is the Boltzmann constant; T is the absolute temperature; p is the equilibrium concentration of the majority carriers; and N_V is the effective concentration of states in the valence band determined from the slope of the *C–U* curve. The band structure parameters and the Fermi level position in In_2O_3 were taken from [5]. We also took into account the presence of a thin Ga_2O_3 layer unavoidably formed on the GaSe surface when the heterostructures are prepared as descried above. The oxide layer thickness determined with the aid of an LEM-2 laser ellipsometer amounted to 4–5 nm.

Since the sample heterostructures were sensitive to illumination in a wavelength range from 0.48 to 0.64 μm, it was expected that the main role in the photocurrent amplification is played by photoelectrons generated in the base semiconductor. It should also be noted that the presence of a natural oxide on GaSe is a negative factor decreasing the surface band bending [1] and, hence, reducing the gate layer thickness and the contribution of minority carriers to the total barrier current in reverse-biased heterostructures.

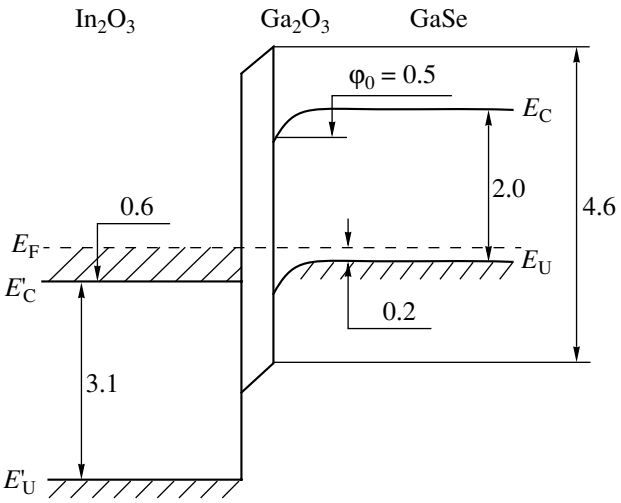

Fig. 1. An energy band diagram of the In_2O_3–GaSe heterostructure (all energy characteristics are in electronvolts).

1063-7850/01/2709-0755$21.00 © 2001 MAIK "Nauka/Interperiodica"

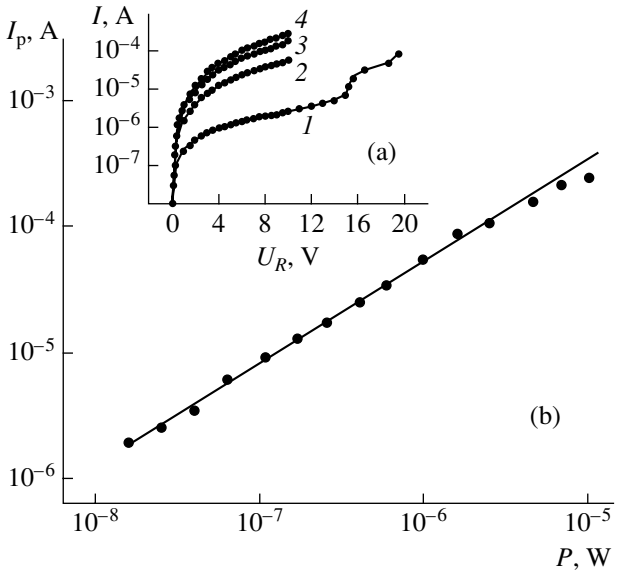

Fig. 2. Characteristics of the In_2O_3–GaSe heterostructure: (a) the reverse branches of the room-temperature *I–U* curves measured (*1*) in the dark and (*2–4*) under illumination at a power of 1.5, 7, and 15 mW, respectively; (b) the plot of photocurrent I_p versus illumination power *P*.

In order to determine the mechanism of the charge transfer through dielectric, we measured the current–voltage (*I–U*) curves in the forward and reverse directions. In the former case, a direct bias was created either by applying an external voltage (dark *I–U* measurements) or by generating charge carriers at large illumination levels (for excluding the *I–U* curve distortions related to nonlinear resistance of the semiconductor base region). In the latter case, the measurements were performed using a GaP light-emitting diode (LED) with λ_{max} = 560 nm. Measurement of the plot of photocurrent versus the open-circuit voltage U_{oc} (the latter reached 0.70–0.75 V for an illumination intensity of ≈100 mW/cm^2) is analogous to taking the forward branch of the *I–U* curve, the only difference being that the former curve reflects the electron processes occurring immediately in the barrier region of a real heterostructure [1]. Such measurements are especially important for studying the heterojunctions with a barrier plane parallel to the GaSe layers (i.e., perpendicularly to the *C* axis) [1, 2], in which case the serial resistance significantly affects the *I–V* curve shape. The results of measurements in both regimes were identical. The *I–V* curve measured in the forward direction at $U > 0.5$ V was described by a function of the type $\log I = f(U^{1/2})$ characteristic both of the Schottky emission and of the Poole–Frenkel thermoelectron ionization effect. However, the calculated slope values showed that the charge carrier transport through the dielectric in the forward direction is controlled by the Schottky emission [6]. In the *I–U* curve measured in the reverse direction, the initial portion was linear and then (at $|U| > 1$ V) the current increased exponentially with the voltage. This behavior is typical of the charge carrier tunneling under the barrier in the dielectric.

Figure 2a (curve *1*) shows the reverse branch of the dark *I–U* curve. The curve exhibits no clearly pronounced saturation usually observed for heterojunctions. In the region of large biases ($|U|$ = 12–16 V), the curve shows slightly pronounced *S*-character typical of the thermal breakdown. Measured under illumination (Fig. 2a, curves *2–4*), the reverse branches of the *I–U* curve are typical of the MTDS (metal–tunnel–dielectric–semiconductor) structures with internal photocurrent amplification [7]. The gain factor ($M \approx 82$) could be estimated from the plot of photocurrent I_p versus radiation power *P* (Fig. 2b). This output characteristic was measured using a heterostructure illuminated with the light of a yellow LED (wavelength, 0.56 μm; modulation frequency, 1 kHz; load resistance, 100 Ω; reverse bias, 10 V). As is seen from Fig. 2, the $I_p(P)$ curve is close to linear in a broad range of illumination intensities. The absolute value of the current sensitivity $R = I_p/P \approx 30$–32 A/W is significantly greater than the values characteristic of silicon photodiodes without internal photocurrent amplification. The sensitivity is comparable with that of an In_2O_3–a-Si:H–Si structure featuring a considerable photocurrent amplification at a reverse bias of U = 6 V [9].

It must be noted that, despite virtually identical behavior of both the *C–U* curves (the absence of the effect of surface states on the curve shape at both high and low frequencies; effect of the serial resistance on the cutoff voltage in the C^{-2} versus *U* curves used to determine the surface bend bending φ_0) and the *C–U* curves measured with a direct bias (the same slope in the semilogarithmic coordinates) observed for the heterostructures with the barrier plane parallel [1, 2] and perpendicular to the base semiconductor layers, the photocurrent amplification effect was observed only in the latter case.

The difference is apparently related to the anisotropic properties of gallium monoselenide. First, the current passage in the space-charge region in structures with the barrier plane parallel to the GaSe layers (perpendicular to the *C* axis) is described within the framework of a diffusion model. In our case, the anisotropic electrical properties of gallium monoselenide (the majority carrier mobility μ and the effective hole mass m_p^* along the layers are 6 and 4 times greater than the analogous values in the transverse direction, respectively [10]) are such that the criterion of applicability of the diffusion theory, $W \gg 2\varphi_0 l/kT$ [10] (where *W* is the gate layer thickness, φ_0 is the contact potential difference, and *l* is the mean free path of charge carriers), fails to be valid because both parts are virtually equal. From this we infer that a change in the barrier plane orientation from parallel to perpendicular to the GaSe layers probably leads to modification of the charge transfer

mechanism. Second, the carrier diffusion length in a structure with the barrier perpendicular to the GaSe layers is ten times greater than that in the structure with the same substrate thickness and the parallel barrier orientation only due to a difference in the minority carrier lifetimes determined from the kinetic characteristics ($\tau \sim 10^{-6}$ and 10^{-4} s for the barrier oriented parallel and perpendicular to the GaSe layers, respectively). Thus, in a heterostructure with the barrier oriented parallel to the base semiconductor layers, most of the charge carriers generated by light in the bulk of GaSe recombine. In the structures reported here, the probability that all the injected charge carriers will participate in the charge transfer through the barrier (perpendicular to the base GaSe layers) significantly increases.

These conclusions are confirmed by the results of measurements of the dark static characteristics of In_2O_3–GaSe–In_2O_3 and In_2O_3–GaSe–InSe transistor structures in a scheme with common base, the first In_2O_3–GaSe (perpendicularly oriented) junction operating as the collector and the second GaSe–In_2O_3 or GaSe–InSe junction (parallel to the base semiconductor layers) operating as the emitter. The general character of such characteristics is known to be analogous to the reverse branch of the *I–U* curve of a diode, because the collector junction is switched in the reverse direction and the electron injection from the emitter junction is somewhat analogous to the carrier photoproduction, the only difference being that the injected electrons have to travel over a certain distance in the emitter field (in our case, perpendicularly to the GaSe layers). In this case, the gain in the collector junction biased at $U = 10$ V in the reverse direction was $M \approx 1.14$–1.23 at an emitter current of 250 μA for the transistors of both types. This is evidence of a rather significant influence of recombination in the charge transfer across the GaSe layers. A further increase in the emitter–base voltage led to strong heating of the samples and degradation of the ohmic contacts.

Thus, the heterostructure studied can be used both as a polarization-sensitive transducer [11] and as a high-efficiency photodiode sensitive in the 0.48–0.64 μm spectral range.

Acknowledgments. The authors are grateful to V.A. Manasson, the Head of the Antenna Development Co. (Torrance, CA, USA), for his interest in this study and fruitful discussion of the results.

REFERENCES

1. V. N. Katerinchuk, Z. D. Kovalyuk, and V. A. Manasson, Fiz. Tekh. Poluprovodn. (Leningrad) **21** (11), 2094 (1987) [Sov. Phys. Semicond. **21**, 1270 (1987)].
2. S. L. Drapak, V. N. Katerinchuk, Z. D. Kovalyuk, and V. A. Manasson, Phys. Status Solidi A **115**, K35 (1989).
3. A. M. Goodman, J. Appl. Phys. **34** (2), 329 (1963).
4. V. L. Bonch-Bruevich and S. G. Kalashnikov, *Physics of Semiconductors* (Nauka, Moscow, 1965).
5. V. A. Manasson, A. I. Malik, and K. D. Tovstyuk, Fiz. Tekh. Poluprovodn. (Leningrad) **18** (12), 2121 (1984) [Sov. Phys. Semicond. **18**, 1323 (1984)].
6. P. T. Oreshkin, *Physics of Semiconductors and Dielectrics* (Vysshaya Shkola, Moscow, 1977).
7. A. Ya. Vul' and A. V. Sachenko, Fiz. Tekh. Poluprovodn. (Leningrad) **17** (8), 1361 (1983) [Sov. Phys. Semicond. **17**, 865 (1983)].
8. V. B. Baranyuk, G. P. Komissarov, V. A. Manasson, and É. M. Shuster, Fiz. Tekh. Poluprovodn. (Leningrad) **22** (4), 733 (1988) [Sov. Phys. Semicond. **22**, 456 (1988)].
9. S. I. Drapak, V. N. Katerinchuk, Z. D. Kovalyuk, and V. A. Manasson, Preprint No. 5, IPM (Kiev, 1989).
10. *Landolt-Bornstein. Numerical Data and Functional Relationships in Science and Technology, New Series*, Group III: *Crystal and Solid State Physics*, Ed. by O. Madelung (Springer-Verlag, Berlin, 1983), Vol. 17, sv. F.
11. V. A. Manasson, Z. D. Kovalyuk, S. I. Drapak, *et al.*, Electron. Lett. **26** (10), 664 (1990).

Translated by P. Pozdeev

Technical Physics Letters, Vol. 27, No. 9, 2001, pp. 758–760. Translated from Pis'ma v Zhurnal Tekhnicheskoĭ Fiziki, Vol. 27, No. 18, 2001, pp. 8–13.

The Light Reflection from Semiconductor Heterostructures Modulated by a Double Polarized Radiofrequency Field

A. O. Volkov, O. A. Ryabushkin, and M. S. Povolotskyi

Fryazino Branch, Institute of Radio Engineering and Electronics, Russian Academy of Sciences, Fryazino, Moscow oblast, Russia

e-mail: roa228@ire216.msk.su

Dipartamento di Ingegneria Elettronika, Università di Roma Tor Vergata, 00133 Roma, Italia

Received April 16, 2001

Abstract—An rf modulation optical spectroscopy method for the study of semiconductor heterostructures is suggested which employs the effect of the light reflection coefficient modulation under the action of two rf fields with different configurations. The dependence of the rf-modulated light reflection spectra at the fundamental absorption edge of a semiconductor on the rf field polarization allows various layers of the heterostructure to be selectively studied. A model is proposed that explains the features observed in the reflection spectra of the light modulated by longitudinal and transverse rf electric fields in a GaAs/AlGaAs heterostructure. © *2001 MAIK "Nauka/Interperiodica".*

Methods based on the modulated light reflection from semiconductors provide for a contactless determination of the energy features of the electron–hole interaction, the magnitude of a built-in electric field, the electron temperature gradient, etc. Such methods employ a periodic action (optical pumping, external electric field, current, etc.) upon a sample in order to modulate the dielectric permittivity of the material. Changes in the spectrum of light reflected from the sample, related to the reflected beam modulation, are studied using methods of lock-in detection. The modulated reflection spectra contain integral information about the sample layers within a depth on the order of the reciprocal absorption coefficient of either pumping or probing light (~10^{-6} m) [1]. In contrast to studying homogeneous semiconductors, the investigation of heterostructures encounters the problem of separating components of the modulated light reflection from various layers in the sample [2].

In the contactless electroreflectance technique used in [3], the optical reflection coefficient of a semiconductor was modulated by a homogeneous low-frequency electric field. The field was generated, and the sample was placed between plates of a flat capacitor. Our rf-modulated reflectance (RMR) method [4–7] employs the same electrode configuration, but the rf field can be more effectively introduced into a sample and is capable of providing information about fast processes in the sample structure. However, the possibilities of both methods are restricted by using a single mode of the electric field polarization. Application of the fields with different spatial orientations induces different mechanisms of charge transfer in the sample. Layers with different values of the conductivity tensor ($\sigma_{XX} \neq \sigma_{ZZ}$) would differently contribute to the modulated reflection spectrum, which can be used to separate the spectral components from various layers. Below, we report on the RMR spectra observed under the action of two rf fields with different configurations on a GaAs/AlGaAs heterostructure, which made it possible to reveal a superlattice layer in the sample.

The sample was placed in an air gap (with a width of $l \sim 5 \times 10^{-4}$ m) of a three-electrode capacitor between a quartz glass plate α and a flat metal electrode δ (Fig. 1). Two comb-shaped metal structures β and γ formed an interdigital capacitor with a spatial period $d \sim 2 \times 10^{-4}$ m. An rf voltage applied to the electrodes was modulated with respect to the amplitude $U = U_{\text{rf}}(1 + \cos\Omega t)\cos 2\pi\nu t$, where $U_{\text{rf}} \sim 1$–10^2 V, $\nu \sim 10^5$–10^7 Hz, and $\Omega/2\pi \sim 10^3$ Hz. Orientation of the electric fields ($\mathbf{F}^A$ or $\mathbf{F}^B$) was determined by switching electrodes in one of the two modes: in case A, the voltage was applied between the flat electrode and the shortened interdigital capacitor (transverse configuration); in case B, the voltage was applied between the two combs (longitudinal configuration). In case B, the flat electrode δ is isolated and weakly influences the rf field in the sample structure. In the transverse configuration, the two combs act as a common flat electrode, creating an electric field close to homogeneous with $U_{\text{rf}}/l \sim F_Z^A \gg F_X^A$. In the longitudinal configuration, a relationship between the electric field components is such that $2U_{\text{rf}}/d \sim F_X^B > F_Z^B$. A detailed calculation of the static electric field in this three-electrode capacitor was presented in [8]. A probing nonpolarized light beam of constant intensity in a limited spectral range with the

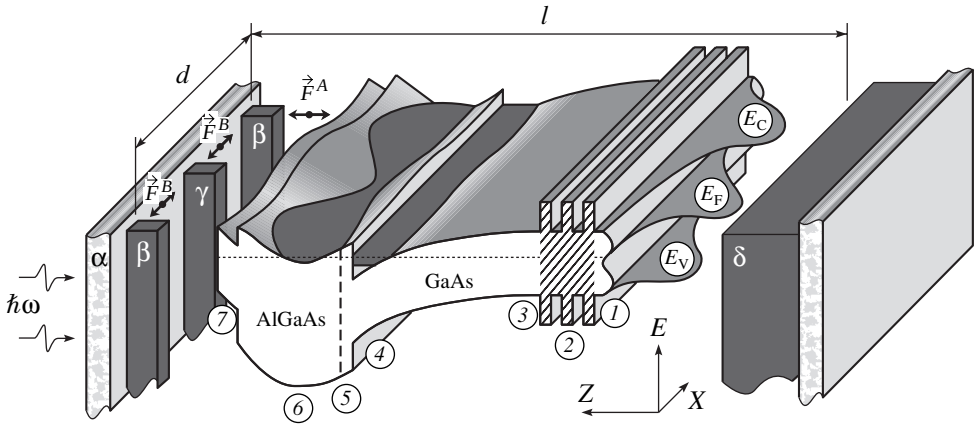

Fig. 1. Geometry and energy diagram of a sample heterostructure placed into the electric field of a three-electrode capacitor: *X* and *Z*, spatial coordinates; *E*, potential energy of electrons in the semiconductor structure; E_C, conduction band bottom; E_V, valence band top; E_F, Fermi energy; α, quartz glass plate; β, γ, interdigital capacitor electrodes; δ, flat electrode; $|\mathbf{F}^A|$ and $|\mathbf{F}^B|$, rf field amplitudes in the transverse and longitudinal configuration, respectively; cross-hatched layer *2* indicates superlattice; dark regions indicate the localization of free electrons in the presence of an external electric field.

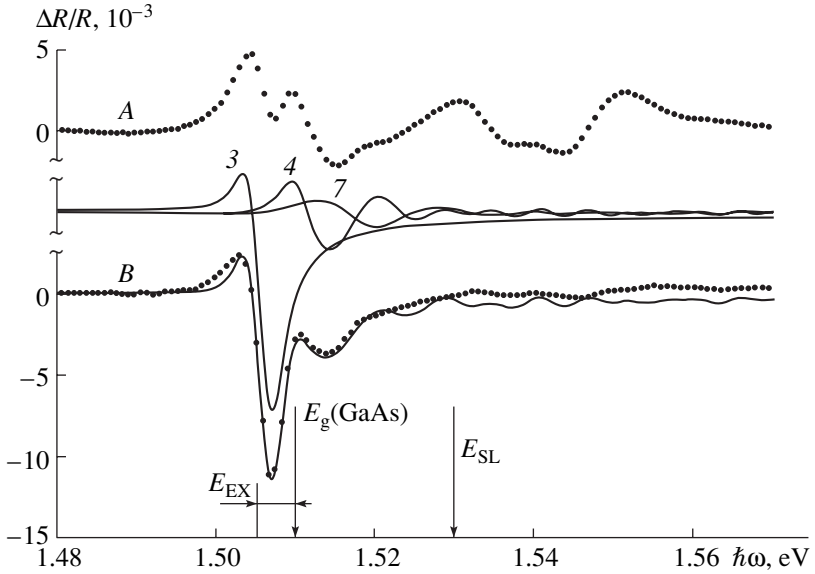

Fig. 2. Experimental (points) and model (solid curves) RMR spectra corresponding to (*A*) transverse and (*B*) longitudinal configurations of the rf field in the sample. Curves *3*, *4*, and *7* show contributions to the spectrum *B* due to layers *3*, *4*, and *7* in Fig. 1; E_g(GaAs) is the bandgap width in GaAs at 77 K; E_{EX} is the free exciton binding energy; E_{SL} is the energy of electron–hole transitions in the superlattice.

quantum energy close to the GaAs bandgap width, $\hbar\omega \sim E_g$(GaAs), was incident on the sample through the interdigital capacitor (with the stripe spacings $\sim 7 \times 10^{-5}$ m). Changes in the reflection spectrum of the probing light were detected by a lock-in scheme tuned to the modulation frequency Ω.

The experiments were performed with semiconductor heterostructures of the GaAs/$Al_xGa_{1-x}As$ type ($x \sim 0.15$) widely used for the fabrication of HEMT transistors. The sample heterostructure (Fig. 1) comprised a semi-insulating GaAs substrate *1*, a superlattice layer *2*, a buffer GaAs layer *3* containing a residual *p*-type impurity ($p \sim 10^{20}$ m^{-3}), a 100-Å-thick undoped AlGaAs layer *5*, a doped AlGaAs layer *6* ($n \sim 10^{24}$ m^{-3}), and a protective GaAs film *7*. The superlattice comprised 10 pairs of GaAs/AlGaAs (73 Å/23 Å) layers. Region *4* in Fig. 1 corresponds to a two-dimensional (2D) electron gas formed in the quantum well at the main heterojunction. The rf field energy is absorbed by free electrons in the regions *4* and *6*; the heating and redistribution of these electrons modulates the built-in electric field at the frequency Ω [4–7].

Figure 2 shows the RMR spectrum of the heterostructure measured at $T = 77$ K in the transverse rf field

configuration (curve *A*). The rather complicated shape of the spectrum is explained by the presence of contributions from various layers [4–7]. Measuring in the longitudinal rf field configuration decreases the number of contributing layers and, hence, yields a spectrum of simpler shape (curve *B*) that facilitates exact quantitative analysis.

Features in the RMR spectrum measured in the longitudinal rf field configuration, observed in the region of low probing quantum energies $\hbar\omega < E_g(\mathrm{GaAs})$, where $E_g(\mathrm{GaAs}) \sim 1.51$ eV at $T = 77$ K, are due to the rf field influencing the bound exciton states. The excitons are formed in the layers with a weak built-in electric field ($F < e/a_{\mathrm{EX}}^2 \sim 10^5$ V/m, where a_{EX} is the characteristic exciton size in GaAs). Such a weak field exists in the buffer layer *3* near superlattice *2*. In this region, the exciton binding energy E_{EX} is modulated by free electrons coming from the 2D electron gas *4* under the action of rf field [7]. Modulated reflection in the region of $\hbar\omega > E_g(\mathrm{GaAs})$ is determined by the Franz–Keldysh effect taking place in the regions featuring a strong built-in electric field. In the sample structure studied, such regions exist in the 2D electron gas *4* and in the protective layer *7*.

Figure 2 also presents the calculated modulation reflection spectra (curves *3*, *4*, and *7*). Spectrum *3* takes into account modulation of the exciton binding energy E_{EX} in a weak field of the buffer layer *3*, while spectra *4* and *7* allow for the electric field modulation in layers *4* and *7*, respectively. The RMR contribution from layer *3* was calculated within the framework of the Tanguy theory [9], which takes into account the ground and first excited exciton states. The contributions from layers *4* and *7* were calculated by conventional method [1] with an allowance for heavy and light holes. Interference of the optical responses from each partial layer was expressed in the total model spectrum constructed according to the Aspnes theory [1]. The best fit of the calculated spectrum to the experiment was obtained for the following parameters of layers in the heterostructure: exciton binding energy modulation, $E_{\mathrm{EX}} = (5.2–5.3) \times 10^{-3}$ eV; electric field strength modulation, $F_4 \sim (0.1–4) \times 10^5$ V/m; $F_7 \sim (3–7) \times 10^5$ V/m; phenomenological broadening parameter, $\Gamma_3 \sim 2.6 \times 10^{-3}$ eV; $\Gamma_4 \sim 1.2 \times 10^{-3}$ eV; $\Gamma_7 \sim 1.5 \times 10^{-3}$ eV.

The three-layer model describes the experimental RMR spectrum observed in the longitudinal rf field configuration sufficiently well. However, this model cannot adequately describe the spectrum measured in the transverse configuration (spectrum *A* in Fig. 2), which exhibits oscillations in the region of photon energies $\hbar\omega > 1.52$ eV. These oscillations are related to modulation of the exciton states in the quantum wells of superlattice *2*.

The difference between spectra *A* and *B* can be qualitatively explained if we take into account that a more homogeneous transverse field $\mathbf{F}^A$ acts upon all layers in the heterostructure. In contrast to this case, the longitudinal field $\mathbf{F}^B$ (Fig. 1) is screened by the layers of 2D electron gas *4* and doped AlGaAs *6* possessing a high conductivity in the *X*–*Y* plane. Since the field $\mathbf{F}^B$ relatively weakly penetrates into superlattice *2*, this layer does not contribute to the RMR spectrum. Thus, the rf-modulated reflectance measurements with different electric field configurations provides for a selective analysis of the layers of heterogeneous nanostructures with significantly anisotropic conductivity.

Acknowledgments. This study was supported by the Russian Foundation for Basic Research, project no. 00-02-16655.

REFERENCES

1. D. E. Aspnes, *Handbook on Semiconductors* (North-Holland, Amsterdam, 1980), Vol. 2.
2. M. Sydor, A. Badakhshan, J. R. Engholm, *et al.*, Appl. Phys. Lett. **58** (9), 948 (1991).
3. X. Yin and F. H. Pollak, Appl. Phys. Lett. **59** (18), 2305 (1991).
4. O. A. Ryabushkin and V. A. Sablikov, Pis'ma Zh. Éksp. Teor. Fiz. **67** (3), 217 (1998) [JETP Lett. **67**, 233 (1998)].
5. O. A. Ryabushkin and V. A. Sablikov, in *Proceedings of the SPIE XVI International Conference on Coherent and Nonlinear Optics, ICONO'98, 1998*, Proc. SPIE **3732**, 137 (1999).
6. O. A. Ryabushkin, V. A. Sablikov, M. S. Povolotskyi, *et al.*, Mikrosist. Tekh., No. 2, 20 (2001).
7. O. A. Ryabushkin, in *Proceedings of Conference "Nanostructures: Physics and Technology," St. Petersburg, 1997*, p. 270.
8. A. V. Efanov, Fiz. Tekh. Poluprovodn. (St. Petersburg) **30** (11), 2077 (1996) [Semiconductors **30**, 1083 (1996)].
9. Ch. Tanguy, J. Appl. Phys. **80**, 4626 (1996).

Translated by P. Pozdeev

Technical Physics Letters, Vol. 27, No. 9, 2001, pp. 761–764. Translated from Pis'ma v Zhurnal Tekhnicheskoĭ Fiziki, Vol. 27, No. 18, 2001, pp. 14–21.

The Cluster Charge and Size Distribution during Ion Sputtering of Metals

V. I. Matveev

Pomorskiĭ State University, Arkhangelsk, Russia

e-mail: matveev.victor@pomorsu.ru

Received March 6, 2001

Abstract—The process of elastic sputtering of a metal in the form of large neutral and charged clusters (with the number of atoms $N \geq 5$) during ion bombardment of the metal target was theoretically studied. The distribution is described by a simple analytical formula. © *2001 MAIK "Nauka/Interperiodica".*

Investigations into the ion sputtering of solids have been reported in a large number of publications (see, e.g., reviews [1–5] and references therein). Consistent model calculations and theoretical descriptions of these processes are highly complicated, first of all, by the essentially multiparticle character of the phenomenon both in the stage of ion penetration into a solid target and in the stage of formation of the sputtered products comprising single atoms of the target material and polyatomic particles (clusters) [6, 7]. The *ab initio* calculations using the molecular dynamics methods [1] (see also [8–10]) encounter considerable technical difficulties rapidly increasing with the number of atoms in the clusters; these calculations are usually hard to reproduce by researchers other than the authors of a given computational scheme. The difficulties additionally increase when processes related to the formation of charged particles are included into the molecular dynamics scheme [11].

Below, we present a theory of the process of metal sputtering in the form of large neutral and charged clusters (with the number of atoms $N \geq 5$) during ion bombardment of the metal target. The theory is based on simple physical assumptions and is consistent with experiment. The analysis, employing some previous results [12–15], yields a simple final simple expression for the probability of a cluster emission in a given charged state. The proposed approach is principally inapplicable to the case of sputtering of single atoms or small clusters. A comparison with experiment leads to a conclusion (see also [12–15]) that the model is applicable beginning with a certain number of atoms in sputtered clusters ($N \geq 5$).

Let us consider a solid composed of atoms, each atom oscillating in a well of depth Δ at an intrinsic frequency ω (the characteristic oscillation period is $T = 2\pi/\omega$). Let the impinging ions possess a velocity such that both the primary ion and fast recoil atoms moving in a metal target experience a large number of collisions during the time period $\tau \ll T$, as a result of which atoms of the metal target acquire the momenta $\mathbf{q}_i$, i being the atom number. Using the inequality $\tau \ll T$, we may alternatively formulate this description as follows. The projectile ion propagation through the system of oscillators reduces to instantaneously and simultaneously transferring the momenta $\mathbf{q}_i$ ($i = 1, 2, \ldots, N$) to the system of N oscillators. Below we will assume all quantities $\mathbf{q}_i$ ($i = 1, 2, \ldots, N$) to be independent and all directions equiprobable. The aim of this calculation is to determine the probability of finding the system of N oscillators (having instantaneously acquired moment $\mathbf{q}_i$) in the final bound states with the centers of mass moving with a momentum $\mathbf{k}$. The latter conditions implies that the entire system of N oscillators moves as a whole with the momentum $\mathbf{k}$.

The probability of such events, corresponding to the correlated breakage of an atomic block, is most readily calculated using the apparatus of quantum mechanics. Let us use the Einstein model and replace a block of N atoms by a system of N identical independent oscillators possessing the intrinsic frequency ω. The corresponding wavefunction is

$$\Psi_i = \Phi(\mathbf{R})\phi_1(\mathbf{r}_1)\phi_2(\mathbf{r}_2)\ldots\phi_N(\mathbf{r}_N), \qquad (1)$$

where $\Phi(\mathbf{R})$ is the wavefunction of the center of mass of the block of N atoms, $\mathbf{R}$ is the radius-vector representing coordinates of the center of mass, and $\phi_i(\mathbf{r}_i)$ is the wavefunction of the ith oscillator having the coordinates $\mathbf{r}_i$. The instantaneous and simultaneous transfer of momenta $\mathbf{q}_i$ converts the wavefunction (1) into

$$\exp\left(\frac{1}{\hbar}\sum_{i=1}^{N}\mathbf{q}_i\mathbf{R}\right)\Phi(\mathbf{R})\exp\left(\frac{i}{\hbar}\mathbf{q}_1\mathbf{r}_1\right)\phi_1(\mathbf{r}_1)$$
$$\times\exp\left(\frac{i}{\hbar}\mathbf{q}_2\mathbf{r}_2\right)\phi_2(\mathbf{r}_2)\times\ldots\times\exp\left(\frac{i}{\hbar}\mathbf{q}_N\mathbf{r}_N\right)\phi(\mathbf{r}_N). \qquad (2)$$

Let us assume that, before acquiring momenta $\mathbf{q}_i$, all oscillators occurred in the ground states, that is, $\phi_1 =$

$\phi_2 = \ldots = \phi_N \equiv \phi_0$, $\Phi \equiv \Phi_0$. The amplitude of the probability of finding an arbitrary final state $\Psi_f = \Phi_{\mathbf{k}}(\mathbf{R})\phi_{n1}(\mathbf{r}_1)\phi_{n2}(\mathbf{r}_2)\ldots\phi_{nN}(\mathbf{r}_N)$ with the center of mass in the state $\Phi_{\mathbf{k}}$ of a continuous spectrum with the momentum $\mathbf{k}$ is determined by the projection of the state Ψ_f onto states (2). Upon summation over the quantum numbers of oscillators n_i (under the condition $n = \sum_{i=1}^{N} n_i$, where n has the sense of the principal quantum number of the system of N oscillators), the square modulus of the probability amplitude is as follows:

$$W_{\mathbf{k}}^{(n)} = \frac{1}{n!}\left[\frac{1}{2\hbar^2\alpha^2}\sum_{i=1}^{N}\mathbf{q}_i^2\right]^n \exp\left\{-\frac{1}{2\hbar^2\alpha^2}\sum_{i=1}^{N}\mathbf{q}_i^2\right\} \times\left|\langle\Phi_{\mathbf{k}}(\mathbf{R})|\exp\left(\frac{i}{\hbar}\sum_{i=1}^{N}\mathbf{q}_i\mathbf{R}\right)|\Phi_0(\mathbf{R})\rangle\right|^2, \quad (3)$$

where $\alpha^2 = m\omega/\hbar$ and m is the mass of the oscillator (atom). In calculating the squared matrix element (3) and taking the sum, we employed the results of Fermi [16, article N 74] (see also [12– 15, 17]). Expression (3) is the probability that a cluster of N atoms is emitted as a whole with a momentum $\mathbf{k}$ in the excited sate n.

Being interested in the emission of stable clusters, we should take the sum of $W_{\mathbf{k}}^{(n)}$ over all excited states with n smaller than certain n_0 (for which the energy stored in the excited oscillators would suffice for breaking the cluster; we may take $n_0 \approx \Delta/\hbar\omega$ that corresponds to the case when the energy of all oscillators is sufficient to eject one atom from a well with the depth Δ). The total probability of finding the center of mass in a continuous spectrum can be determined by integrating over all $\mathbf{k}$. However, this value is more conveniently obtained by summing over all bound sates $\Phi_n(\mathbf{R})$ of the center of mass up to certain $n = k_0$ (determination of the k_0 value is described below), followed by subtracting the result from unity. Finally, we arrive at

$$W_N = \left[1 - \exp\left(-\frac{1}{k_0}\frac{1}{2\beta^2}\left(\sum_{i=1}^{N}\mathbf{q}_i\right)^2\right)\right] \times \exp\left(-\frac{1}{n_0}\frac{1}{2\hbar^2\alpha^2}\left(\sum_{i=1}^{N}\mathbf{q}_i\right)^2\right), \quad (4)$$

where $\beta^2 = mN\Omega/\hbar$ and Ω is the frequency of oscillations of the center of mass.

Now let us consider a procedure used for determining the quantity k_0. We assume that the center of mass of a block of N atoms performs harmonic oscillations at a frequency Ω in a potential well with the depth U_N, which will be referred to as the binding energy of the given cluster in the metal. This binding energy is proportional to the surface area S_N on which the block of N atoms contacts with the metal. Considering this surface as a hemisphere with a center situated on the unsputtered metal surface, we obtain $U_N = \sigma S_N = \delta N^{2/3}$ [12–15]. Thus, we must distinguish between δ, the fraction of the cluster binding energy (per atom in the cluster) and Δ, the potential well of each atom in the metal target. Apparently, k_0 entering into formula (4) can be evaluated as $U_N/(\hbar\Omega)$. Then we must average the probability (4) over all possible $\mathbf{q}_i$ ($i = 1, 2, \ldots, N$). A natural assumption concerning the distribution of $\mathbf{q}_i$ is that all these quantities are independent and all their directions are equiprobable. In averaging, as done in [12–15], the probability over directions $\Omega_{\mathbf{q}_i}$ of the vectors $\mathbf{q}_i$, we can significantly simplify the calculation by assuming all $|\mathbf{q}_i|$ to be equal and randomly oriented in space. As a result, the average probability for $N \gg 1$ takes the form

$$\overline{W_N} = \left[1 - \left(1 + N^{-\frac{2}{3}}\frac{q^2}{(k_{01})^2}\right)^{-\frac{3}{4}}\right]\exp\left(-N\frac{\delta}{\Delta}\frac{q^2}{(k_{01})^2}\right), \quad (5)$$

where $k_{01} = (2m\delta)^{1/2}$. Thus, we have determined the probability of detachment of the whole cluster (block) of N atoms without mutual substitutions of atoms.

The process of charged state formation is an important part of the sputtering mechanism. The following considerations are based essentially on the assumption that large clusters are emitted from the target as a whole, representing a block of atoms. Taking this circumstance into account, we will determine the charged state of a block of N atoms. For this purpose, by analogy with a statistical derivation of the Saha–Langmuir formula [18], we assume that there exist a certain (critical) distance ξ up to which exchange is possible between conduction electrons of the metal target and electrons of atoms in the cluster moving away from the target surface. When the cluster to metal distance exceeds ξ, the electron exchange nonadiabatically ceases. According to [15], the quantity $P_N(Q)$ representing the probability that a cluster of N atoms would possess a charge Qe (e being the electron charge) is determined using a standard formula for the probability of fluctuations

$$P_N(Q) = \frac{1}{D_N}\exp\left\{-\frac{1}{2}\frac{Q^2}{(\Delta Q_N)^2}\right\}, \qquad \overline{(\Delta Q_N)^2} = \frac{3^{\frac{1}{2}}}{\pi^{\frac{4}{3}}}\frac{m_e\vartheta}{\hbar^2}\left(\frac{V}{N}\right)^{\frac{2}{3}}\gamma^{\frac{1}{3}}N. \quad (6)$$

Here, D_N is the normalization factor determined by summation over all possible values of $Q = 0, \pm1, \pm2, \ldots$;

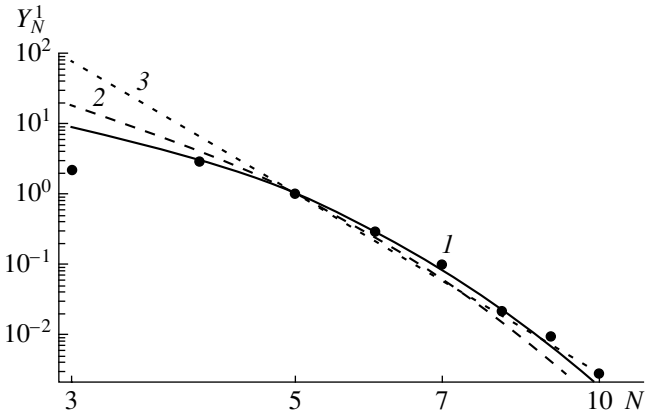

Fig. 1. Relative sputtering yield Y_N^1 of singly-charged tantalum clusters Ta_N^1 plotted versus the number N of atoms in the cluster, calculated for a tantalum target bombarded with singly charged 6-keV Au^{-1} ions at a target temperature of $\vartheta = 2273$ K. Solid curve presents the results of calculation for the parameter $q = 500$ at. units ($\hbar = m_e = e = 1$); points *1* represent the experimental data from [20, 21]. For the comparison, curve *2* shows the mass spectrum of neutral clusters Y_N^0 calculated ($q = 500$ at. units) for the same target temperature, curve *3* shows the power law [6] normalized to the fifth cluster (representing the $N^{-8.5}/5^{-8.5}$ function).

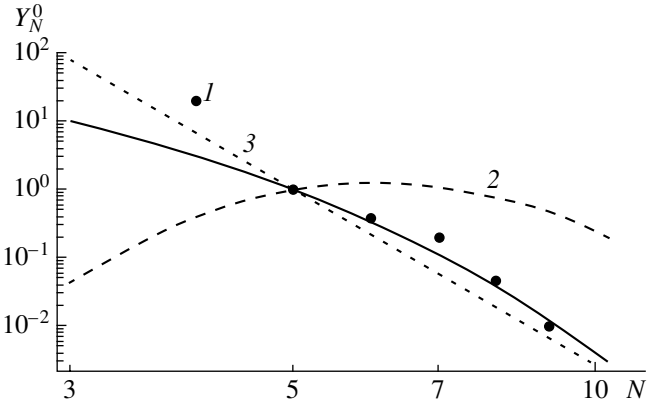

Fig. 2. Relative sputtering yield Y_N^0 of neutral tantalum clusters Ta_N^0 plotted versus the number N of atoms in the cluster, calculated for a tantalum target bombarded with singly charged 5-keV Ar^{+1} ions at a target temperature of $\vartheta = 300$ K. Solid curve presents the results of calculation for the parameter $q = 450$ at. units ($\hbar = m_e = e = 1$); points *1* represent the experimental data from [6]. For the comparison, curve *2* shows the mass spectrum of singly-charged clusters Y_N^1 calculated ($q = 450$ at. units) for the same target temperature, curve *3* shows the power law [6] normalized to the fifth cluster (representing the $N^{-8.5}/5^{-8.5}$ function).

$\overline{(\Delta Q_N)^2}$ is the mean square deviation of the cluster charge from the equilibrium value; m_e is the mass of the conduction electron; V is the cluster volume; ϑ is the target temperature; and γ is the valence of metal atoms.

Finally, to determine the probability W_N^Q of finding a cluster of N atoms carrying the charge Qe, we must multiply the probability W_N given by Eq. (5) by $P_N(Q)$. As a result, we obtain the final expression for the probability of emission of a cluster of N atoms with the charge Qe:

$$W_N^Q = \left[1 - \left(1 + N^{-\frac{2}{3}}\frac{q^2}{(k_{01})^2}\right)^{-\frac{3}{2}}\right] \times \exp\left(-N\frac{\delta}{\Delta}\frac{q^2}{(k_{01})^2}\right)\frac{1}{D_N}\exp\left\{-\frac{1}{2}\frac{Q^2}{(\Delta Q_N)^2}\right\}. \quad (7)$$

In experiment, we usually determine the relative probabilities of the emission of clusters with various numbers of atoms. For the comparison with such experimental data, the probability (7) first has to be divided by the probability of emission of a cluster with $N = 5$ (any number $N \geq 5$ can be selected, but $N = 5$ is more convenient for our purposes); experimental data have to be normalized accordingly. Then, if necessary, it is possible to pass to any other convenient units.

Figures 1 and 2 show the relative sputtering yields $Y_N^Q = W_N^Q/W_5^Q$ of singly charged (Y_N^1) and neutral (Y_N^0) tantalum clusters Ta_N plotted versus the number N of atoms in the cluster, calculated for a tantalum target bombarded with singly charged 6-keV Au^{-1} ions or 5-keV Ar^{+1} ions at a target temperature of $\vartheta = 2273$ or 300 K, respectively. For the comparison, we also plotted the power law [6] normalized to the fifth cluster (representing the $N^{-8.5}/5^{-8.5}$ function for tantalum). In order to restrict the number of fitting parameters in the calculation, we assumed that $\Delta = \delta = 8.1$ eV (the sublimation energy of Ta [19]). It must be noted that the mass spectra of neutral clusters weakly depend on the target temperature. The spectra of singly charged clusters are significantly affected by the temperature but, as the temperature increases, the latter spectra approach the spectra of neutral clusters.

Acknowledgments. The author gratefully acknowledges financial support of the Ministry of Education of the Russian Federation within the framework of the Program of Fundamental Research in Natural Sciences.

REFERENCES

1. *Fundamental and Applied Aspects of Solid Sputtering: Collection of Articles*, Comp. by E. S. Mashkov (Mir, Moscow, 1989).
2. N. N. Andersen, K. Dan. Vidensk. Selsk. Mat. Fys. Medd. **43**, 127 (1993).
3. H. M. Urbassek and W. O. Hofer, K. Dan. Vidensk. Selsk. Mat. Fys. Medd. **43**, 97 (1993).

4. I. A. Baranov, Yu. V. Martynenko, S. O. Tsepelevich, and Yu. N. Yavlinskiĭ, Usp. Fiz. Nauk **156**, 478 (1988) [Sov. Phys. Usp. **31**, 1015 (1988)].
5. *Sputtering by Particle Bombardment*, Ed. by R. Behrisch and K. Wittmaack (Springer-Verlag, New York, 1991; Mir, Moscow, 1998), Vol. III.
6. A. Wucher and W. Wahl, Nucl. Instrum. Methods Phys. Res. B **115**, 581 (1996).
7. S. R. Coon, W. F. Calaway, and M. Y. Pellin, Nucl. Instrum. Methods Phys. Res. B **90**, 518 (1994).
8. A. Wucher and B. Y. Garrison, J. Chem. Phys. **105**, 5999 (1996).
9. A. Brunelle, S. Della-Negra, C. Deprun, *et al.*, Int. J. Mass Spectrom. Ion Processes **164**, 193 (1997).
10. Th. J. Colla, H. M. Urbassek, A. Wucher, *et al.*, Nucl. Instrum. Methods Phys. Res. B **143**, 284 (1998).
11. M. L. Yu, in *Sputtering by Particle Bombardment*, Ed. by R. Behrisch and K. Wittmaack (Springer-Verlag, New York, 1991; Mir, Moscow, 1998), Vol. III, p. 91.
12. V. I. Matveev and P. K. Khabibullaev, Dokl. Akad. Nauk **362** (2), 191 (1998) [Dokl. Phys. **43**, 544 (1998)].
13. V. I. Matveev, S. F. Belykh, and I. V. Verevkin, Zh. Tekh. Fiz. **69** (3), 64 (1999) [Tech. Phys. **44**, 323 (1999)].
14. S. F. Belykh, V. I. Matveev, I. V. Veryovkin, *et al.*, Nucl. Instrum. Methods Phys. Res. B **155** (4), 409 (1999).
15. V. I. Matveev, Zh. Tekh. Fiz. **70** (8), 108 (2000) [Tech. Phys. **45**, 1063 (2000)].
16. É. Fermi, *Scientific Works* (Nauka, Moscow, 1971), Vol. 1.
17. L. D. Landau and E. M. Lifshitz, *Course of Theoretical Physics*, Vol. 3: *Quantum Mechanics: Non-Relativistic Theory* (Nauka, Moscow, 1989, 4th ed.; Pergamon, New York, 1977, 3rd ed.).
18. L. N. Dobretsov and M. V. Gomoyunova, *Emission Electronics* (Nauka, Moscow, 1966).
19. C. Kittel, *Introduction to Solid State Physics* (Wiley, New York, 1976; Nauka, Moscow, 1978).
20. S. F. Belykh, U. Kh. Rasulev, A. V. Samartsev, and I. V. Veryovkin, Nucl. Instrum. Methods Phys. Res. B **136**, 773 (1998).
21. S. F. Belykh, U. Kh. Rasulev, A. V. Samartsev, *et al.*, Mikrochim. Acta, Suppl. **15**, 379 (1998).

Translated by P. Pozdeev

Technical Physics Letters, Vol. 27, No. 9, 2001, pp. 765–768. Translated from Pis'ma v Zhurnal Tekhnicheskoĭ Fiziki, Vol. 27, No. 18, 2001, pp. 22–28.

The Effect of Decreased Mass Transfer in Twisted Flows

V. L. Okulov[a]* and S. A. Martemianov[b]**

[a] *Institute of Thermal Physics, Siberian Division, Russian Academy of Sciences, Novosibirsk, Russia*

** e-mail: okulov@itp.nsc.ru*

[b] *Laboratoire d'Etudes Thermiques UMR CNRS n. 6608, ESIP, 40, Avenue du Recteur Pineau, 68022 Poitiers Cedewx, France*

*** e-mail: martemianov@esip.univ-poitiers.fr*

Received March 20, 2001

Abstract—A model describing mass transfer from a swirling flow toward walls of a cylindrical reactor is developed for the first time. The model explains a possible decrease in the mass transfer caused by the flow swirling.

Intensification of the mass exchange processes in hydrodynamic flows is an important task in many technical applications. It was commonly accepted that the flow swirling in a reactor always leads to an increase in the mass transfer at the expense of a natural increase in the trajectory length and in the time for which particles stay in the reactor. However, some experimental results obtained in the past decade [1–3] revealed some swirling flow regimes characterized by the mass transfer from flow to wall reduced as compared to that in a translatory (nonswirling) flow (for the same electrolyte supply rate to the reactor).

In order to explain this phenomenon, let us consider the problem of mass transfer in a swirling flow in a mass exchange reactor section representing a cylinder with the radius R and the length L. To simplify mathematical formulation of the problem, we will restrict the consideration to steady-state axisymmetric regimes (with neglect of turbulent pulsations and three-dimensional effects). Let the mass exchange reactor section be sufficiently short, so that the boundary layer developed along this section has a small curvature as compared to the cylinder radius and, hence, does not significantly affect the nonviscous flow in the core. We will also assume that the mass transfer does not influence the flow hydrodynamics (the Schmidt number Sc is treated as a constant and dependence on this parameter is not considered; the Sc value is assumed to be sufficiently large, so that a diffusion layer is deep inside the boundary layer). The concentration of a substance entering into reaction on the wall surface is constant (different from a concentration in the flow core).

The mass exchange between the reactor wall and the swirling flow will be calculated for a flow induced by an axisymmetric vortex structure. This structure determines a nonviscous flow core formed in the cylindrical mass exchange reactor section. Let the vortex axis coincide with the cylinder axis and let the vortex core with a radius ε ($\varepsilon < R$) consist of screw current lines with a constant pitch of $2\pi l$ and a constant axial vorticity component corresponding to a simple flow velocity field [4]:

$$w_\varphi = \frac{\Gamma}{r}\begin{cases} r^2/\varepsilon^2, & r < \varepsilon \\ 1, & r \geq \varepsilon \end{cases};$$
$$w_z = w_0 - \frac{\Gamma}{l}\begin{cases} r^2/\varepsilon^2, & r < \varepsilon \\ 1, & r \geq \varepsilon \end{cases}, \quad (1)$$

where Γ is the vortex circulation, w_0 is the velocity at the flow axis, and w_z and w_φ are the axial and tangential velocity components of the nonviscous flow (Fig. 1). The selected solution (1) of the Euler equations adequately describes the experimental velocity profiles in various swirling flows [4–6] and allows the main mass transfer characteristics (the coefficient k of mass transfer to the surface of the cylindrical tube and the Sherwood number Sh) to be calculated without recourse to any empirical hypotheses.

The presence of the second velocity component (related to the flow swirling) in Eqs. (1) leads to the necessity of considering equations for a three-dimensional (3D) boundary layer (see [7, p. 249]) with the following boundary conditions:

$$y = 0: u = v = w = 0;$$
$$y = \infty: u = w_\varphi(R) \equiv V; w = w\zeta(R) \equiv W,$$

where u, v, w are the velocity components in the boundary layer; the x axis coincides with the tangential direction; $y = R - r$ is the distance to wall in the radial direction; and the z axis is oriented along the cylinder axis (Fig. 1). By virtue of the assumption concerning a con-

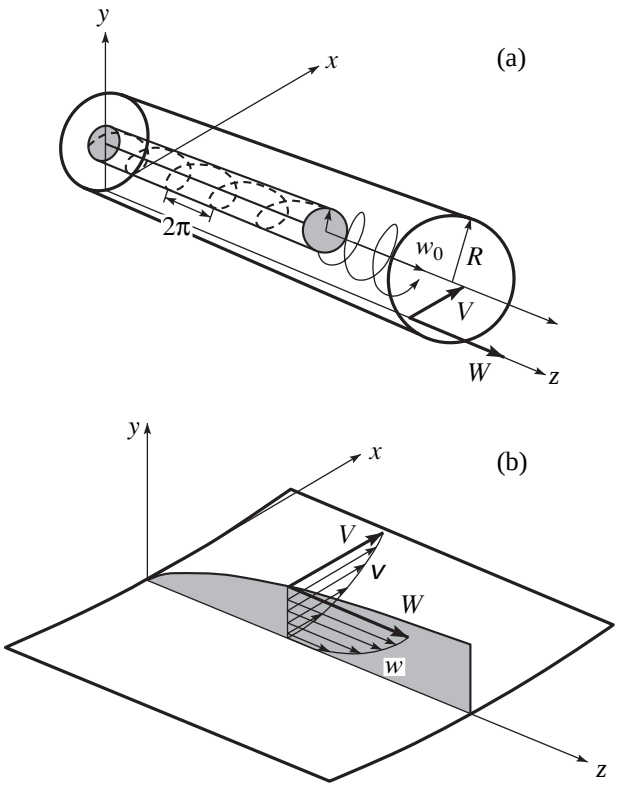

Fig. 1. (a) Axisymmetric vortex structure inducing swirling flow in a reactor tube and (b) a coordinate system for the boundary layer on the tue wall. Dashed curve in (a) shows a screw current line in the vortex core; solid curve is the liquid particle trajectory.

stant character of the viscous flow along the mass exchange section (i.e., constant V and W vales), we have $\partial p/\partial z = 0$. This condition leads to the complete coincidence of two equations in the system for the 3D boundary layer, from which it follows that $v/w = V/W$. The two remaining independent equations correspond to the case of a boundary layer in a plane-parallel plate. Therefore, the friction stresses at the tube surface can be expressed as

$$\tau_\varphi = \mu\frac{\partial u}{\partial y}\bigg|_{y=0} = 0.332\sqrt{\frac{\mu\rho W}{z}}V,$$
$$\tau_z = \mu\frac{\partial w}{\partial y}\bigg|_{y=0} = 0.332\sqrt{\frac{\mu\rho W}{z}}W, \qquad (2)$$

where μ is the dynamic viscosity and ρ is the liquid density.

Proceeding to consideration of the mass exchange process, note that the flow velocity components in a thin diffusion layer occurring deep in the boundary layer can be expressed (after expanding into the Taylor series and neglecting small terms) through the friction stress components (2) on the wall:

$$u = -\frac{1}{2}y^2\left(\frac{\partial}{\partial x}\frac{\partial v}{\partial y} + \frac{\partial}{\partial z}\frac{\partial w}{\partial r}\right)\bigg|_{y=0};$$
$$v = y\frac{\partial v}{\partial y}\bigg|_{y=0}; \quad w = y\frac{\partial w}{\partial y}\bigg|_{y=0}, \qquad (3)$$

where the formula for the velocity component u follows from the equation of continuity. Taking into account the above assumptions and using relationships (2) and (3), the equation of stationary diffusion inside a thin diffusion layer can be written as

$$\frac{\tau_z}{\mu}y\frac{\partial c}{\partial z} - \frac{1}{2\mu}\frac{\partial \tau_z}{\partial z}y^2\frac{\partial c}{\partial y} + \frac{\tau_\varphi}{\mu}y\frac{\partial c}{\partial x} = D\frac{\partial^2 c}{\partial y^2}, \qquad (4)$$

with the corresponding boundary conditions

$$c = c_\infty \quad \text{for} \quad z = 0 \quad \text{or} \quad y \longrightarrow \infty;$$
$$c = 0 \quad \text{for} \quad y = 0 \quad \text{and} \quad 0 \le z \le L. \qquad (5)$$

The fact that the boundary conditions (5) are independent of the angular coordinate allows us to ignore the dependence on x in Eq. (4), which leads to the absence of a convective mass transfer in the tangential direction of the mass exchange reactor section. As a result, the integration of Eq. (4) with the boundary conditions (5) can be performed by analogy with the problem of diffusion in a plane-parallel plate [8]. This procedure leads to the following relationship for the coefficient of mass transfer from the flow to the cylinder wall:

$$k(z) = -\frac{D}{c_\infty}\frac{\partial c}{\partial y}\bigg|_{y=0} = \frac{D}{\delta(z)};$$
$$\delta(z) = 2.95Sc^{-1/3}\left(\frac{\nu z}{W}\right)^{1/2}. \qquad (6)$$

Accordingly, the Sherwood number averaged over the surface is

$$\overline{Sh} = \frac{1}{D}\int_0^L k(z)dz = 0.678Sc^{1/3}\left(\frac{WL}{\nu}\right)^{1/2}. \qquad (7)$$

Therefore, within the framework of the axisymmetric flow model, the effect of the flow swirling on the mass transfer characteristics (6) and (7) can be manifested only through some features in behavior of the axial flow velocity component in the nonviscous flow. However, this very component behaves rather ambiguously. Indeed, swirling flows exhibit at least two essentially different flow regimes featuring right- and left-

handed vortices generating flows with streamlike (maximum on axis) and tracelike (minimum on axis) profiles of the axial velocity component [4]. The possibility of both regimes was experimentally established by studying the vortex decay in a broad range of the flow-rate-average Reynolds number (1500–300000) [9–11].

The phenomenon was explained [5] in terms of the possible existence of two vortex structures with different screw symmetries under the same integral flow parameters. Indeed, ignoring losses in a thin boundary layer, the swirling flows in cylindrical tubes must be characterized by constant integral flow parameters including the flow rate Q; velocity circulation Γ; and the axial fluxes of the momentum moment M, momentum J, and energy E. The results of calculations [5, 6] confirmed that, provided the same integral characteristics at the entrance of the working section, all flow regimes with vortex decay [9–11] may feature two different vortex structures (1), with a right-handed vortex ($l > 0$) present in the swirling flow before the decay and a left-handed vortex ($l < 0$), after the decay.

For the mass exchange analysis, let us consider two vortex structures with different screw symmetries existing under the same integral flow parameters (see table). In order to exclude the (different) contributions due to tangential velocity components ignored in the model (7), both structures are assumed to possess equal values of this component on the tube wall, although the axial velocity components are different (Fig. 2). In addition, the last column in the table gives the ratios of the Sherwood numbers (7) to the corresponding values calculated for a nonswirling laminar flows with the same flow rate [8]. The mass transfer has proved to be smaller for flows with the right-handed vortices than for the analogous flows with the left-handed vortices. Moreover, the former mass transfer was also significantly lower as compared to that for a purely axial nonswirling flow (as indicated by the Sherwood number ratio in the table being lower than unity).

Thus, we have developed for the first time a mathematical model of mass transfer in a simplest swirling nondecaying flow. Within the framework of this model, we demonstrated the possibility of the mass transfer being different in the flows with the opposite screw symmetries of the vortex field. When a vortex with the right-handed screw symmetry appears in the flow core (generating a streamlike axial velocity profile), the mass transfer from flow to wall will be smaller than that in the case of a purely axial nonswirling flow.

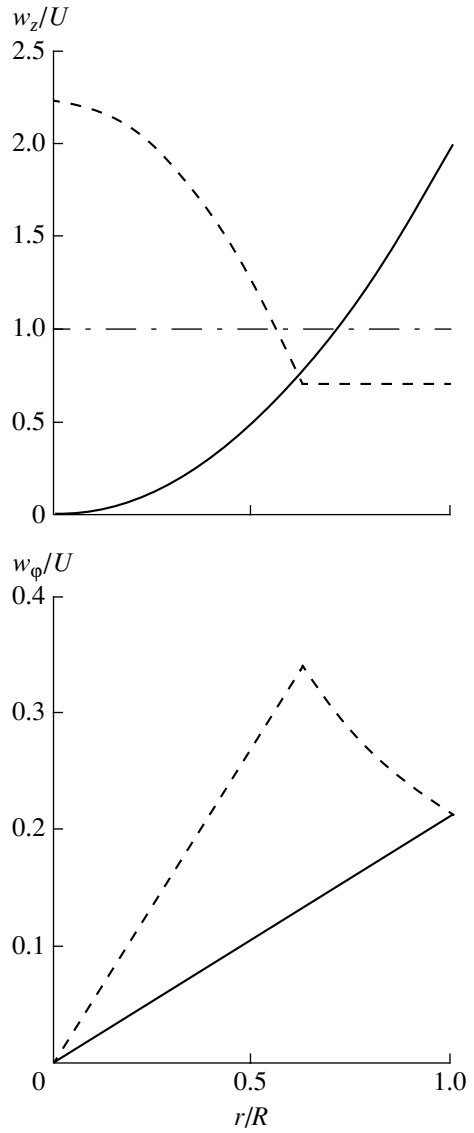

Fig. 2. Flow velocity component profiles (normalized to the average flow-rate velocity U) for the flows with different symmetry of the vortex field for the same integral flow parameters: right-handed vortex (dashed curves); left-handed vortex (solid curves); axial velocity in a nonswirling flow (dot–dashed curve).

Comparative data on the mass exchange rate in swirling flows with different screw symmetries of the vortex field

Integral parameters	G/RU	$Q/\rho UR^2$	$M/\rho U^2R^3$	$J/\rho U^2R^2$	$E/\rho U^3R^2$	Relative mass exchange rate $\overline{Sh}_{swirl}/\overline{Sh}_{axial}$
	0.212	3.142	0.444	4.224	3.236	
Vortex structure parameters	Γ/UR	$2\pi l/R$	ε/R	w_0/U	$p_0/\rho U^2$	
Right-handed	0.212	0.879	0.623	2.4	0.07	0.84
Left-handed	0.212	–0.667	1.0	0.0	0.0	1.414

Acknowledgments. This study was supported by the Russian Foundation for Basic Research, project no. 00-05-65463.

REFERENCES

1. P. Legentilhomme, A. Aouabed, and J. Legrand, Chem. Eng. J. **52**, 137 (1993).
2. S. Yapici, M. A. Patrick, and A. A. Wragg, J. Appl. Electrochem. **25**, 15 (1995).
3. M. S. de Sa, E. Shokry, and I. V. Soegiarto, Can. J. Chem. Eng. **69**, 294 (1991).
4. S. V. Alekseenko *et al.*, J. Fluid Mech. **382**, 195 (1999).
5. V. L. Okulov, Pis'ma Zh. Tekh. Fiz. **22** (19), 47 (1996) [Tech. Phys. Lett. **22**, 798 (1996)].
6. T. O. Murakhtina and V. L. Okulov, Pis'ma Zh. Tekh. Fiz. **26** (10), 66 (2000) [Tech. Phys. Lett. **26**, 432 (2000)].
7. H. Schlichting, *Boundary-Layer Theory* (McGraw-Hill, New York, 1979, 7th ed.).
8. V. A. Levich, *Physicochemical Hydrodynamics* (Prentice Hall, Englewood Cliffs, New York, 1962).
9. S. Leibovich, Annu. Rev. Fluid Mech. **10**, 221 (1978).
10. M. Escudier, Prog. Aerosp. Sci. **25**, 189 (1988).
11. T. Sarpkaya and F. Novak, AIAA Pap., No. 99-0135, 1 (1999).

Translated by P. Pozdeev

Technical Physics Letters, Vol. 27, No. 9, 2001, pp. 769–772. Translated from Pis'ma v Zhurnal Tekhnicheskoĭ Fiziki, Vol. 27, No. 18, 2001, pp. 29–35.

On the Problem of Solar Magnetic Field Generation

Yu. V. Vandakurov

Ioffe Physicotechnical Institute, Russian Academy of Sciences, St. Petersburg, 194021 Russia

Received March 29, 2001

Abstract—Generation of a nonaxisymmetric, predominantly toroidal magnetic field in the convective layer of the Sun is considered assuming that the process is related to a decrease in the energy consumed for the convective heat transfer. It is also assumed that the field is antisymmetric relative to the equatorial plane and the field strength varies in proportion to the sine or cosine of the azimuthal angle. It is shown that the field strength increases when both a radial gradient of the angular rotation velocity and a steady-state axisymmetric meridional substance circulation are present. A change in the direction of the poloidal motion (leading to a change in the overall field sign) is assumed to take place on attaining a limiting field strength. This is probably related to the excitation of the corresponding turbulent medium viscosity. In the proposed model, a restart of the field generation process is induced by a change in the magnetic field sign. *© 2001 MAIK "Nauka/Interperiodica".*

Recently [1], a hypothesis was put forward that a driving force for the solar magnetic field generation is the formation of a state with minimum energy consumed for the convective heat transfer [1]. In other words, it is suggested that the thermal to magnetic energy conversion favors a decrease in the energy consumption. In this context, it is of interest to study nondissipative processes of the magnetic field generation. According to Krause and Rädler [2], there is ground to believe that spherical dynamos related to the meridional circulation may exist, representing modified dynamos of the type proposed by Gailitis [3], in which case the fluctuational motions play no significant role and only nonaxisymmetric magnetic fields may be generated. It should be noted that Gailitis studied the problem of field excitation by a system of two stationary axisymmetric ring vortices.

Below, we will consider one possible variant of such a nonviscous interaction between a nonstationary nonaxisymmetric field and stationary, symmetric relative to the equator, distributions of the rotation and meridional circulation, assuming the field and circulation to possess opposite symmetries. In addition, we assume that the main field is toroidal while containing a small poloidal component. It will be demonstrated that a field with the strength varying with the azimuthal angle φ by the $\sin\varphi$ of $\cos\varphi$ law increases in the presence of both a radial gradient of the angular rotation velocity and a steady-state meridional circulation corresponding to the substance slowly emerging or sinking in equatorial regions and moving in the reverse directions at high altitudes. Below, we will assume that both these assumptions are satisfied. The fact that, in the general case, a radial gradient of the angular rotation velocity in the convective layer of the Sun is nonzero is confirmed by observations [4].

All the vector (and scalar) quantities are represented by expansions over complete system of orthogonal vector spherical harmonics $\mathbf{Y}_{J,M}^{(\lambda)}$ (or spherical functions $Y_{J,M}$) representing functions of angular variables, where $\lambda = 0, \pm 1$; index J is a nonnegative integer, and M is the azimuthal number (see [5]). Coefficients in the expansions under consideration are, for example, $v_{J,M}^{(\lambda)} = v_{JM}^{(\lambda)}$, $B_{J,M}^{(\lambda)}$, and $\rho_{J,M}$ (in the case of hydrodynamic velocity **v**, magnetic field **B**, and density ρ). These quantities depend on the radius r and time t (r, ϑ, and φ constituting a spherical coordinate system).

The general relationships for the expansion coefficients, following from the equilibrium equations for all nonlinear forces, were considered elsewhere [6, 7]. The same relationships can be applied to the study of induction equation, which (in the case when vectors **v** and **B** obey the aforementioned symmetry conditions and the medium is ideally conducting) can be reduced to the following equations:

$$\left(\frac{\partial}{\partial t} + iM\Omega\right)B_{J,M}^{(0)}$$

$$= \frac{a}{r}\{(J^2-1)^{1/2} f_J D_{J-1,M} - [J(J+2)]^{1/2} g_J D_{J+1,M}\}, \quad (1)$$

$$J = 1, 3, \ldots,$$

$$\left(\frac{\partial}{\partial t} + iM\Omega\right)B_{J,M}^{(-1)}$$

$$= \frac{a}{r} M (30)^{1/2} v_{20}^{(-1)} [f_J B_{J-1,M}^{(0)} + g_J B_{J+1,M}^{(0)}], \quad (2)$$

$$J = 2, 4, \ldots,$$

1063-7850/01/2709-0769$21.00

where

$$f_J = \left[\frac{J+1}{J(2J-1)(2J+1)}\right]^{1/2},$$
$$g_J = \left[\frac{J}{(J+1)(2J+1)(2J+3)}\right]^{1/2}, \quad (3)$$

$$D_{J,M} = \frac{\partial}{\partial r} r v_{10}^{(0)} B_{J,M}^{(-1)}$$
$$- [J(J+1)]^{1/2} v_{10}^{(0)} B_{J,M}^{(+1)} = r^2 B_{J,M}^{(-1)} \frac{\partial}{\partial r}\left[\frac{v_{10}^{(0)}}{r}\right], \quad (4)$$

$M = \pm 1$, $a = (3/8\pi)^{1/2}$, and $\Omega = i(a/r) v_{10}^{(0)}$ is the angular rotation velocity; in Eq. (1) for the main toroidal field component, terms of the order of $(v_{20}^{(+1)}/r) B_{J,M}^{(0)}$ were omitted.

Equations (1) and (2) contain both rapidly oscillating (with the angular rotation velocity Ω) and slowly varying terms. The latter have the frequency on the order of $[i\psi]^{1/2}$, where $\psi = v_{20}^{(-1)}(d\Omega/dr)$. Note that, in the case of differential rotation with respect to altitude, the circular frequencies of fast oscillations usually differ from the angular rotation velocity [8].

The passage to equations describing slow oscillations can be performed using the substitution

$$B_{J,M}^{(\lambda)} = e^{-iM\Omega t} Q_{J,M}^{(\lambda)}. \quad (5)$$

This transformation leads to equations with the right-hand parts analogous to those in Eqs. (1) and (2), involving the slowly varying variables $Q_{J,M}^{(0)}$ and $Q_{J,M}^{(-1)}$. For example,

$$\frac{\partial}{\partial t} Q_{J,M}^{(-1)} = M \frac{1}{r}\left(\frac{45}{4\pi}\right)^{1/2} v_{20}^{(-1)} [f_J Q_{J-1,M}^{(0)} + g_J Q_{J+1,M}^{(0)}], \quad (6)$$
$$M = \pm 1.$$

This equation can be used to exclude, for example, the variable $Q_{J,M}^{(-1)}$, after which we arrive at the following system:

$$\frac{\partial^2}{\partial t^2} Q_{J,M}^{(0)} = -iM\left(\frac{45}{4\pi}\right)^{1/2} \psi \{(J^2-1)^{1/2} f_J \times [f_{J-1} Q_{J-2,M}^{(0)} + g_{J-1} Q_{J,M}^{(0)}]$$
$$- [J(J+2)]^{1/2} g_J [f_{J+1} Q_{J,M}^{(0)} + g_{J+1} Q_{J+2,M}^{(0)}]\}, \quad (7)$$
$$J = 1, 3, \ldots, \quad M = \pm 1.$$

In this approximation, the radial variation of the velocity $v_{20}^{(-1)}$ is determined by the relationship

$$\psi = v_{20}^{(-1)} d\Omega/dr = \text{const}, \quad (8)$$

and the condition of slow variation of the quantities $Q_{J,M}^{(0)}$ in time is satisfied when $|\psi|^{1/2} \ll \Omega$. In addition, the small quantities omitted in deriving Eq. (1) are much smaller than the remaining terms provided that

$$v_{20}^{(+1)}/(r|\psi|^{1/2}) \ll 1. \quad (9)$$

It is important to note that, in the case of a poloidal motion for which condition (8) is satisfied, the coefficients in Eq. (7) are constant. Therefore, the initial system of partial differential equations is reduced to a system of ordinary differential equations (7) for the coefficients $Q_{J,M}^{(0)}(r, t)$, where radius r is a parameter of the problem. This circumstance evidences validity of the procedure used to pass to the slowly varying variables (despite the fact that we are dealing with a medium rotating with different angular velocities at various depths).

Since the coefficients of equations in system (7) are constant, the general solution can be written in the form of $\sum_k A_k \exp(\sigma_k t)$, where $A_k = \text{const}$, k is the number of a partial solution, and σ_k are the roots of the characteristic equation obtained from system (7) upon replacing $\partial/\partial t$ by σ_k. Upon finding from this system the dimensionless complex eigenvalues

$$q_k = \sigma_k^2/[M(45/4\pi)^{1/2}\psi], \quad (10)$$

we can use relationship (10) to determine the squares of the reciprocal growth times (for $\sigma_k > 0$) or decay times (for $\sigma_k < 0$) for all k modes. The calculations were performed upon leaving only N coefficients $Q_{J,M}^{(0)}$ in Eqs. (7). For example, only the coefficient $Q_{1,M}^{(0)}$ is nonzero and $k = 1$ for $N = 1$. In the next approximation ($N = 2$), there appears one more coefficient $Q_{3,M}^{(0)}$ and

Table

N	q_k		$\mathrm{RE}[(q_k)_{\max}^{12}]$
1	0.0000 + *i*0.1000		0.2236
2	±0.0649 + *i*0.0417		0.2665
3	±0.0799 + *i*0.0199	0.0000 + *i*0.0359	0.2847
4	±0.0824 + *i*0.0146	±0.0250 + *i*0.0211	0.2882

an additional mode $k = 2$, etc. The solutions q_k for the models corresponding to N varying from 1 to 4 are presented in the table.

Most interesting are the rapidly growing modes characterized by the maximum positive real parts of the $(q_k)^{1/2}$. In our case, these real parts are nonzero; denoted by $\mathrm{Re}[(q_k)^{1/2}_{\max}]$, these values are listed in the last column of the table. Substituting these into formula (10), we obtain the corresponding positive values of $\mathrm{Re}(\sigma_k)$. As is seen, the real parts attain an asymptotic level for $N = 3$, after which the values cease to depend on N. The value corresponding to this level is the required problem solution. Note, however, that $\mathrm{Im}(\sigma_k)$ may significantly depend on the character of the differential rotation with respect to altitude.

It should be emphasized that a change in the poloidal rotation direction leads to alternation of the sign of the generated magnetic field. Indeed, the signs of the coefficients $v_{20}^{(-1)}$, $B_{J,M}^{(-1)}$, and $D_{J,M}$ are uniquely related to each other. In addition, a change in one of these signs implies a transition to another solution for the eigenvalue q_k characterized by the maximum growth rate of the overall magnetic field amplitude. The last transition is accompanied by a change in the sign of the toroidal field.

The above results allow us to make two important conclusions. First, the oscillatory mode growing in time exists for all signs of the $v_{20}^{(-1)}$ coefficient and the radial gradient of the angular rotation velocity $d\Omega/dr$. Second, the characteristic time τ of the most rapidly growing field modes weakly depends on the number N of retained modes for $N > 3$. Assuming that $q_{\max}^{1/2} \approx 0.29$, we obtain

$$\tau \approx 2.5|\psi|^{-1/2}. \quad (11)$$

In the larger, bottom part of the convective layer of the Sun, the gradient $d\Omega/dr$ can be approximately taken equal to $0.1\Omega/r$ (see, e.g., [4]). Then the time τ is approximately equal to the solar cycle duration (i.e., on the order of 10 years) for $v_{20}^{(-1)} \sim 10$ cm/s. In this case, the horizontal poloidal velocities are greater than the radial velocities by a factor of about $|d\ln\rho/d\ln r|$. Under these conditions, condition (9) will be satisfied as far as we deal with the bottom half of the solar convective layer.

A different situation takes place in the subsurface layer of the solar convective zone, where the radial gradient of the angular rotation velocity is negative, while its absolute value is probably two orders of magnitude greater than the value cited above. Under these conditions (for the same value of the $v_{20}^{(-1)}$ coefficient), the magnetic field generation may proceed at a rate ten times greater than that considered above. It is also not excluded that this relatively rapid process is related to the quasi-biannual cycle of the magnetic field generation studied in [9]. In this case, the horizontal poloidal velocities in the subsurface layer of the solar convective zone may be on the order of 10 m/s and condition (9) will be satisfied provided the gradient $|d\Omega/dr|$ is sufficiently high.

As is known, motions with the velocities about 50 m/s in a layer bounded by the relative radii 0.97 and 0.999 were revealed by Gonzalez *et al.* [10] by analysis of the helioseismicity data. The value of the observed velocity was close to (or even somewhat greater than) that cited above.

Thus, the equations derived above are indicative of a spontaneous exponential growth of the magnetic field, mostly of the main toroidal component, in the convective layer of the Sun in the presence of a nonzero radial angular velocity gradient and a slow steady-state meridional circulation of the type considered above. It can be expected that, in the stage when the field strength would attain a maximum level, a convective magnetic viscosity must be excited that would favor both termination of the field growth and displacement of the magnetic field toward higher layers. However, in our model, the thermal to magnetic energy conversion is related to a decrease in the energy consumed for the convective heat transfer. Therefore, we may expect the energy conversion to restart upon changing (apparently, under the action of a turbulent viscosity) the direction of a slow meridional circulation. This will be accompanied by a change in the sign of the generated magnetic field. We suggest that, as a result, a new field with the opposite sign will start to form in the layer below the emerging magnetic field zone. The hypothesis, according to which this scheme may describe some general features of the solar cycle, is worthy of further investigation.

In concluding, it should also be noted that a characteristic value of the magnetic field strength was estimated [1, 7, 11] based on the comparison with the observed altitude variation of the angular rotation velocity. According to these estimates, a nonaxisymmetric toroidal field is on the order of 10 kG. This value agrees with the value of a total fraction of the solar energy converted into the magnetic field energy, which was estimated at about 0.1% [12].

Acknowledgments. This study was supported by the "Integration" Foundation (contract no. KO0854) and by the Russian Foundation for Basic Research (project no. 00-02-16939).

REFERENCES

1. Yu. V. Vandakurov, Pis'ma Astron. Zh. **25**, 868 (1999) [Astron. Lett. **25**, 758 (1999)].

2. F. Krause and K. Rädler, *Mean-Field Magnetohydrodynamics and Dynamo Theory* (Akademie-Verlag, Berlin, 1980; Mir, Moscow, 1984).
3. A. Gaĭlitis, Magn. Gidrodin. **1**, 19 (1970).
4. J. Schou, H. M. Antia, S. Basu, *et al.*, Astrophys. J. **505**, 390 (1998).
5. D. A. Varshalovich, A. N. Moskalev, and V. K. Khersonskii, *Quantum Theory of Angular Momentum* (Nauka, Leningrad, 1975; World Scientific, Singapore, 1988).
6. Yu. V. Vandakurov, Astron. Zh. **76**, 29 (1999) [Astron. Rep. **43**, 24 (1999)].
7. Yu. V. Vandakurov, Astron. Zh. **78**, 253 (2001) [Astron. Rep. **45**, 216 (2001)].
8. Yu. V. Vandakurov, Izv. Vyssh. Uchebn. Zaved., Radiofiz. (2001) (in press).
9. E. E. Benevolenskaya and V. I. Makarov, Pis'ma Astron. Zh. **18**, 195 (1992) [Sov. Astron. Lett. **18**, 108 (1992)].
10. I. González Hernández, J. Patrón, R. S. Bogart, *et al.*, Astrophys. J. Lett. **510**, L153 (1999).
11. Yu. V. Vandakurov, Pis'ma Zh. Tekh. Fiz. **25** (10), 82 (1999) [Tech. Phys. Lett. **25**, 415 (1999)].
12. P. A. Foukal and J. Lean, Astrophys. J. **328**, 347 (1988).

Translated by P. Pozdeev

Technical Physics Letters, Vol. 27, No. 9, 2001, pp. 773–775. Translated from Pis'ma v Zhurnal Tekhnicheskoĭ Fiziki, Vol. 27, No. 18, 2001, pp. 36–42.

The Features of Vacancy Formation at Low Temperatures

M. N. Magomedov

Institute for Problems of Geothermics, Dagestan Scientific Center, Russian Academy of Sciences, Makhachkala, Dagestan, Russia

e-mail: danterm@datacom.ru

Received March 14, 2001

Abstract—Expressions for the calculation of the thermodynamic potential, enthalpy, entropy s_v, and volume of vacancy formation in a simple crystal at temperatures close to absolute zero are derived. It is established that the vacancy concentration Φ as a function of the temperature T exhibits a minimum at a certain temperature T_0. At $T < T_0$, the $\Phi(T)$ function increases with decreasing temperature; the $s_v(T)$ value changes sign at $T = T_0$ and is negative at $T < T_0$. It is shown that the existence of the "zero-point vacancies" does not violate the third law of thermodynamics. Three new effects are predicted, and the prospects for their experimental observation are considered. © *2001 MAIK "Nauka/Interperiodica".*

The possibility for vacancies to exist at $T = 0$ was predicted by Andreev and Lifshits long ago [1], but the properties of such "zero-point vacancies" are still poorly studied. In particular, the temperature and pressure dependences of the parameters of vacancy formation in the temperature interval from zero to Debye temperature (Θ_D) are still unclear. The purpose of this study was to estimate the probability of the "zero-point vacancy" formation and determine the entropy (s_v) and volume (v_v) of vacancy formation in the low-temperature range ($0 \le T \ll \Theta_D$).

Previously [2–4], an expression for the thermodynamic potential (Gibbs free energy) of the vacancy formation was obtained in the following form:

$$g_v = -k_B T \ln(\Phi),$$
$$\Phi = (2/\pi^{1/2}) \int_{(E_v/k_B T)^{1/2}}^{\infty} \exp(-t^2) dt, \quad (1)$$

where k_B is the Boltzmann constant, Φ is the probability of detecting a vacancy, and E_v is the energy barrier for an atom to leave the lattice site. Based on the Einstein crystal model, the expression for the latter quantity is [2–4]

$$E_v = m(k_B c\Theta)^2 f(y)/4k_n\hbar^2, \quad (2)$$

where m is the atom mass; c is the distance between centers of the nearest neighbors; Θ is the Einstein temperature; k_n is the coordination number; $\hbar$ is the Planck constant; and

$$f(y) = [1 - \exp(-y)]/\{y[1 + \exp(-y)]\},$$
$$y = \Theta/T. \quad (3)$$

For the enthalpy, entropy, and volume of vacancy formation, we may use the conventional expressions [5]

$$h_v = -(d\ln(\Phi)/d(1/k_B T))_p = k_B T(\Phi_T + \alpha_p T\Phi_v),$$
$$s_v = -(dg_v/dT)_p = h_v/T + k_B \ln(\Phi), \quad (4)$$
$$v_v = (dg_v/dP)_T = \Phi_v k_B T/B_T,$$

where $\alpha_p = V^{-1}(dV/dT)_p$ is the isobaric thermal expansion coefficient; $B_T = -V(dP/dV)_T$ is the isothermal bulk compression modulus; and

$$\Phi_T = (d\ln(\Phi)/d\ln(T))_v = 1 - (d\ln(E_v)/d\ln(T))_v,$$
$$\Phi_v = (d\ln(\Phi)/d\ln(V))_T = -(d\ln(E_v)/d\ln(V))_T.$$

As was demonstrated in [2–5], most substances in the temperature interval up to the melting point (T_m) obey the condition $E_v \gg k_B T_m$. Therefore, the probability Φ can be expressed with a good accuracy using the expansion

$$\Phi \cong (k_B T/\pi E_v)^{1/2} \exp(-E_v/k_B T), \quad (5)$$

from which we obtain

$$\Phi_T = (E_v/k_B T)[1 - t(1 + \eta) + 2\eta],$$
$$\Phi_v = (E_v/k_B T)[\gamma(2 - t) - 2/3], \quad (6)$$

where $\gamma = -(d\ln(\Theta)/d\ln(V))_T$ is the isothermal Gruneisen parameter, and

$$t = -d\ln(f)/d\ln(y) = 1 - 2y\exp(-y)/[1 - \exp(-2y)],$$
$$\eta = -(d\ln(\Theta)/d\ln(T))_v. \quad (7)$$

At high temperatures ($T \gg \Theta$), the f value is close to unity and the quantities t and η are negligibly small. In this case, E_v is independent of T and expression (5) converts into a well-known Arrhenius relationship [5].

1063-7850/01/2709-0773$21.00

Since $\alpha_p T_m$ is one order of magnitude smaller than unity, the E_v value virtually coincides (as is seen from Eqs. (4) and (6)) with the enthalpy of vacancy formation. The case of high temperatures was studied in sufficient detail for both simple substances [2–4] and for binary cubic crystals [6–9]. The values of h_v, s_v, V_v calculated in [2–4] showed a good fit to the experimental data for both vacancies and Schottky defects in binary crystals. Below, we will use this approach for evaluating the energy of vacancy formation at low temperatures.

In the region of $T < \Theta$, the quantities f and t strongly vary with the temperature and their limiting values are

$$\lim_{T\to 0}(f) = \lim(T/\Theta) = 0,$$
$$\lim_{T\to 0}(t) = 1 - 2\lim[(\Theta/T)\exp(-\Theta/T)] = 1. \quad (8)$$

Another difficulty encountered in the low-temperature interval is that the functions $\Theta(T)$ and $\gamma(T)$ obey relationships of the type [10, 11]

$$\Theta(T) \approx \Theta(0)(1 - \chi T^2), \quad \chi = 3[\pi/2\Theta(0)]^2,$$
$$\gamma(T) \approx \gamma(0)(1 + \chi T^2)/(1 - \chi T^2), \quad (9)$$

where $\Theta(0)$ and $\gamma(0)$ are the Einstein temperature and the Gruneisen parameter at $T = 0$. Taking into account that $\alpha_p(0) = 0$ [5], one may readily derive from Eqs. (1)–(9) that

$$\Phi(0) = \lim_{T\to 0}(\Phi) = (\pi M)^{1/2}\exp(-M),$$
$$\lim_{T\to 0}(g_v/k_B T) = M + 0.5\ln(\pi M), \quad \lim_{T\to 0}(h_v/k_B T) = 0,$$
$$s_v(0)/k_B = -\lim_{T\to 0}(g_v/k_B T) = -M - 0.5\ln(\pi M), \quad (10)$$
$$\lim_{T\to 0}(V_v B_T/k_B T) = M[\gamma(0) - 2/3],$$

where M is the parameter equal to the ratio of the energy barrier for the vacancy formation to the energy of zero-point oscillations per degree of freedom:

$$M = \lim_{T\to 0\,K}(E_v/k_B T) = 2E_{v0}/k_B\Theta(0), \quad (11)$$

$$E_{v0} = m[k_B c(0)\Theta(0)]^2/4k_n\hbar^2. \quad (12)$$

Here, $c(0)$ is the distance between centers of the nearest neighbors and $\Theta(0)$ is the Einstein temperature (both at $T = 0$) and $\Theta(0) = 3\Theta_D(0)/4$ [5].

Using the values of $c(0)$ and $\Theta_D(0)$ reported in [12–18], we obtain the following estimates:

M = 0.6–0.9, $\Phi(0)$ = 0.4–0.2 for bcc or hcp ^{3}He and ^{4}He;

M = 1.4–4.0, $\Phi(0) = 0.1–5 \times 10^{-3}$ for hcp p-H_2;

M = 2.3–5.5, $\Phi(0) = 0.04–9 \times 10^{-4}$ for hcp o-D_2;

M = 6.1–7.3, $\Phi(0) = (5–1.4) \times 10^{-4}$ for fcc Ne;

M = 23–25, $\Phi(0) = 10^{-11}–10^{-12}$ for fcc Ar.

Thus, the M value increases and $\Phi(0)$ decreases when the atomic mass grows. Note also that the E_{v0} value calculated by formula (12) for the above crystals perfectly coincided with the energy of a monovacancy formation in a crystal experimentally estimated at $T \ll \Theta_D$.

Experiments [14–18] gave negative values of the entropy of vacancy formation at low temperatures in bcc and hcp modifications of the ^{3}He and ^{4}He crystals. It was demonstrated that such negative values ($s_v < 0$) do not contradict the thermodynamic conditions for vacancy formation. Proceeding from the above results, we may infer that the vacancy concentration as a function of the temperature has a minimum at a certain temperature T_0. At T decreases below T_0, the $\Phi(T)$ value increases from $\Phi(T_0)$ to $\Phi(0)$ determined in (10). The growth of $\Phi(T)$ with decreasing T in the interval $0 < T < T_0$ is related to the zero-point oscillations of atoms in the crystal. The same factor accounts for negative values of the entropy of vacancy formation in the interval $0 < T < T_0$. The passage of $s_v(T)$ to the region of negative values is caused entirely by the thermodynamic reasons rather than by the "ferromagnetic polarization of nuclear spins around the vacancy" (as was suggested in [15, 16]).

It must be pointed out that the existence of "zero-point vacancies" by no means violates the third law of thermodynamics. This becomes clear if we take into account that the system entropy (per atom) is [5]

$$s = -(dg/dT)_p$$
$$= -(dg/dT)_{p,\Phi} - (dg/d\Phi)_{p,T}(d\Phi/dT)_p, \quad (13)$$

where g is the thermodynamic potential (per atom) of the crystal. The first term in this expression is the entropy (per atom) of the crystal, which is related to a change in the thermodynamic parameters. Within the framework of the Einstein model, the first term in Eq. (13) decreases in proportion to $\exp(-\Theta/T)$ when $T \longrightarrow 0$ [5]. The second term in Eq. (13) is the entropy (per atom) of the crystal, which is related to a change in the vacancy concentration. Taking into account that $g_v = (dg/d\Phi)_{p,T}$ [5], the second term in Eq. (13) can be transformed so as to take the form $(g_v/k_B T)\Phi(h_v/T)$. According to Eq. (10), this function vanishes at $T = 0$ and, hence, the existence of the "zero-point vacancies" does not contradict the third law of thermodynamics in the Planck formulation: $s(0) = 0$ [20].

Thus, proceeding from the above results, we may conclude that there are three low-temperature effects which have to be observed in experiment:

(i) The concentration of vacancies as a function of the temperature must exhibit a minimum at a certain point $T = T_0$. When the temperature decreases in the interval $0 < T < T_0$, the function $\Phi(T)$ increases from $\Phi(T_0)$ to $\Phi(0)$.

(ii) The function $s_v(T)$ is negative in the interval $0 < T < T_0$. As a result, the isobaric formation of vacancies

at $T < T_0$ is accompanied by the evolution of heat at an amount of Ts_v.

(iii) As the temperature tends to zero, the vacancy concentration ceases to depend on the pressure (i.e., on the density). At $T = 0$, the volume of vacancy formation is zero: $v_v(0) = (dg_v/dP)_{T=0} = 0$.

Let us consider in more detail the problem of experimental observation of these low-temperature effects. As for the minimum in $\Phi(T)$, this feature is easily revealed by consequently connecting the experimental points in the $\Delta a/a_0$ versus T plot presented in [14, Fig. 5] for fcc ^{3}He ($\Delta a = a - a_0$ is the change in the lattice parameter as a result of the vacancy formation). Unfortunately, the authors of [14] tried to fit these points to the exponential (Arrhenius) relationship between vacancy concentration and temperature, which hindered the possibility of detecting the $\Phi(T)$ minimum.

As for the second effect, the heat evolution during the vacancy formation at $T < T_0$ agrees with the conclusion at which Andreev and Lifshits arrived [1]: at $T = 0$, it is energetically favorable for the crystal to come into a state where some part of the lattice sites is vacant. Note that this property is by no means characteristic of only the quantum crystals. Inherent in all substances, this effect is merely more significantly pronounced in ^{3}He and ^{4}He crystals where amplitude of the zero-point oscillations is relatively large. Therefore, the effect of heat evolution during the low-temperature vacancy formation will be more readily observed for helium, the more so that the phenomenon of $s_v < 0$ in this crystal is known for a long time [14–18].

The third effect, $v_v(0) = 0$, is essentially a consequence of the fact that, according to Eq. (1), the function g_v ceases to depend on pressure in the vicinity of $T = 0$ and becomes constant $g_v = 0$ (although g_v/k_BT tends to a nonzero constant value determined in (10) for $T \longrightarrow 0$). The fact that $v_v(0) = 0$ indicates that a finite number $N_v(0)$ of "zero-point vacancies" do not contribute to the total system volume. In other words, the formation of a "zero-point vacancy" leads to relaxation of the lattice parameters such that the total volume of the crystal would coincide with the volume of the ideal vacancy-free crystal at $T = 0$. Thus, the "zero-point vacancy" formation must be accompanied by a decrease in the mean interatomic distance. This contraction is just what accounts for the heat evolution at an amount of Ts_v. It is believed that this contraction also accounts for the negative values of the thermal expansion coefficient recently observed in bcc ^{3}He for $T < 0.2$ K at any pressures [12].

In concluding, note that the transition from the Einstein model employed in this study to a more complicated Debye model will not change the physical essence of the effect described above, since the zero-point oscillations in both models are of the same nature as those related to the Heisenberg uncertainty principle.

Acknowledgments. The author is grateful to Prof. K.M. Magomedov, K.N. Magomedov, and Z.M. Surkhaeva for their help in work.

REFERENCES

1. A. F. Andreev and I. M. Lifshits, Zh. Éksp. Teor. Fiz. **56** (6), 2057 (1969) [Sov. Phys. JETP **29**, 1107 (1969)].
2. M. N. Magomedov, Teplofiz. Vys. Temp. **27** (2), 279 (1989).
3. M. N. Magomedov, Metallofizika **13** (5), 106 (1991).
4. M. N. Magomedov, Izv. Akad. Nauk, Met., No. 5, 73 (1992).
5. L. A. Girifalco, *Statistical Physics of Materials* (Wiley, New York, 1973).
6. M. N. Magomedov, Fiz. Tverd. Tela (St. Petersburg) **34** (12), 3718 (1992) [Sov. Phys. Solid State **34**, 1991 (1992)].
7. M. N. Magomedov, Zh. Fiz. Khim. **67** (4), 661 (1993).
8. M. N. Magomedov, Zh. Fiz. Khim. **68** (4), 589 (1994).
9. M. N. Magomedov, Teplofiz. Vys. Temp. **32** (5), 686 (1994).
10. *Problems in Solid State Physics*, Ed. by H. J. Goldsmid (Academic, New York, 1968).
11. M. N. Magomedov, Zh. Fiz. Khim. **61** (4), 1003 (1987).
12. S. B. Trickey, Q. P. Kirk, and E. D. Adams, Rev. Mod. Phys. **44** (4), 668 (1972).
13. *Cryocrystals*, Ed. by B. I. Verkin and A. F. Prikhod'ko (Naukova Dumka, Kiev, 1983).
14. S. M. Heald, D. R. Baer, and R. O. Simmons, Phys. Rev. B 30 (5), 2531 (1984).
15. I. Iwasa and H. Suzuki, J. Low Temp. Phys. **62** (1/2), 1 (1986).
16. I. Iwasa, J. Phys. Soc. Jpn. **56** (5), 1635 (1987).
17. P. R. Granfors, B. A. Fraass, and R. O. Simmons, J. Low Temp. Phys. **67** (5/6), 353 (1987).
18. M. E. R. Bernier and J. H. Hetherington, Phys. Rev. B **39** (16), 11285 (1989).
19. P. Varotsos and K. Alexopoulos, J. Phys. C **12** (19), L761 (1979).
20. Yu. L. Klimontovich, *Statistical Physics* (Nauka, Moscow, 1982; Harwood Academic, New York, 1986).

Translated by P. Pozdeev

Technical Physics Letters, Vol. 27, No. 9, 2001, pp. 776–778. Translated from Pis'ma v Zhurnal Tekhnicheskoĭ Fiziki, Vol. 27, No. 18, 2001, pp. 43–49.

Temperature Dependence of the Quantum Efficiency of 4H-SiC-Based Schottky Photodiodes

T. V. Blank, Yu. A. Gol'dberg, E. V. Kalinina, O. V. Konstantinov, A. O. Konstantinov, and A. Hallen

Ioffe Physicotechnical Institute, Russian Academy of Sciences, St. Petersburg, 194021 Russia
ACREO AB, Electrum 236, SE 16440 Kista, Sweden
KTH Electrum Department of Electronics, S-16440 Kista, Sweden

Received March 29, 2001

Abstract—Using metal–semiconductor structures based on a pure epitaxial layer of *n*-4H-SiC ($N_d - N_a = 4 \times 10^{15}$ cm^{-3}), UV photodetectors were created with a maximum photosensitivity at 4.9 eV and a quantum efficiency up to 0.3 el/ph. The photosensitivity spectrum of the base structure is close to the spectrum of bactericidal action of the UV radiation. For photon energies in the 3.4–4.7 eV range, the quantum efficiency of the photoelectric conversion exhibits rapid growth with the temperature above 300 K, which is explained by the participation of photons in indirect interband transitions. This growth is not manifested when the photon energy is close to the threshold energy of direct optical transitions in the nondirect-bandgap semiconductor, which allows the threshold energy to be evaluated (~4.9 eV). © *2001 MAIK "Nauka/Interperiodica".*

Introduction. As is known, Schottky diodes based on wide-bandgap semiconductors (such as SiC) are now the most widely used type of UV photodetectors. These devices most frequently employ 6H-SiC layers, the spectra of which extend from 3.3 to 6 eV with a maximum sensitivity at 4.5 eV [1]. The prospects of using 4H-SiC layers in high-temperature and high-voltage photoelectronics were also studied (see, e.g. [2, 3]). Note that the spectral interval of photosensitivity of a surface-barrier structure based on 4H-SiC, extending from 3.9 to 5.2 eV with a maximum response at 4.9, is close to the spectrum of bactericidal action of the UV radiation. For this reason, such detectors may find wide application in medicine and biology. Until now, the spectral dependence of the quantum efficiency of 4H-SiC photodetectors was studied only at room temperature [4, 5].

This paper reports on the temperature dependence of the quantum efficiency of Cr-4H-SiC Schottky diodes measured at various energies of detected photons (3.2–6 eV). This allows us to judge the temperature stability of the photodetector studied and to establish important physical features in the mechanism of photoelectric conversion in this Schottky diode. In particular, the photoelectric conversion mechanism can be influenced by the crystal structure defects present in the subsurface region of a semiconductor, which are known to account for the temperature instability of GaAs and GaP based Schottky photodiodes [6]. Below, we will demonstrate that the system also exhibits another physical feature: a sharp growth of the photocurrent with the temperature in the vicinity of the direct optical absorption threshold. Using this fact, we evaluated the threshold energy.

Sample preparation and measurements. The Schottky barriers were prepared by thermal deposition of Cr in vacuum onto 25-μm-thick epitaxial films of *n*-4H-SiC with the uncompensated donor concentration $N_d - N_a = 4 \times 10^{15}$ cm^{-3}. The semiconductor films were grown by chemical vapor deposition (CVD) from the gas phase onto commercial *n*-4H-SiC substrates with $N_d - N_a = 1 \times 10^{19}$ cm^{-3}. The base ohmic contact was obtained by thermal deposition of Cr into the substrate.

For the photoelectric measurements, the Schottky photodiodes were placed into a thermostat with quartz windows and illuminated with a UV radiation generated by a DRT-300 lamp. This system allowed photodetectors to be studied in a temperature range from 78 to 400 K at the incident photon energies varying from 3.2 to 6 eV. The photocurrent measured in the short-circuit regime was used to determine the quantum efficiency (el/ph = electron/photon) related to the ratio of the response current sensitivity (A/W) to the detected photon energy (eV).

The shortwave photoeffect usually implies the case when all the incident light is absorbed in the photoelectrically active region, for which purpose the light absorption range $L_v = \alpha^{-1}$ (α is the optical absorption coefficient) must be smaller than the sum of the space-charge layer thickness W and the diffusion length L of the minority charge carriers (in this case, holes L_p): $L_v < W + L_p$. The longwave photoeffect represents the opposite case, whereby $L_v > W + L_p$. In the structures studied (with the uncompensated donor concentration

$N_d - N_a = 4 \times 10^{15}$ cm^{-3}), the space-charge layer thickness is $W = 5 \times 10^{-5}$ cm and hole diffusion length is $L_p \sim 2 \times 10^{-4}$ cm. Based on the published data for the spectral dependence of the optical absorption coefficient [7], we conclude that the longwave and shortwave photoeffect conditions in the system studied are satisfied for the photon energies below and above 4.8 eV, respectively.

Spectral characteristics of the photodiode. Figure 1 presents the plots of the quantum efficiency versus photon energy measured at different temperatures. These experimental data show the following.

(i) The photocurrent is virtually absent for the photon energies below 3.2 eV. From this we infer that the (nondirect) bandgap width at $T = 300$ K is ~3.2 eV, in agreement with the published data [7].

(ii) The 4H-SiC based Schottky diode has a quantum efficiency above 10% in the 4.3–5.2 eV spectral interval, with a peak of ~0.3 el/ph at 4.9 eV. The characteristic has a sloping front on the side of low photon energies and decays sharply on the high-energy side.

Temperature dependence of the photocurrent. A comparison of the two curves in Fig. 1 measured at different temperatures shows that the quantum efficiency increases with the temperature. Figure 2 presents the temperature dependences of the quantum efficiency γ measured for various photon energies. At low temperatures (100–200 K), the γ versus T plots exhibit a similar behavior for all photon energies, whereby the quantum efficiency grows with the temperature and tends to saturation. In the shortwave range, this behavior is analogous to what we have previously observed for GaAs and GaP surface barrier structures. The effect is related to trapping and release of electron–hole pairs on the fluctuation traps occurring in the subsurface region of the semiconductor [6]. In the longwave range, the effect is related to a change in position of the absorption edge and to an increase in the hole diffusion length with the temperature.

At high temperatures (above 300 K), the dependence of the quantum efficiency on the temperature differs significantly from that observed previously for both long- and shortwave photoeffect.

The longwave photoeffect is characterized by the presence of a high-temperature interval where γ rapidly grows with the temperature. This behavior reflects the effect of phonons favoring the indirect interband optical transitions, the probability of which increases with the number of phonons (i.e., with the temperature). The photon energy at which the rapid high-temperature growth ceases equals precisely to the indirect interband transition energy. By our data, this value is close to 4.9 eV. Published data contain only theoretically estimated values of the direct optical transitions falling within 5–6 eV [6], which also agrees with our estimate.

No such quantum efficiency growth region is observed in the shortwave range, where the photoelectric effect involves predominantly the direct optical transitions.

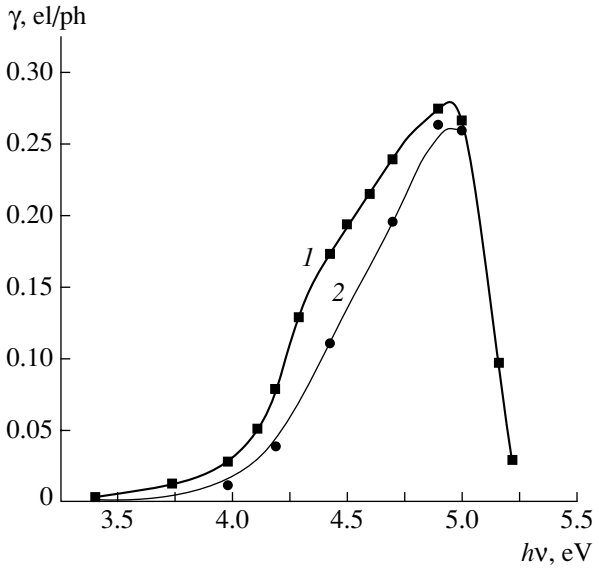

Fig. 1. Plots of the quantum efficiency versus photon energy for Cr-4H-SiC Schottky barrier photodiodes measured at $T = 300$ (*1*) and 100 K (*2*).

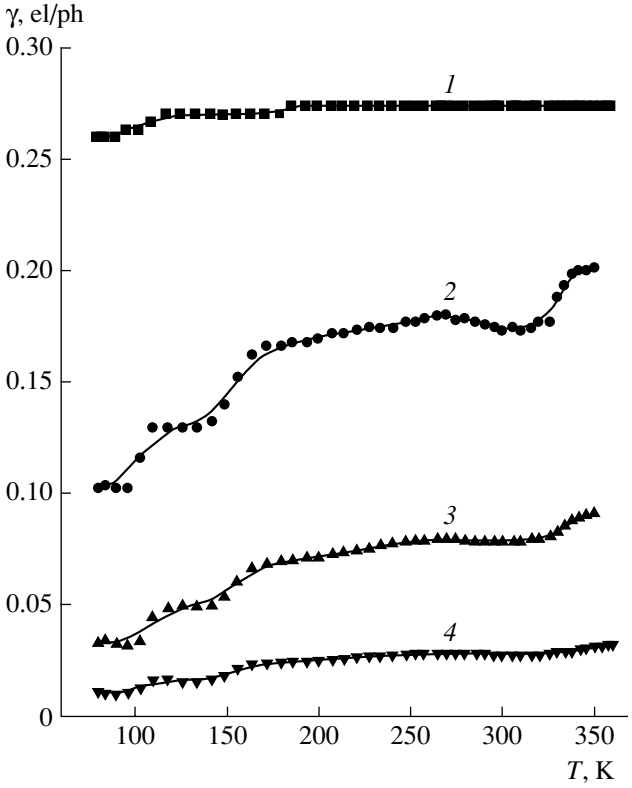

Fig. 2. Plots of the quantum efficiency versus temperature for Cr-4H-SiC Schottky barrier photodiodes measured at various photon energies $h\nu = 5.07$ (*1*), 4.42 (*2*), 4.18 (*3*), and 3.96 eV (*4*).

Energy band model and discussion of experimental results. According to the existing notions, the con-

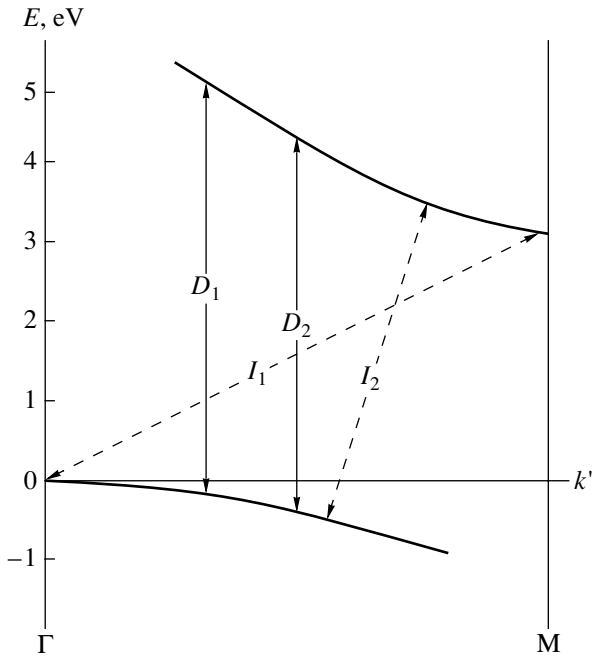

Fig. 3. A schematic diagram of the Brillouin zone of 4H-SiC (see the text for explanations).

duction band minimum in 4H-SiC occurs at the M point of the **k**-space, while the valence band maximum is at the Γ point of the Brillouin zone [7, 8]. Figure 3 shows a schematic diagram of the Brillouin zone for 4H-SiC. Apparently, the interband electron transition upon absorption of a photon with an energy above 3.2 eV initially proceeds as an indirect transition. This is illustrated by the sloping dashed line I_1 (indirect interband transition). As the photon energy increases, the slope of the dashed line decreases, as illustrated by the line I_2. Even a slight additional increase in the photon energy at this point renders the optical transition direct, as shown by the solid vertical line D_1 (direct interband transition). Line D_1 corresponds to the threshold of the direct optical transition, which corresponds in our case to a photon energy of 4.9 eV. As the photon energy grows further, the vertical transition line shifts leftward to position D_2.

We may suggest, however, that electrons and holes in this situation would bind to form a hot exciton possessing a higher binding energy (on the order of 0.1 eV). For the energies of detected photons above 5 eV, the photoelectron and photohole are produced in that region of the **k**-space where the conduction band bottom is almost parallel to the valence band top; the electron and hole velocities are oriented in the same direction and are close in absolute values. Therefore, the Coulomb interaction may allow a a hot exciton to form. The possibility of such exciton formation was originally theoretically predicted in [9]. The exciton formation tightly binds electron to hole, preventing them from being separated under the action of the electric field in the space-charge layer. This exciton is capable of leaving the space-charge region to recombine in a quasi-neutral bulk of the semiconductor or in the metal. We believe that this may account for a sharp drop in the quantum efficiency of the photoelectric conversion observed in 4H-SiC-based Schottky photodiodes for the photon energies above 5 eV.

Acknowledgments. This study was supported by the INTAS Foundation, project no. 97-2141.

REFERENCES

1. Boston Electronic Corp., SiC-UV-detectors, Catalog, 1996.
2. Q. Wahab, T. Kimoto, A. Ellison, *et al.*, Appl. Phys. Lett. **72** (4), 445 (1998).
3. S.-K. Lee, C.-M. Zetterling, and M. Ostling, J. Appl. Phys. **87** (11), 8039 (2000).
4. R. G. Verenchikova, Yu. A. Vodakov, D. P. Litvin, *et al.*, Fiz. Tekh. Poluprovodn. (St. Petersburg) **26** (6), 1008 (1992) [Sov. Phys. Semicond. **26**, 565 (1992)].
5. G. N. Violina, E. V. Kalinina, G. F. Kholuyanov, *et al.*, in *Proceedings of the 3rd International Symposium "Silicon Carbide and Related Materials," ISSCRM-2000, Novgorod, 2000*, p. 70.
6. Yu. A. Goldberg, O. V. Konstantinov, O. I. Obolensky, *et al.*, J. Phys.: Condens. Matter **11**, 455 (1999).
7. *Properties of Advanced Semiconductor Materials*, Ed. by M. Levinshtein, S. Rumyantsev, and M. Shur (Wiley, New York, 2000), Vol. 3.
8. C. Persson and U. Lindefelt, J. Appl. Phys. **82** (11), 5496 (1997).
9. R. F. Kazarinov and O. V. Konstantinov, Zh. Éksp. Teor. Fiz. **43** (3), 936 (1961) [Sov. Phys. JETP **13**, 654 (1961)].

Translated by P. Pozdeev

Technical Physics Letters, Vol. 27, No. 9, 2001, pp. 779–780. Translated from Pis'ma v Zhurnal Tekhnicheskoĭ Fiziki, Vol. 27, No. 18, 2001, pp. 50–53.

CO_2 Laser Radiation Confinement in a Composite Material Containing Silver Nanoparticles

O. P. Mikheeva and A. I. Sidorov

Institute of Laser Physics, St. Petersburg, Russia

Received April 19, 2001

Abstract—Experimental data are reported on the optical confinement of a pulsed 10.6 μm laser radiation in a composite comprising a dielectric medium with linear optical properties containing dispersed silver nanoparticles. The energy threshold for the laser radiation confinement at a pulse duration of 2 μs does not exceed 10 μJ/cm^2. © *2001 MAIK "Nauka/Interperiodica".*

Composite optical materials containing dispersed nanoparticles of semiconductors and metals are employed for the high-speed switching of pulsed laser radiation [1–4]. One of the factors determining the large nonlinear permittivity of composites with metal nanoparticles in the visible spectral range is the electric field enhancement at the particles as a result of the plasmon resonance [2, 3]. Below, we present experimental data demonstrating that a dielectric composite with metal nanoparticles may exhibit an increase in the optical nonlinearity in the middle IR range, which leads to a low-threshold confinement of a laser radiation.

The composite was made of a KRS-13 (75% AgBr + 25% AgCl) crystal, which was initially transparent and possessed linear optical properties in the middle IR range. In order to form silver nanoparticles, the material was melted at T = 450°C under illumination with visible light. The melting led to partial decomposition of the components with the liberation of metal silver. The subsequent experiments were performed with polished 1.5-mm-thick plates of the composite free of any antireflection coatings. The estimated volume fraction of silver in the composite did not exceed 10%. The optical transmission coefficient of the sample plates for a continuous low-intensity radiation at 10.6 μm was 75%. The initial material (KRS-13) transmission at the same wavelength was 80%. The radiation source was a pulsed multimode TEA-CO_2 laser operating at 10.6 μm, with a 2 μs pulse width at the base. The measurements were performed with parallel beams. The radiation transmitter through a sample was collected on a photodetector window with the aid of a short-focus KCl lens.

Figure 1 shows the initial portion of the confinement region (a) and the whole curve (b) measured in the incident energy density range of up to E_1 = 70 mJ/cm^2. As is seen from these data, the energy threshold of confinement corresponding to the deviation of the E_2 versus E_1 plot (E_2 is the output energy density) from linear does not exceed 10 μJ/cm^2. For E_1 = 70 mJ/cm^2, the coefficient of attenuation of the incident radiation is 30. The confinement effect is reversible: measurements starting

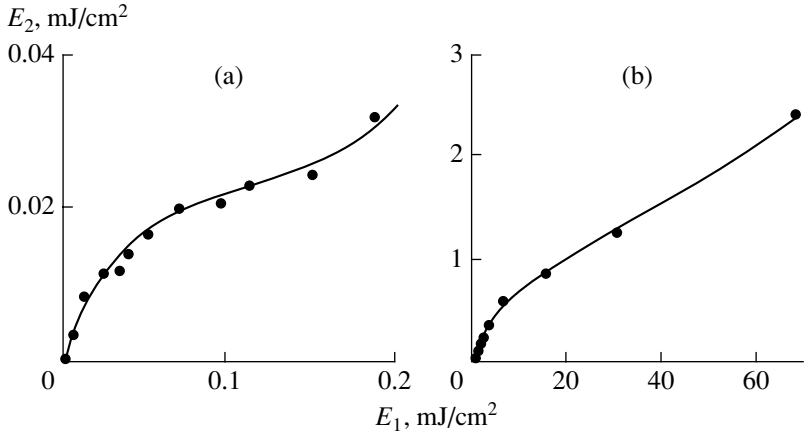

Fig. 1. Plots of the transmitted versus incident radiation energy density (λ = 10.6 μm) for a dielectric composite with silver nanoparticles.

1063-7850/01/2709-0779$21.00 © 2001 MAIK "Nauka/Interperiodica"

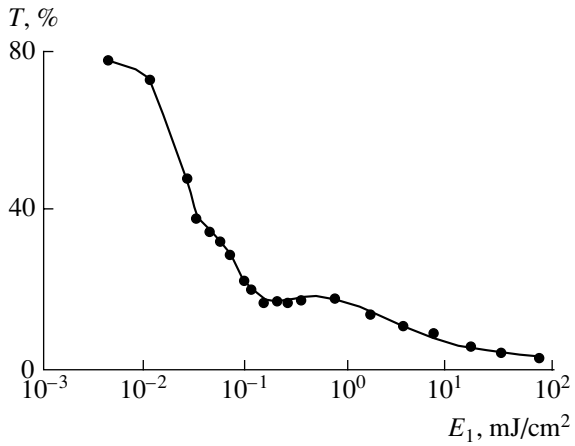

Fig. 2. The plot of optical transmission versus incident laser radiation energy density (λ = 10.6 μm) for a dielectric composite plate.

at the maximum E_1 value gave the same $E_2(E_1)$ curve to within the experimental accuracy.

Figure 2 presents a plot of the composite transmission versus incident radiation energy density. It can be seen that there are two regions of confinement in the range of E_1 values from 0 to 100 mJ/cm^2. The low-threshold region corresponds to E_1 = 10–100 μJ/cm^2, while the region of $E_1 > 1$ mJ/cm^2 is characterized by a high confinement threshold. In the E_1 interval from 0.1 to 1 mJ/cm^2, the transmission coefficient has an almost constant value of about 15%.

The presence of a low-threshold confinement region is indicative of the electric field enhancement at the nanoparticles as a result of the plasmon resonance. However, the region of plasmon resonances for a composite comprising silver nanoparticles dispersed in a linear dielectric medium falls within the visible spectral range [2, 3]. We may suggest that silver nanoparticles in the composite studied possess a complicated fractal structure with voids filled with the dielectric, rather than represent continuous metal grains. The fractal nanoparticles can be characterized by an effective complex permittivity dependent both on the particle shape and on the ratio of metal and dielectric components. The real part of the modulus and the imaginary part of the complex permittivity of such particles are apparently smaller than the analogous values of the complex permittivity of silver. This explains a shift of the plasmon resonance toward longer wavelengths.

The high-threshold confinement region ($E_1 >$ mJ/cm^2) may appear due to the thermal effects related to a temperature variation of the refractive index and absorption coefficient of the dielectric in the vicinity of metal particles. The temperature-induced changes of the optical characteristics of KRS-13 become significant at $T >$ 200°C. However, our estimates showed that the sample temperature variation at E_1 = 1 mJ/cm^2 does not exceed a few dozen degrees, provided that only optical absorption is taken into account. Therefore, we may suggest that a significant role is played by the electric field enhancement in the vicinity of nanoparticles. This effect leads to a considerable heating of a thin dielectric layer surrounding the metal particles.

Thus, we have experimentally established that a composite comprising silver nanoparticles dispersed in a linear dielectric medium exhibits a low-threshold optical nonlinearity leading to the optical confinement effect at a wavelength of 10.6 μm. This effect can be used for the laser radiation control and for the protection of photodetectors radiation damage in the middle IR range.

Acknowledgments. This study was supported by the International Scientific-Technological Center, project no. 1454.

REFERENCES

1. K. M. Leung, Phys. Rev. A **33** (4), 2461 (1986).
2. A. E. Neeves and M. H. Birnboim, J. Opt. Soc. Am. B **6** (4), 787 (1989).
3. D. Stroud and E. van Wood, J. Opt. Soc. Am. B **6** (4), 778 (1989).
4. Ya. S. Bobovich, Opt. Zh. **68** (1), 6 (2001) [J. Opt. Technol. **68**, 3 (2001)].

Translated by P. Pozdeev

Technical Physics Letters, Vol. 27, No. 9, 2001, pp. 781–783. Translated from Pis'ma v Zhurnal Tekhnicheskoĭ Fiziki, Vol. 27, No. 18, 2001, pp. 54–60.

The Fractal Properties of a Geometric Model of the High-Resolution X-ray Diffractor

E. M. Latush and M. I. Mazuritsky*

Faculty of Physics, Rostov State University, Rostov-on-Don, Russia

** e-mail: mazurmik@icomm.ru*

Received April 9, 2001

Abstract—Perfect and mosaic crystals are conventionally used in X-ray monochromators operating in the energy range from several hundred to tens of thousands of electronvolts. The focusing X-ray optics for nonparallel beams employs either cylindrical bent crystals (the methods of Johann [1], Johansson [2], and Cauchois [3]) or crystals with spherical or toroidal [4] bending of the crystallographic planes. Special variants of high-resolution stepped-crystal diffractors [5–8] were developed to study the possibility of high-precision focusing of a monochromatic X-ray radiation. The fractal properties of a geometric model of such a high-resolution stepped-crystal diffractor are considered. © *2001 MAIK "Nauka/Interperiodica".*

The main specific feature of the focusing methods consists in using a diffraction reflection with simultaneous focusing of rays by a large surface of a bent single crystal. Some problems solved by X-ray microanalysis require an instrument possessing a high spectral resolving power in combination with sufficiently large signal intensity. A high resolving power corresponds to small values of the dimensionless parameter $\Delta\lambda/\lambda$ or $\Delta E/E$, where λ is the radiation wavelength and E is the corresponding energy. If θ denotes the angle between an incident ray and the corresponding atomic plane of the crystal, the Bragg law stipulates that the admissible angle variation interval is determined by the relationship $\Delta\theta = \tan\theta\,(\Delta\lambda/\lambda)$. This value depends on several factors, including the mosaic imperfection of a particular crystal, the method used to expand the X-ray radiation into a spectrum, and the size of the reflecting Bragg surface (diffraction zone) of a diffractor crystal. The diffraction reflection zone is the set of points in the crystallographic plane for which the Bragg angle falls within $\theta - \Delta\theta \le \theta \le \theta + \Delta\theta$ for a given wavelength interval $\lambda - \Delta\lambda \le \lambda \le \lambda + \Delta\lambda$. Previously [9], we proposed an algorithm and wrote a program for the computer simulation of the diffraction zones of bent crystal monochromators characterized by various types of the crystallographic plane bending (cylindrical, spherical, toroidal, etc.) employed in the schemes of focusing based on the Rowland circle.

The greater the $\Delta\theta$ value, the wider the diffraction zone and, hence, the larger the aperture and the higher the intensity of the spectra. However, there are many cases requiring both a large intensity and a high spectral resolution (associated with a small reflecting crystal area). The two contradictory conditions can be only satisfied in a system employing several crystals.

The principles of design of the stepped-crystal diffractors employing a separate bent crystal in each step were developed in [5–7]. The theoretical scheme of a new high-brightness stepped-crystal X-ray diffractor with controlled spectral resolution was considered in [8]. It was demonstrated that a high resolution could be provided at a constant angular width ($\Delta\varphi$ = const) of each crystal.

The results of testing a prototype of the high-brightness stepped-crystal X-ray diffractor for electron-probe microanalysis (EPMA) employing four cylindrically bent (002) mica crystals were reported in [10, 11]. The tests conducted in the spectrometer channel of an EPMA system of the CAMEBAX-micro type using AgLα(3) radiation showed that intensity of the spectrum measured with the new diffractor increased 3.3 times as compared to the spectrum obtained with a single bent crystal (for the same resolution parameter of 10^{-3}).

The reflecting surface of the stepped-crystal X-ray diffractor is composed of concave cylindrical fragments having the same height and a common vertical axis. Mounted on each step (glued or fixed so as to form the optical contact) is a bent crystal monochromator. Figure 1a schematically shows a median section of the diffractor by the plane of the focusing circle with the center at the point O'.

The focusing circumference occurring in the horizontal plane passes through the point S at which the radiation source is located, the diffractor apex A_2 (middle of the central step), and the detector D. The section of each step by the focusing circle plane is an arc centered at the point O. The central step has a radius equal to the doubled radius of the focusing circle. The radii of subsequent steps gradually decrease with the distance from the central step.

1063-7850/01/2709-0781$21.00

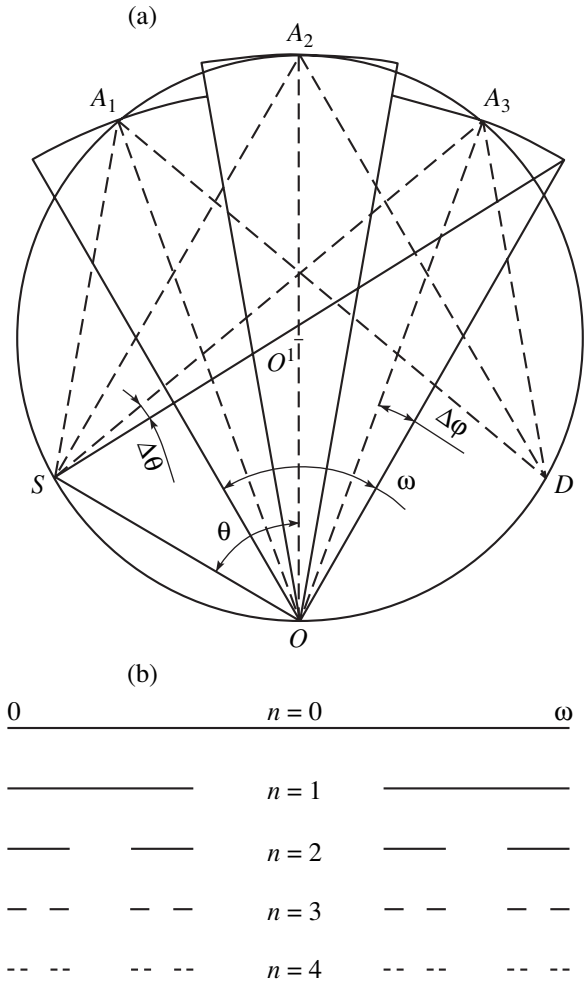

Fig. 1. Geometric model of the stepped-crystal diffractor: (a) optical scheme of the diffractor and spectral expansion of the X-ray radiation (points *O*' and *O* are centers of the focusing circle and step curvature, respectively; *S* and *D* are positions of the radiation source and its image or detector); (b) schematic diagram illustrating generation of the Cantor triad set (proceeding from [0, ω] seeding segment, the generator rejects the middle on each tripling step) for the first four generations.

In Fig. 1a, angle ω is the total angular width of the diffractor relative to point *O*, $\alpha_i = \angle A_2OA_i$ are the angular positions of each step, and $R_i = OA_i$ are the corresponding radii of curvature. The radiation is incident onto each step at an angle θ relative to the tangent. One of the models proposed in our previous paper [8] employs steps of equal angular width. In such a case, $2\Delta\varphi = \text{const}(i)$ and the angle ω with the apex at point *O* is divided into 2*N* equal parts, Δφ being the halfwidth of each step (Fig. 1a). Apparently, in this scheme

$$\alpha_i = \frac{\omega(2i - N - 1)}{2N}, \quad R_i = R_0\cos\alpha_i, \qquad i = 1, 2\ldots N. \tag{1}$$

Let us consider the stepped crystal surface formation by sequentially tripling the number of steps. Here, we digress from considering a real diffractor and consider schematically a geometric model analogous to that used in [12] to create a Cantor fractal point set in the unit segment [0, 1].

The seeding element used to generate the initial set (zero generation) is an arc with a width ω situated in the plane of the focal circle centered at point *O*. The process of step multiplication (forming steps similar to the initial element) consists in applying a certain procedure, representing a generating element (generator) of the set. In our case, this generator divides the arc in the first step into three equal angular parts (so as to produce three arcs centered at *O*) and rejects the middle part. Then the generator is applied to each of the two remaining angular intervals and so on. Upon accomplishing an infinite number of generation steps, the resulting set represents a system of fine nonintersecting angular segments called the Cantor dust (see [13]).

In our case, the linear segment [0, 1] is replaced by the angular segment [0, ω] representing the set K_0 (Fig. 1b, $n = 0$). Dividing this segment into three equal parts and rejecting the middle (ω/3, 2ω/3), we obtain the set K_1 comprising the pair of segments [0, ω/3] and [2ω/3, ω] (Fig. 1b, $n = 1$) and so on. Continuing this process, we obtain a decreasing sequence of embedded sets K_n, each set K_n containing 2^n segments of equal lengths $(\omega/3)^n$. According to Hausdorff (see [12, 13]), the fractal dimension of this Cantor triad set is $D = \ln 2/\ln 3 = 0.630929\ldots$

In a real X-ray spectrometer, the radiation source is situated at point *S*, which may only hypothetically (for $\theta = 90°$) coincide with point *O*. A relationship between the quantities Δθ and Δφ is given by the expression

$$\Delta\theta \approx \tan\theta/(\tan\theta + \tan\alpha)\Delta\varphi. \tag{2}$$

It is seen that the angular size of steps viewed from point *S* is not constant, in which sense the geometry of a stepped-crystal diffractor is subject to variation. Using a scheme analogous to that for point *O* (Fig. 1b), we determined the Hausdorff fractal dimension *D* for point *S*. This was performed with the aid of a special computer program for an IBM PC, sequentially dividing the segment [0, ω] into 3, 9, 27, … equal parts (tripling at each step) and rejecting the middle. In each step, the $\Delta\varphi_i$ values were recalculated into $\Delta\theta_i$ by formula (2). According to [12], the value of the *d*-measure of the set of angular segments in the *n*th generation is given by the expression

$$M_d = \sum_{\Delta\theta_i \in K_n} \Delta\theta_i^d \xrightarrow[2^n \to \infty]{} \begin{cases} 0, & d > D, \\ \infty, & d < D. \end{cases} \tag{3}$$

The critical dimension $d = D$ obtained in the limit of infinitely increasing number of angular segments ($2^n \longrightarrow \infty$) is the fractal dimension. This is the exponent *d*, such that the sum in expression (3) becomes

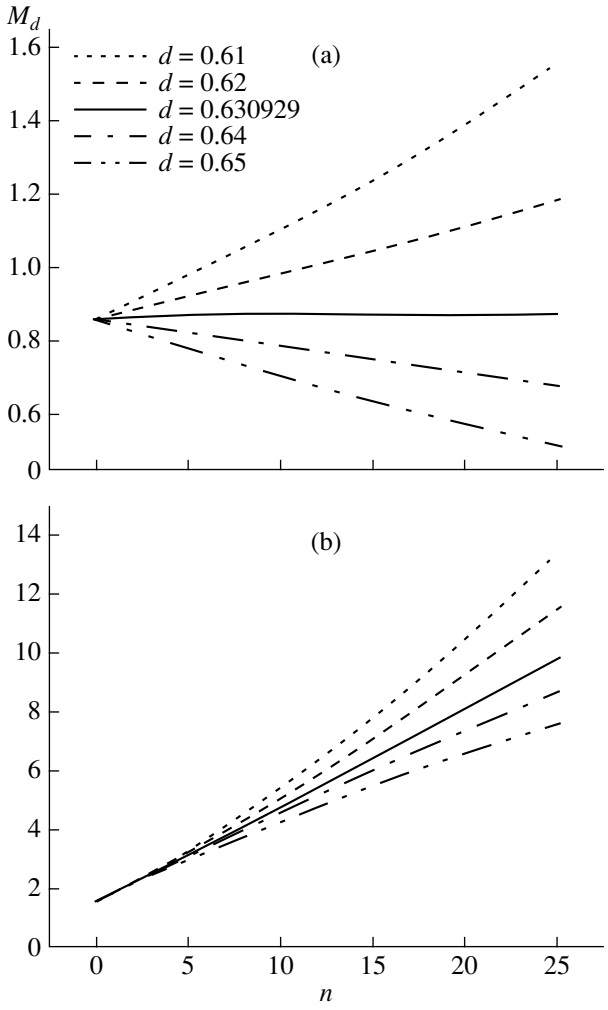

Fig. 2. Plots of the measure M_d of the set of angular segments versus generation number n for various d values (nth generation contains 2^n segments) and the diffractor angular width (a) $\omega < 2\theta$ and (b) $\omega \approx 2\theta$.

finite (albeit not tending to zero) despite the infinite increase in the number of the diffractor steps. For a diffractor with an angular width $\omega < 2\theta$ (Fig. 2a), the fractal dimension is still $D = 0.630929\ldots$; that is, it remains the same as that in the model of diffractor relative to point O. This is illustrated by the plots in Fig. 2a, which tend to zero for larger d and grow to infinity for smaller d.

However, the fractal properties of the geometric model completely disappear if the point S (radiation source) coincides with the left boundary of the diffractor (i.e., at $\theta \approx \omega/2$). For this case, the numerical modeling showed that the plots corresponding to any d (Fig. 2b) exhibit infinite growth. In other words, no value $d = D$ exists in the limit as $2^n \longrightarrow \infty$ such that the M_d value would be finite. This result is simply explained by that the angular size of steps close to point S increases despite a decrease in the arc length with a growing number of steps n.

REFERENCES

1. H. H. Johann, Z. Phys. **69**, 185 (1931).
2. T. Johansson, Z. Phys. **82**, 507 (1933).
3. Y. Cauchois, J. Phys. Radium **3**, 320 (1932).
4. C. Bonnelle and C. Mande, *Advances in X-ray Spectroscopy* (Pergamon, Oxford, 1982).
5. D. B. Wittry and S. J. Sun, J. Appl. Phys. **69** (7), 3886 (1991).
6. A. Marcelli, A. V. Soldatov, and M. I. Mazuritsky, European Patent No. 97830282.6-2208 (1997).
7. A. Marcelli, M. I. Mazuritsky, and A. V. Soldatov, Proc. SPIE **3448**, 210 (1998).
8. M. I. Mazuritsky, E. M. Latush, A. V. Soldatov, *et al.*, Pis'ma Zh. Tekh. Fiz. **26** (12), 15 (2000) [Tech. Phys. Lett. **26**, 502 (2000)].
9. M. I. Mazuritsky, A. V. Soldatov, E. M. Latush, *et al.*, Pis'ma Zh. Tekh. Fiz. **25** (19), 11 (1999) [Tech. Phys. Lett. **25**, 763 (1999)].
10. A. Marcelli, M. I. Mazuritsky, A. V. Soldatov, and E. M. Latush, in *Proceedings of the Second Workshop, Weimar, Germany, 1999*, p. 74.
11. M. I. Mazuritsky, A. V. Soldatov, V. L. Lyashenko, *et al.*, Pis'ma Zh. Tekh. Fiz. **27** (1), 24 (2001) [Tech. Phys. Lett. **27**, 11 (2001)].
12. J. Feder, *Fractals* (Plenum, New York, 1988; Mir, Moscow, 1991).
13. R. N. Kronover, *Fractals and Chaos in Dynamic Systems* (Postmarket, Moscow, 2000).

Translated by P. Pozdeev

Technical Physics Letters, Vol. 27, No. 9, 2001, pp. 784–785. Translated from Pis'ma v Zhurnal Tekhnicheskoĭ Fiziki, Vol. 27, No. 18, 2001, pp. 61–64.

A Stochastic Equation for the Evolution of Channeled Particles

V. P. Koshcheev

Surgut State University, Surgut, Russia

e-mail: koscheev@surgu.wsnet.ru

Received January 29, 2001

Abstract—A stochastic equation for the evolution of the transverse energy of high-energy charged particles moving in planar and axial channels in a crystal is derived using the condition of nonconservation of the adiabatic invariant. © *2001 MAIK "Nauka/Interperiodica".*

A stochastic equation for the evolution of the transverse energy of channeled high-energy charged particles is necessary for constructing the kinetic equation of the Fokker–Planck type in the space of transverse energies without recourse to the Lindhard hypothesis of attaining the statistical equilibrium [1]. Derivation of the kinetic Fokker–Planck equation based on the kinetic equation for weakly disturbed quantum systems is not quite satisfactory [2] because the initial equation constructed within the framework of the perturbation theory restricts the domain of applicability of this Fokker–Planck equation to the condition of slow variation of an adiabatic invariant represented by the transverse energy of channeled particles.

The primary factor determining the regular and chaotic motion of channeled particles in a crystal is the electric potential of the crystal, which is the sum of the Coulomb potentials of atomic nuclei occupying the crystal lattice sites and the Coulomb potentials of electrons in the atomic shells

$$U(r) = \sum_n \left(\frac{Ze^2}{|\mathbf{r} - \mathbf{r}_n|} - \sum_{j=1}^{Z} \frac{e^2}{|\mathbf{r} - \mathbf{r}_{nj}|} \right), \quad (1)$$

where Ze is the charge of the atomic nucleus, $\mathbf{r}_n = \mathbf{r}_{n0} + \delta\mathbf{r}_n$ ($\delta\mathbf{r}_n$ is the vector determining the position of the nth nucleus displaced from the lattice site due to thermal oscillations), $\mathbf{r}_{nj} = \mathbf{r}_{n0} + \delta\mathbf{r}_n + \delta\mathbf{r}_{nj}$ ($\delta\mathbf{r}_{nj}$ is the vector determining the position of the jth electron relative to the nth atomic nucleus), and $\mathbf{r}_{n0}$ determines the position of the nth crystal lattice site.

Averaging over the independent thermal oscillations of atoms in the crystal is performed with the aid of the Gauss distribution function. Averaging over the quantum fluctuations of the positions of atomic electrons is carried out using the method [3] employed by Bethe for calculating the atomic form factor. These averaging procedures, conducted with respect to the coordinates of all nuclei and all electrons, are denoted by symbols $\langle \ldots \rangle_T$ and $\langle \ldots \rangle_e$, respectively. The motion of a single high-energy charged particle in the transverse direction is described by the classical equation of motion

$$m\frac{d^2\mathbf{r}_\perp}{dr^2} = \mathbf{F}_\perp, \quad (2)$$

where $\mathbf{r}_\perp = (x, y)$ is the transverse coordinate, $\mathbf{F}_\perp = (F_x, F_y)$ is the transverse force, $F_x = -\partial U(r)/\partial x$, $U(r) = U(x, y, z)$ is the potential energy of the channeled particle, $m = \gamma m_0$, $\gamma = (1 - \beta^2)^{-1/2}$ is the Lorentz factor, $\beta = v/c$, c is the velocity of light, v is the velocity of the charged particle along OZ axis, and m_0 is the rest mass.

The electric potential can be represented as a sum of the mean value and the potential fluctuations

$$U(r) = \bar{U} + \delta U_z(r) + \delta U(r), \quad (3)$$

where $\bar{U}$ is the continuous potential of an axial ($\bar{U} = \bar{U}(x, y)$) or a plane-parallel ($\bar{U} = \bar{U}(x)$) channel in the crystal, averaged over the thermal oscillations of atoms; $\delta U_z(r) = \langle U \rangle_{e,T} - \bar{U}$ is the continuous potential correction related to the discrete arrangement of atoms on the axis or in the plane; and $\delta U(r) = U(r) - \langle U \rangle_{e,T}$ is the potential fluctuation caused by thermal oscillations of the atomic nuclei and quantum fluctuations of the positions of atomic electrons.

Let us first consider the case of a plane-parallel channel. The transverse energy of a channeled particle is

$$\varepsilon = \frac{m\dot{x}^2}{2} + \bar{U}(x). \quad (4)$$

The rate of variation of the transverse energy of the channeled particle is

$$\frac{d\varepsilon}{dt} = \sqrt{\frac{2}{m}[\varepsilon - \bar{U}(x)]}\,\delta f, \quad (5)$$

where $\delta f = -\dfrac{\partial \delta U}{\partial x}$ is the transverse force fluctuation.

The adiabatic invariant can be written as [4]

$$I = \frac{1}{\pi}\int_{X_1(\varepsilon)}^{X_2(\varepsilon)} \sqrt{2m[\varepsilon - \bar{U}(x)]}\,dx, \quad (6)$$

where $X_{1,2}$ are the reversal points of the classical trajectory of a channeled particles, which can be determined from the equation $\bar{U}(X_{1,2}) = \varepsilon$.

The period of oscillations for the particles moving in a plane-parallel crystal channel is defined by the relationship

$$\frac{dI}{d\varepsilon} = \frac{T(\varepsilon)}{2\pi}. \quad (7)$$

If the adiabatic invariant depends only on the transverse energy, $I = I(\varepsilon)$, and this energy varies with time, $\varepsilon = \varepsilon(t)$, the adiabatic invariant is also not conserved in time: $I = I[\varepsilon(t)]$.

The rate of variation of the adiabatic invariant with time can be determined as follows:

$$\frac{dI}{dt} = \frac{dI}{d\varepsilon}\frac{d\varepsilon}{dt}, \quad (8)$$

$$\frac{dI}{dt} = \frac{1}{2\pi}\int_{X_1(\varepsilon)}^{X_2(\varepsilon)} \sqrt{\frac{2m}{\varepsilon - \bar{U}(x)}}\frac{d\varepsilon}{dt}\,dx. \quad (9)$$

Equating the right-hand parts of Eqs. (8) and (9) and using relationships (5) and (7), we obtain an equation describing evolution of the transverse energy of channeled particles,

$$\frac{d\varepsilon}{dt} = \frac{2}{T(\varepsilon)}\int_{X_1(\varepsilon)}^{X_2(\varepsilon)} \delta f\,dx, \quad (10)$$

which can be rewritten as

$$\frac{d\varepsilon}{dt} = -\frac{2}{T(\varepsilon)}\{\delta U[X_2(\varepsilon), t] - \delta U[X_1(\varepsilon), t]\}. \quad (11)$$

As can be seen, the transverse energy of channeled particles is not conserved only when the right-hand part of the evolution equation is a source of fluctuations. By the same token, we construct a stochastic equation of evolution of the transverse equation of high-energy charged particles in the axial channels:

$$\frac{d\varepsilon}{dt} = -\frac{1}{S(\varepsilon)}\int\int_{\varepsilon = \bar{U}(x,y)} \frac{d\delta U}{dt}\,dx\,dy, \quad (12)$$

where

$$S(\varepsilon) = \int\int_{\varepsilon = \bar{U}(x,y)} dx\,dy.$$

In Eq. (12), the averaging is performed over the region accessible for the channeled particle possessing the transverse energy ε. Averaging of this type is used within the framework of the Lindhard hypothesis of attaining the statistical equilibrium [1]. Proceeding from the stochastic equations (10) or (12), one may readily construct an equation of the Fokker–Planck type (see, e.g., [5] and references therein).

REFERENCES

1. J. Lindhard, Usp. Fiz. Nauk **99** (2), 249 (1969).
2. V. A. Bazylev and N. K. Zhivago, *Radiation from Fast Particles in Matter and External Fields* (Nauka, Moscow, 1987).
3. H. A. Bethe, *Intermediate Quantum Mechanics* (W. A. Benjamin, New York, 1964; Mir, Moscow, 1965).
4. L. D. Landau and E. M. Lifshitz, *Course of Theoretical Physics*, Vol. 1: *Mechanics* (Nauka, Moscow, 1973; Pergamon, New York, 1988).
5. S. M. Rytov, *Introduction to Statistical Radiophysics* (Nauka, Moscow, 1976), Part 1.

Translated by P. Pozdeev

Technical Physics Letters, Vol. 27, No. 9, 2001, pp. 786–788. Translated from Pis'ma v Zhurnal Tekhnicheskoĭ Fiziki, Vol. 27, No. 18, 2001, pp. 65–70.

Slowly Relaxing Charge in Lead Borosilicate Glass Passive Coatings Studied by Isothermal Capacitance Relaxation

P. B. Parchinskii, S. I. Vlasov, and A. A. Nasirov

National University of Uzbekistan, Tashkent, Uzbekistan

e-mail: pavel@phys.silk.org

Received April 12, 2001

Abstract—The effective surface charge density in passive lead borosilicate glass coatings on a semiconductor surface was determined by the isothermal capacitance relaxation measurements. It was found that an increase in the temperature of coating formation is accompanied by increase in the effective surface charge density. This relationship is explained by the growth in concentration of the charge trapping centers with increasing content of a crystalline phase in the bulk of glass. *© 2001 MAIK "Nauka/Interperiodica".*

Low-melting lead borosilicate glasses are widely used in semiconductor microelectronics for obtaining passive and insulating layers [1, 2], which accounts for the interest in investigating electrical characteristics of these materials. An important parameter of such passive coatings is the amount of the slowly relaxing (mobile) charge present in the bulk of glass [1]. Previously [3], we established that the main factor responsible for the appearance of this slowly relaxing charge in passive lead borosilicate glass coatings on semiconductors is the charge carrier transfer between a semiconductor and the trapping centers existing in the bulk of glass. The extent of influence of the charge density in the dielectric on the parameters of semiconductor devices is usually characterized by the value of effective trapped surface charge density Q_{ts} [4].

In cases when the presence of a slowly relaxing charge is related to the recharge of trapping centers in the bulk of the dielectric, the Q_{ts} value can be determines as

$$Q_{ts} = \frac{1}{d} q \int_0^d N_{ts}(x) x dx, \quad (1)$$

where d is the dielectric layer thickness, $N_{ts}(x)$ is the distribution of the concentration of charge trapping centers in depth of the dielectric, q is the elementary charge, and $x = d$ is the coordinate of the semiconductor–dielectric interface. A change in the potential ψ_s at the semiconductor–dielectric interface may affect the charged state of the trapping centers in the bulk. Therefore, it was also of interest to study the differential density of the effective surface charge $D_{ts} = dQ_{ts}/d\psi_s$, which determines a change in the effective surface charge density in response to the surface potential variation. The D_{ts} value depends on the energy spectrum of the charge trapping centers in the dielectric.

In practice, the experimental data are usually described in terms of the Q_{ts} and D_{ts} values as functions of E, the energy of the Fermi level relative to the conduction band bottom E_c at the semiconductor–dielectric interface for a given ψ_s. The E value can be expressed as

$$E = E_c - F - q\psi_s, \quad (2)$$

where F is the Fermi level energy in a quasi-neutral volume of the semiconductor. Below, we will present the $Q_{ts}(E)$ and $D_{ts}(E)$ curves measured for the passive lead borosilicate glass coatings by the method of isothermal capacitance relaxation after charge carrier injection into the bulk of glass (charge pumping technique) [4, 5].

The passive glass coatings were deposited onto n-Si(111) substrates with a resistivity of $\rho = 60$–$80\ \Omega$ cm. The glass composition and the coating deposition process were analogous to those described in [6]. Taking into account that the electrical properties of passive lead borosilicate glass coatings depend on the temperature regime of passivation [6], the samples were divided into two groups. In group 1, the glass was fused at 680°C, while in group 2, the treatment temperature was increased to 700°C. The isothermal capacitance relaxation measurements were conducted on sample heterostructures of the metal–dielectric–semiconductor type with a control metal electrode area of 0.01 cm^2.

The isothermal capacitance relaxation measurements were performed at room temperature in the dark using the bridge compensation technique. The charge trapping centers in the glass were recharged by applying a strong-enrichment voltage pulse V_1 to the control

1063-7850/01/2709-0786$21.00

electrode of a sample heterostructure initially occurring in an equilibrium state corresponding to a certain base voltage V_0. After termination of the enrichment voltage pulse, the bridge unbalance signal that was proportional to the amount of charge Q_{ts} captured by the trapping centers was measured. By changing the base voltage V_0, it was possible to study the dependence of Q_{ts} and D_{ts} on ψ_s and E. The relationship between V_0 and ψ_s was determined as described in [7].

Figures 1 and 2 show the $Q_{ts}(E)$ and $D_{ts}(E)$ curves measured as described above. It is seen from Fig. 1 that Q_{ts} monotonically increases with E in the samples of both groups, which is explained by increasing energy interval featuring the carrier exchange between semiconductor and glass [4, 5]. Note also that the Q_{ts} and D_{ts} values in the samples of group 2 are almost ten times greater than the analogous values in group 1. The $D_{ts}(E)$ curves of the heterostructure belonging to both groups exhibit minima at E = 0.45–0.55 eV, where D_{ts} = (1.1–1.4) × 10^{-9} C/(cm^2 eV) in group 1 and D_{ts} = (5.5–7) × 10^{-9} C/(cm^2 eV) in group 2. Neither of the curves exhibit local maxima at some E values.

According to [8], such U-shaped spectra of charge trapping centers free of local maxima are characteristic of the localized states in the bandgap of an amorphous dielectric. However, using this assumption about the nature of the carrier trapping centers in lead borosilicate glasses, it is difficult to explain dependence of the Q_{ts} and D_{ts} values on the temperature of the passive glass coating formation. On the other hand, it is known that dangling bonds occurring at the boundaries of phase inhomogeneities in the bulk of glass are also characterized by a continuous spectrum of energy states in the bandgap [9]. Such inhomogeneities may represent, for example, the inclusions of a crystalline phase formed in the glass matrix in the course of the passive coating formation [6].

Data of the electron microscopy and X-ray diffraction measurements showed that the content of a crystalline phase in lead borosilicate glasses increased when the fusion temperature was changed from 680 to 700°C. The related growth in the area of interphase boundaries leads to an increase in the number of dangling bonds localized at these interfaces, which can serve as the charge trapping centers. This must be accompanied by an increase in the amount of slowly relaxing charge accumulated in the bulk of glass, which can explain the observed correlation between Q_{ts} and D_{ts}, on the one hand, and the temperature of fusion of the passive glass coatings, on the other hand.

Thus, the results of the isothermal capacitance relaxation measurements yielded the $Q_{ts}(E)$ and $D_{ts}(E)$ curves for the passive lead borosilicate glass coatings on a semiconductor surface. An analysis of these experimental data suggested that the appearance of charge carrier trapping centers in these coatings is related to the formation of crystalline phase inclusions in the amorphous glass matrix. The observed growth in Q_{ts} and D_{ts} values, accompanying the increase in the temperature of the passive glass coating formation from 680 to 700°C, is related to the increasing content of the crystalline phase in the glass.

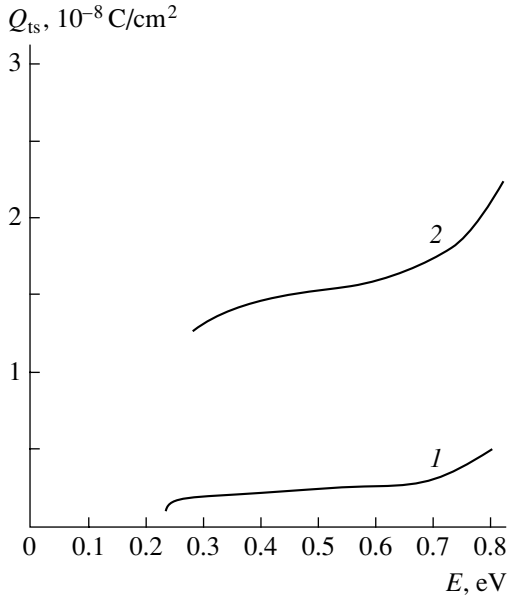

Fig. 1. Plots of the effective surface charge density Q_{ts} versus the Fermi level position E (relative to the conduction band bottom at the semiconductor–glass interface) for the samples of group 1 and 2 (curves *1* and *2*, respectively).

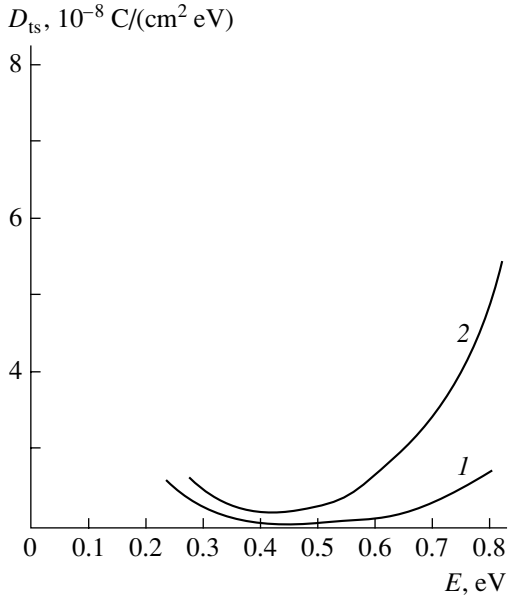

Fig. 2. Plots of the differential effective surface charge density D_{ts} versus the Fermi level position E (relative to the conduction band bottom at the semiconductor–glass interface) for the samples of group 1 and 2 (curves *1* and *2*, respectively).

REFERENCES

1. V. F. Korzo and V. N. Chernyaev, *Dielectric Films in Integrated Microelectronics* (Énergiya, Moscow, 1977).
2. I. G. Pichugin and Yu. M. Tairov, *Technology of Semiconductor Devices* (Vysshaya Shkola, Moscow, 1984).
3. S. I. Vlasov, P. B. Parchinskiĭ, A. A. Nasirov, *et al.*, Zh. Tekh. Fiz. **69** (8), 141 (1999) [Tech. Phys. **44**, 998 (1999)].
4. L. S. Berman, Fiz. Tekh. Poluprovodn. (St. Petersburg) **31** (1), 78 (1997) [Semiconductors **31**, 63 (1997)].
5. J. E. Chung and R. S. Muller, Solid-State Electron. **12** (10), 867 (1989).
6. P. B. Parchinskiĭ, S. I. Vlasov, A. A. Nasirov, *et al.*, Mikroélektronika **26** (1), 62 (1997).
7. S. M. Sze, *Physics of Semiconductors Devices* (Wiley, New York, 1981; Mir, Moscow, 1984), Vol. 1.
8. N. F. Mott and E. A. Davis, *Electronic Processes in Non-Crystalline Materials* (Clarendon Press, Oxford, 1971; Mir, Moscow, 1974).
9. T. Bechshtedt and R. Enderlein, *Semiconductor Surfaces and Interfaces. Their Atomic and Electronic Structures* (Academie-Verlag, Berlin, 1988; Mir, Moscow, 1990).

Translated by P. Pozdeev

Technical Physics Letters, Vol. 27, No. 9, 2001, pp. 789–791. Translated from Pis'ma v Zhurnal Tekhnicheskoĭ Fiziki, Vol. 27, No. 18, 2001, pp. 71–77.

Radiation-Stimulated Erosion of Field Electron Emitters

T. I. Mazilova, I. M. Mikhaĭlovskiĭ, and V. A. Ksenofontov

Kharkov Physicotechnical Institute, National Scientific Center, Kharkov, Ukraine

Received April 10, 2001

Abstract—The features of erosion of the surface of point field electron emitters bombarded by helium ions were studied. An analysis of the ion-bombardment-induced atomic-scale surface roughness showed evidence of a nondynamic character of the surface atom displacement for the primary ion energies below a threshold for the stable Frenkel pair formation and cathode sputtering. A quasi-static mechanism of the surface erosion is considered, according to which the process is related to the displacement of metal atoms into low-coordinated positions upon evolution of the energy of formation of interstitial helium atoms. © *2001 MAIK "Nauka/Interperiodica".*

Considerable interest in the field electron emitters (cold cathodes) is related to their possible application as active elements in various electronic devices. The discovery of explosive (blow-up) emission, which is now widely employed for the generation of high-current electron beams, inspired the investigations of processes occurring on the surface of cold cathodes operating at high current densities [1].

In recent years, development of the scanning tunneling microscopy, new types of field electron emitters for nanoelectronic devices [2–5], and coherent field electron sources [6] has markedly stimulated the research in this field. Application of the field electron emitters in electron-beam and microelectronic devices is significantly limited by a relatively low stability of these elements with respect to ion bombardment. The ion bombardment unavoidably accompanies the field emission process as a result of the electron impact ionization of residual gases, predominantly inert gases, penetrating into vacuum chambers from the atmosphere, the more so that these gases are poorly evacuated by standard ultra- high vacuum pumps.

The problems pertaining to the radiation stability of cold cathodes are usually treated in terms of the cumulative cathode sputtering mechanism, developed in the early works devoted to the field electron emission from point cathodes [7, 8], and the notions about surface erosion proceeding as a result of the radiation-enhanced surface self-diffusion [9, 10]. To the present, it is reliably established that evolution of the atomic topography of a cold cathode, characterized by a submicron radius of curvature of the emitting surface, in the course of ion bombardment is determined primarily by the radiation-enhanced surface migration of atoms. However, the mechanism of this phenomenon is still insufficiently clear. We have used the field ion (FIM) and field electron microscopy (FEM) techniques to study interaction of the low-energy helium atoms with an atomically smooth tungsten emitter surface.

The study was carried out in a two-chamber field emission microscope in which the samples and ultrahigh vacuum cryosorption pumps were cooled with liquid hydrogen. The working voltage could be varied from 1.5 to 25 kV in the FIM mode and from 0.1 to 2.5 kV in the FEM mode. The residual gas pressure in the inner vacuum chamber was maintained within 10^{-7}–10^{-6} Pa and the imaging gas (helium) pressure was $(2–4) \times 10^{-3}$ Pa. The point emitter samples were fabricated by electrochemical etching from high-purity tungsten (99.98% W). The sample temperature in the course of ion bombardment was maintained within 80–300 K. The emitting surface of a cold cathode was formed by evaporating at 80 K in the electric field of positive polarity at a field strength of 5.8×10^{10} V/m.

The helium ion irradiation parameters in the FEM mode at a field strength of $E = (2–4) \times 10^9$ V/m were determined as described in [9, 11]. The helium ion energy distribution was close to Maxwellian, with the mean ion energy $\langle W \rangle$ approximately equal to er_0E (e is the electron charge and r_0 is the curvature radius of the hemispherical emitter point tip). In our experiments, the mean ion energy was varied within 25–500 eV. The maximum energy of bombarding ions W_{max} was four to five times as large as the mean value $\langle W \rangle$. After irradiation of the sample emitter, the applied voltage polarity was reversed and the surface erosion was studied in the FIM mode.

Figure 1 shows typical FIM images of a point cold emitter with a surface curvature radius at the tip $r_0 = 6$ nm, which were obtained both before and after irradiation with helium ions at a mean energy of 30 eV to a total fluence of 4.2×10^{14} cm^{-2} at 100 K. The maximum energy of helium ions in this experiment was 150 eV. The mean energy $\langle w_a \rangle$ transferred by projectiles to the surface tungsten atoms was approximately 1.2 eV. The irradiation resulted in disturbance of the regular arrangement of metal atoms in the surface layer. The

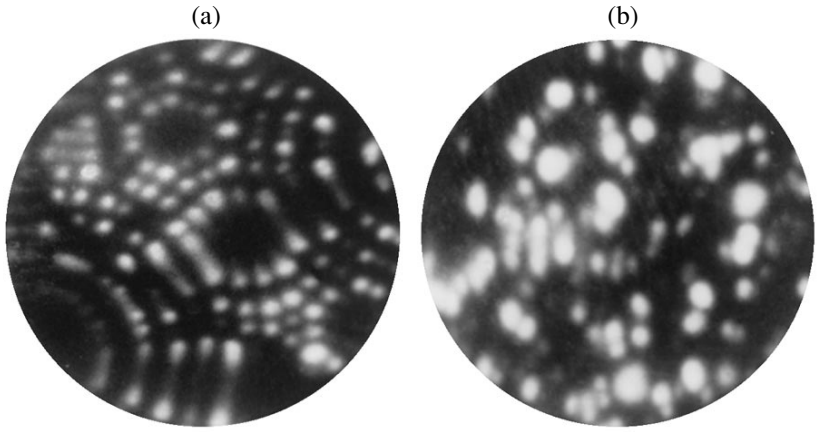

Fig. 1. FIM images of a low-voltage field electron point emitter (a) before and (b) after irradiation with helium ions to a total fluence of ~10^{13} ion/cm^2.

sample surface exhibited randomly distributed centers of increased brightness, most of which represented the images of individual atoms. The local increase in brightness is explained by the fact that these atoms were displaced as a result of the ion bombardment from their initial sites to positions with reduced values of the surface coordination number, which are characterized by a relatively high local electric field strength. The field evaporation voltage for such displaced atoms is 8–12% lower than the threshold value for stepped close-packed planes {211} and {110}. In our experiments, the $\langle W \rangle$ and W_{max} values were significantly lower than the threshold energy for the cathode sputtering and the formation of stable Frenkel pairs of point defects (450 eV) [12]. Therefore, the description of the surface erosion under the action of low-energy ion bombardment cannot be based on the known dynamic mechanisms of the atomic-scale surface roughness development as a result of the cathode sputtering [7, 8] or the radiation-induced interstitial atoms emerging at the surface [13].

Figure 2 shows a plot of the surface density of bright centers N (normalized to the ion fluence N_i) versus the mean helium ion energy. The surface density of bright centers gradually increases with the ion energy, showing no features that could be expected if any dynamic mechanism of the atomic-scale surface roughness formation were in operation. In particular, there is no jump in the surface density of displaced atoms in the vicinity of $\langle W \rangle$ = 450 eV corresponding to the threshold of defect formation in the bulk (and subsurface) layers. Another important point is that the surface erosion does not vanish when the ion energy decreases to $\langle W \rangle$ = 30 eV, which corresponds to a mean energy of $\langle w_a \rangle$ = 1.2 eV transferred to tungsten atoms. Thus, the radiation stability of nanoemitters operating under conditions of small (subthreshold) mean energies of bombarding atoms cannot be described within the framework of any collisional mechanism of the radiation-enhanced surface self-diffusion.

The dynamic effects may give certain contribution to the formation of a surface microrelief by displacing surface atoms into energetically close positions. However, the fact that atoms kept appearing on the surface after termination of the ion bombardment confirmed the assumption concerning a collisionless mechanism of the formation of atomic-scale roughness on the surface of ion-bombarded low-voltage field electron emitters.

During the low-energy ion bombardment of nanoemitters under conditions excluding the dynamic channels of erosion (such as the cathode sputtering, displacement of surface atoms to low-coordinated positions, and radiation-induced Frenkel pair formation followed by diffusion emergence of the mobile interstitial atoms at the surface), a significant role may belong to relaxation processes in the subsurface layers satu-

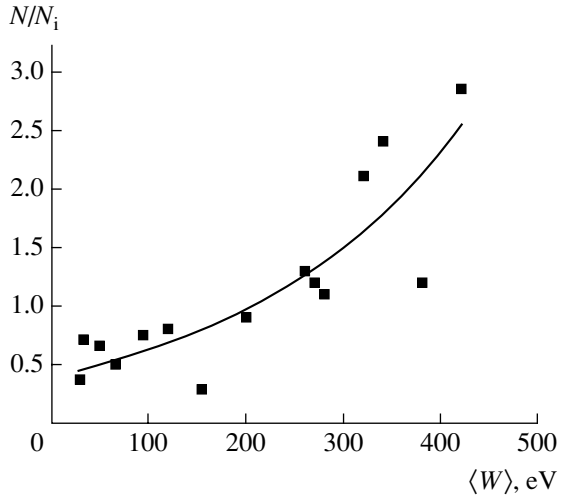

Fig. 2. A plot of the surface density of bright centers N (normalized to the ion fluence N_i) versus the mean helium ion energy.

rated with implanted helium atoms. The presence of helium atoms in the subsurface layers of targets was detected at 300 K by the mass spectra taken with the aid of a two-pulse atomic probe–field ion microscope (AP–FIM) instrument [14]. The AP–FIM operation in the two-pulse regime virtually excludes the probability of detecting helium atoms unavoidable present in the residual atmosphere. The possibility of helium absorption in the subsurface layers of metals is usually related to the trapping of helium atoms by vacancies in these layers. However, as noted above, the energy of helium ions in most of the experiments reported here was significantly below the threshold of defect formation. Thus, the AP–FIM data confirmed the assumption that helium atoms are absorbed in the subsurface layers of defect-free nanocrystals.

Despite the fact that the role of helium in the radiation damage of metals was repeatedly studied [12, 15], the mechanism of interaction of individual helium atoms with the surface layers of metals is still unclear. It is known that the interaction of helium and metal atoms has a repulsive character and the penetration of helium into a metal crystal lattice leads to local displacements of the surrounding matrix atoms. Calculated values of the energy of formation of an interstitial helium atom depend on its position in the lattice and may vary in tungsten within 5.5–7.4 eV [12], which significantly exceeds the maximum energies necessary for displacing the surface tungsten atoms into low-coordinated positions.

Thus, under conditions when the surface erosion by low-energy ion bombardment cannot be described by any dynamic mechanism of the atomic-scale surface roughness formation, the displacements of surface metal atoms as a result of evolution of the energy of formation of interstitial helium atoms may significantly contribute to the emitter erosion. The appearance of the atomic-scale surface roughness as a result of the displacement of surface atoms into low-coordinated positions in the course of ion bombardment, which was observed in our experiments, must lead to an increased surface mobility. This factor can be considered as a radiation-induced decrease in the surface self-diffusion energy that has to be taken into account in a phenomenological description of the surface processes on cold cathodes.

REFERENCES

1. G. A. Mesyats, *Ectons* (Nauka, Yekaterinburg, 1993), Part 1.
2. S. N. Magonov and M. H. Whangbo, *Surface Analysis with STM and AFM* (Springer-Verlag, Berlin, 1996).
3. G. N. Furseĭ, D. V. Glazanov, L. M. Baskin, *et al.*, Vakuum. Mikroélektron. **26** (2), 89 (1997).
4. L. M. Baskin, G. G. Vladimirov, and V. N. Shrednik, Poverkhnost, No. 7, 67 (1999).
5. T. I. Mazilova, Zh. Tekh. Fiz. **70** (2), 102 (2000) [Tech. Phys. **45**, 243 (2000)].
6. A. Knoblauch, Ch. Miller, and S. Kalbitzer, Nucl. Instrum. Methods Phys. Res. B **139**, 20 (1998).
7. W. P. Dyke, F. M. Charbonnier, R. M. Strayer, *et al.*, Appl. Phys. **31** (5), 58 (1960).
8. M. I. Elinson and G. F. Vasil'ev, *Autoelectron Emission* (Fizmatgiz, Moscow, 1958).
9. Zh. I. Dranova and I. M. Mikhaĭlovskiĭ, Fiz. Met. Metalloved. **31** (5), 1108 (1971).
10. J. Y. Cavaille and M. Drechsler, Surf. Sci. **75**, 342 (1978).
11. P. A. Bereznyak and V. V. Slezov, Radiotekh. Élektron. (Moscow), No. 2, 354 (1972).
12. A. G. Zaluzhnyĭ, Yu. N. Sokurskiĭ, and V. N. Tebus, *Helium in Reactor Materials* (Énergoatomizdat, Moscow, 1988).
13. V. I. Gerasimenko, Zh. I. Dranova, and I. M. Mikhaĭlovskiĭ, Fiz. Tverd. Tela (Leningrad) **25** (8), 2456 (1983) [Sov. Phys. Solid State **25**, 1410 (1983)].
14. B. G. Lazarev, V. A. Ksenofontov, I. M. Mikhaĭlovskiĭ, and O. A. Velikodnaya, Fiz. Nizk. Temp. **24** (3), 272 (1998) [Low Temp. Phys. **24**, 205 (1998)].
15. *Sputtering by Particle Bombardment*, Ed. by R. Behrisch (Springer-Verlag, New York, 1983; Mir, Moscow, 1986), Vol. II.

Translated by P. Pozdeev

Technical Physics Letters, Vol. 27, No. 9, 2001, pp. 792–794. Translated from Pis'ma v Zhurnal Tekhnicheskoĭ Fiziki, Vol. 27, No. 18, 2001, pp. 78–82.

Special Features in the Magnetization of Polycrystals in Alternating Opposite Magnetic Fields

G. A. Markov and Yu. A. Khon

Institute of Strength Physics and Materials Science, Siberian Division, Russian Academy of Sciences, Tomsk, 634055 Russia

Received April 19, 2001

Abstract—When a polycrystalline closed ferrimagnetic core is exposed to opposite ac magnetic fields with equal amplitudes, a nonzero ac magnetic field exists inside the core. As a result, an electric current is induced in a secondary coil wound over the primary one. © *2001 MAIK "Nauka/Interperiodica".*

Polycrystalline ferro- and ferrimagnets are inhomogeneous systems with nonlinear properties. When such a medium is exposed to an external magnetic field with the strength $H = H_1 + H_2$, the resulting magnetic field inside the medium is $B(H) \neq B_1(H_1) + B_2(H_2)$. In the particular case of vectors H_1 and H_2 equal in magnitude and opposite in direction, vector B can be nonzero. If the components H_1 and H_2 vary in time, an alternating magnetic field may appear in the medium as well. This effect does actually exist, as was illustrated by a particular example [1].

A closed ferrimagnetic core was composed of five identical ferrite rings (M600NN-8K 100 × 00 × 10) with a maximum magnetic permeability of 2000. Each ring magnet was 20 mm thick, the inner and outer diameters being 60 and 100 mm, respectively. The primary winding contained $N_1 = 100$ turns of a copper wire with a cross section area of 0.75 mm^2. This winding represented two coils, each of 50 turns; the second coil was wound over the first in the opposite direction. The output ends of the coils were connected together, while the input ends were connected to the voltage source. The total wire length in the primary winding was 32.5 m. The secondary winding, made of the same wire as the primary one and wound over the second coil of the primary winding, contained $N_2 = 50$ turns wound in one direction. The active electrical resistance of the primary winding was $R_1 \approx 0.7\ \Omega$, while that of the secondary coil was half of this value. Signals applied to the primary coil represented current pulses of variable duration, with an amplitude from 100 to 10^5 A.

When a voltage U_1 across the primary winding was below 40 V, no current passed in the secondary winding. When U_1 was increased from 40 to about 100 V, an electric current was detected in the secondary winding. However, no relationship between voltages in the secondary and primary windings (U_2 and U_1, respectively) could be revealed in this interval. For $U_1 \geq 100$ V, the U_2 value was a linear function of U_1. In particular, an ac current with a frequency of 5 kHz and the amplitude of U_1 = 100, 200, 300, 400, 500, 600, 700, 800, and 900 V induced a response signal in the secondary winding with U_2 = 800, 1750, 2500, 3400, 4300, 5250, 6250, 7250, and 8250 V, respectively. As can be seen, the transformation coefficient $K = U_2/U_1$ weakly increases with the voltage in the primary winding. Note that $K > 1$ even for $N_2 = 1$. An increase in the secondary voltage was observed for the ac current frequencies from 10^{-2} Hz to 10^2 MHz. The dependence of the transformation coefficient on the frequency in this range was almost linear.

A qualitative pattern of this phenomenon is as follows. Each grain in a polycrystalline material has its own direction of the magnetic moment. In a nonmagnetic state, there is no long-range order in the orientation of magnetic moments of the grains. In a external magnetic field $\mathbf{H}_1$, the magnetic field in the medium is $\mathbf{B}_1 = \mu_1(H_1)\mathbf{H}_1$. The magnetic permeability μ_1 is determined by the number of grains, the magnetic moments of which make an acute angle with the vector H_1. Let the relative content of such grains per unit volume be η_1. As the field strength H_1 grows, the $H_1\eta_1$ value increases. A change in the orientation of magnetic moments of the grains leads to elastic interactions between these grains As a result, the free energy of a polycrystalline sample acquires, besides the magnetic component, a contribution due this elastic interaction. For brevity, this contribution will be referred to as the elastic energy. A distribution of the magnetic moments in the field $\mathbf{H}_1$ corresponds to a minimum free energy. For an oppositely directed external field $\mathbf{H}_2$, the corresponding internal magnetic field is $\mathbf{B}_2 = \mu_2(H_2)\mathbf{H}_2$. The magnetic permeability μ_2 is determined by the grains, the magnetic moments of which make an acute angle with the vector $\mathbf{H}_2$. The relative content of such grains per unit volume will be denoted $\eta_2(\mathbf{H}_2)$. The corresponding distribution of the magnetic moments in the field $\mathbf{H}_2$ also corresponds to a minimum free energy of

the polycrystal. A homogeneous and isotropic magnet exposed to the fields with $|\mathbf{H}_2| = |\mathbf{H}_1|$ is characterized by $\eta_2 = \eta_1$.

In a polycrystal exposed to the opposite magnetic fields with $H_1 = H_2 = H$, the resulting magnetic field is $B = \Delta\mu H$, where $\Delta\mu = \mu(H)(\eta_1 - \eta_2)$. Thus, the magnetic component of the free energy of the polycrystal depends on the difference $\eta_1 - \eta_2$; when $H = 0$, this difference vanishes and $\eta_1 = \eta_2$. For the H values below a certain threshold H_0, an increase in the elastic energy for $\eta_1 \neq \eta_2$ exceeds the magnetic component of the free energy. Under these conditions, $\eta_1 = \eta_2$ and the medium exhibits no magnetization. When H exceeds H_0, an increase in the elastic energy is compensated by a decrease in the magnetic component of the free energy. As a result, the magnetic moments η_1 of the grains are oriented along $\mathbf{H}_1$, while the moments η_2 align in the $\mathbf{H}_2$ direction. This state of the medium possessing macroscopic magnetization is thermodynamically favorable.

Now let us consider the kinetics of magnetization of a polycrystalline magnet. First, note that the η_1 and η_2 values characterize a long-range order in the distribution of magnetic moments of the grains. Therefore, these quantities can be considered as the order parameters of a given polycrystalline magnet. The kinetic equations for the order parameters are represented by the equations of balance between the numbers of particles (grains) [2, 3]:

$$t_0 \partial\eta_1/\partial t = F_1(\eta_1, \eta_2) + l_0^2 \Delta\eta_1, \quad (1)$$

$$t_0 \partial\eta_2/\partial t = F_2(\eta_1, \eta_2) + l_0^2 \Delta\eta_2, \quad (2)$$

where t_0 is the characteristic time and l_0 is the characteristic length of variation of the order parameter; F_1 and F_2 are the source functions. Taking into account that η_1 and η_2 are small parameters, the source functions can be presented in the form of expansions [3]

$$\begin{aligned} F_1 &= a_1\eta_1 + b_1\eta_1^2 - \eta_1^3 + c\eta_1\eta_2, \\ F_2 &= a_2\eta_2 + b_2\eta_2^2 - \eta_2^3 - d\eta_1\eta_2. \end{aligned} \quad (3)$$

where a_1, b_1, c, a_2, b_2, and d are dimensionless coefficients. Possessing a physical sense, solutions for the order parameters must obey the following conditions: $0 \le \eta_1 \le 1$; $0 \le \eta_2 \le 1$; $\eta_1 + \eta_2 \le 1$. In the opposite alternating magnetic fields, $\Delta\mu = \Delta\mu(t)$ and the frequency of variation of this value is determined by the ac current frequency ω in the primary winding. For $t_0 \ll 1/\omega$, the magnetization of a polycrystal is described by stationary solutions of Eqs. (1) and (2). In this study, the consideration is restricted to this very case.

Magnetization of the medium in the field $\mathbf{H}_1$ is described by Eq. (1) with $c = 0$. Since a long-range order in the distribution of magnetic moments of the grains is established in the field of any strength, the homogeneous stationary solution $\eta_1 = 0$ for $H_1 > 0$ must always be unstable with respect to small perturbations. This takes place for $a_1 \ge 0$. A nonzero stable homogeneous stationary solution is $\eta_{10} = b_1/2 + (b_1/4 + a)1/2$, from which it follows that $0 \le b_1 < 1/2$. For $H_1 \longrightarrow \infty$, the medium exhibits magnetization up to saturation: $\eta_{10} \longrightarrow 1$. Therefore, the coefficient a_1 must be a monotonically increasing function of H_1. Applying the same considerations to the process of magnetization in the field $\mathbf{H}_2$ for $d = 0$, we conclude that $a_2 \ge 0$ and $0 \le b_2 < 1/2$. For a homogeneous isotropic magnet, we should take $a_1 = a_2$ and $b_1 = b_2$.

The coefficients c and d characterize the influence of the elastic interaction between grains on the magnetization of the polycrystal. It is naturally assumed for a homogeneous isotropic magnet that $|c| = |d|$. Since Eqs. (1) and (2) are symmetric with respect to substituting c for $-c$, it is sufficient to consider the region of $c \ge 0$. An analysis of the set of equations $F_1 = F_2 = 0$ shows that no stable homogeneous solutions such that $\eta_{10} - \eta_{20} > 0$ exist for $a \ll c$, which implies that the polycrystalline medium exposed to weak external fields occurs in the initial sate with $\eta_{10} = \eta_{20}$. When $a \approx c$, there is a single homogeneous solution stable with respect to small perturbations, such that $\eta_{10} > \eta_{20} > 0$. In this sate, the magnetization vector is parallel to the field $\mathbf{H}_1$, the difference $\eta_1 - \eta_2 \le 0.1$ and, hence, $\Delta\mu \le 0.1\mu$. The condition $a \approx c$ determines a critical value of the external magnetic field strength. For $a/c \longrightarrow \infty$, we have $\eta_{20} \longrightarrow \eta_{10}$ and $\Delta\mu \longrightarrow 0$, which implies that the magnetization of the medium decreases. Thus, when the voltage applied to the primary winding increases, the $\Delta\mu$ value jumps to a finite level and then monotonically decays. Since the solution $\eta_{20} - \eta_{10} = 0$ is unstable, a transition of the system to the state with $\eta_{10} > \eta_{20} > 0$ is a homogeneous process, which means that the magnetization of the polycrystal in a field with $H > H_0$ occurs spontaneously. Since the magnetic moments of the grains rotate by an angle not exceeding $\pi/2$, the magnetization of the polycrystal in opposite alternating magnetic fields can proceed in a wide range of frequencies ω.

Now let us calculate the transformation coefficient. For certainty, we assume that the first coil in the primary winding and the secondary winding were wound in the same direction. The inductances of the circuits, determined by the numbers of turns and the magnetic permeabilities for the first and second coil are $L_1 = 0$ and $L_2 \sim \mu N_2^2$, respectively. The proportionality factor depends on the system of units and the core geometry. This quantity does not enter into the expression for the transformation coefficient and is not presented here in the explicit form. The mutual induction coefficients of

the coils wound one over another are $L_{12} = L_{21} \sim \Delta\mu N_1 N_2/2$. Ignoring the voltage drop across the primary winding and the resistance of the secondary winding, we obtain

$$U_1 \sim N_1 N_2/2d(\Delta\mu I_2)/dt, \quad (4)$$

$$U_2 \sim -[N_1 N_2/2d(\Delta\mu I_1)/dt + N_2^2 \mu dI_2/dt], \quad (5)$$

where I_1 and I_2 are the currents passing in the primary and secondary windings. For $N_2 \approx N_1$ and $dI_1/dt \approx dI_2/dt$, we have $K \approx \Delta\mu/\mu$. In particular, $\Delta\mu \approx 0.1\mu$ yields $K \approx 10$. Increasing voltage in the primary winding leads to a decrease in $\Delta\mu$ and an increase in K. Note that, for $N_2 \longrightarrow 1$, we always obtain $K > 1$, so that the device developed in [1] is always a step-up transformer. Note also that the relationship $U_2 N_2 = U_1 N_1$ inherent in usual transformers is not valid in the system considered here.

REFERENCES

1. G. A. Markov, RF Patent No. 2119205, MKI S 1 6H 01 F 30/06 (1997), Byull. No. 26 (1998).
2. B. S. Kerner and V. V. Osipov, Usp. Fiz. Nauk **160** (9), 2 (1990) [Sov. Phys. Usp. **33**, 679 (1990)].
3. Yu. A. Khon, Izv. Vyssh. Uchebn. Zaved., Fiz., No. 6, 3 (1999).

Translated by P. Pozdeev

Technical Physics Letters, Vol. 27, No. 9, 2001, pp. 795–797. Translated from Pis'ma v Zhurnal Tekhnicheskoĭ Fiziki, Vol. 27, No. 18, 2001, pp. 83–88.

Current Shutdown in the T-10 Tokamak Studied by Pellet Injection

V. M. Timokhin, V. Yu. Sergeev, and B. V. Kuteev

St. Petersburg State Technical University, St. Petersburg, 195251 Russia

e-mail: timokhin@phtf.stu.neva.ru

Received April 26, 2001

Abstract—Processes accompanying in the tokamak discharge shutdown were studied by injecting a large number of heavy-impurity (KCl) pellets (~10^{19} atoms) into the T-10 tokamak operating in the ohmic regime. A more than twofold drop in the current at an average rate of 12 MA/s was observed, which corresponded to a considerable (exceeding 75%) decrease in the magnetic energy of the plasma column. The observed phenomena showed evidence of the production of runaway electrons during the discharge current drop. © *2001 MAIK "Nauka/Interperiodica".*

Rapid removal of the thermal and magnetic energy from plasmas can be necessary in tokamak reactors in both emergency cases and standard operating regimes [1]. This circumstance accounts for the considerable interest of researchers toward studying theoretical aspects of this problem [2, 3] and conducting experiments using modern setups [4–6]. Previously [7], we reported on the results of injecting KCl pellets containing up to 3×10^{18} atoms, aimed at the discharge shutdown in the T-10 tokamak.

Below, we present preliminary data on the T-10 tokamak plasma behavior in response to the injection of an almost tenfold greater amount of the same heavy impurity (KCl, ~10^{19} atoms), which led to the loss of a considerable part of the discharge current. The experiments were conducted in the ohmic regime on a quasi-stationary stage of discharge with the following parameters (before impurity injection): discharge current, I_p = 280 kA; loop voltage U_l = 1.3 V; toroidal magnetic field B_t = 2.1 T; limiter radius a_L = 0.3 m; temperature at the plasma column center $T_e(0) \sim 1$ keV; volume-averaged electron density $\bar{n}_e \sim 2 \times 10^{19}$ m^{-3}.

The experimental setup was described in detail elsewhere [8]. The impurity (about ten KCl pellets 0.1–0.3 mm in size) was injected downward into the plasma in the direction of the plasma column center at a velocity of V_p = 100–150 m/s. The pellets evaporated on the periphery of the plasma column, at a small radius of $a_L \leq 20$ cm.

Figure 1 shows time evolution of the main diagnostic signals measured under typical discharge conditions. All signals are normalized to the maximum values of the corresponding parameters in the time interval studied. The electron temperature at a quarter of the small radius $T_e(a_L/4)$ was measured by a heterodyne detector of the second-harmonic electron cyclotron resonance (ECR) radiation. The soft X-ray radiation (SXR) detector signal represented emission along the central chord. Other signals were obtained from hard X-ray radiation (HXR) receiver, magnetohydrodynamic (MHD) probes, and a peripheral channel of a fast bolometric array (Bol).

The impurity was injected beginning with the time instant of 812.6 ms, as was immediately reflected by the

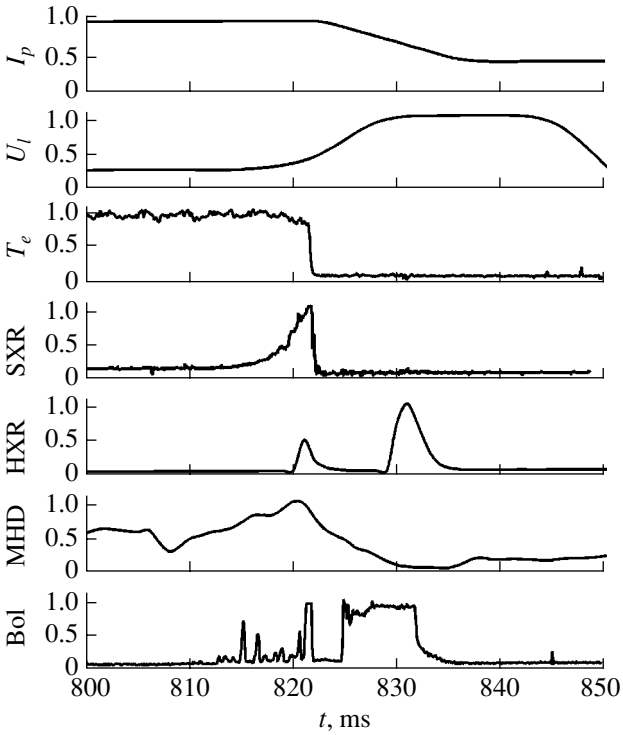

Fig. 1. Time variation of the main plasma parameters in response to the KCl pellet injection into a tokamak discharge (shot #27528).

1063-7850/01/2709-0795$21.00 © 2001 MAIK "Nauka/Interperiodica"

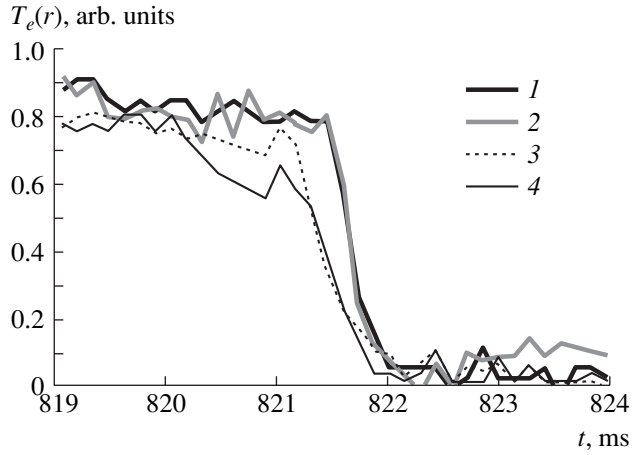

Fig. 2. Time evolution of the electron temperature profile after KCl injection into a tokamak discharge (shot #27528). The measurements were performed at r = 4.6 (*1*), 10.7 (*2*), 15.9 (*3*), and 18.7 cm (*4*).

bolometer signal. The bolometer output signal peaks correspond to the instants of vaporization and ionization of individual pellets. The parameters of plasma varied rather insignificantly until about 821 ms, when most of the impurity was injected. At this time instant (821.2 ms), the bolometer signal intensity reached values close to maximum and remained on this level over about 0.5 ms. Simultaneously, the electron temperature exhibited a sharp drop, which was accompanied by an analogous drop of the SXR signal. The electron temperature decayed to almost zero and stayed on this level until the end of the process. Thus, the time interval between 813 and 821 ms corresponds to the thermal energy removal from the plasma (see also [7]).

An analysis of evolution of the electron temperature profile in the sharp decay stage (Fig. 2) suggests that the impurity rapidly reaches the central region of the plasma column. This is consistent with the almost simultaneous drop of the electron temperature in all channels. Estimates showed that the transport coefficients increased in this stage by at least one order of magnitude as compared to the quasi-stationary values ($D \sim 1$ m^2/s). This result confirmed the conclusion [7] that a disturbance in the impurity transfer coefficient depends on the amount of injected substance.

After termination of the stage of the thermal energy removal from the discharge, the system exhibits the stage of the discharge current decay [7]. A decrease in the current is accompanied by an increase in the loop voltage. The current begins to drop at approximately 822 ms and decays over about the next 15 ms at an average rate of 12 MA/s to reach a level of ~100 kA (Fig. 1). The 2.5-fold drop in the current corresponds to a more than 75% decrease in the energy of the poloidal magnetic field.

During the time interval from 825 to 832 ms, the bolometer signal is approximately constant and close to the maximum level. In this stage, the magnetic field energy of the current is removed through reradiation by the impurity, which is evidenced by a decrease in the current. Note the low level (two–three times the quasi-stationary value) of the bolometer signal at the onset of the current drop (822–825 ms). We may suggest that the energy is pumped from the current to the runaway electrons (probably, by the mechanism of avalanche multiplication during close collisions [9]), followed by reradiation in the wavelength range not monitored by the X-ray detectors employed (<1 MeV).

In this context, a characteristic feature is the HXR emission at 830–835 ms. We relate this signal to the fact that the energies of runaway electrons reach a level (1–3 MeV) detectable by the HXR sensor employed. Note also the preceding HXR pulse at 820–822 ms (immediately before the onset of the sharp drop in the electron temperature), which is probably related to the loss of the population of runaway electrons existing in the discharge before impurity injection. These losses may be caused by a sharp change of conditions in the plasma or by an increase in the plasma MHD activity. The latter possibility is confirmed by the coincidence of the time instants corresponding to the first HXR pulse and the MHD activity peak. During the second HXR pulse, the MHD signal is minimum and the mechanism of the runaway electron losses is apparently different.

A smooth monotonic decay of the bolometer current observed after 832 ms on the background of still decaying current can be explained by a decrease in the plasma energy density, by a diffusion loss of the radiating impurity on the walls, and by the continuing production of runaway electrons.

The current ceases to decrease at 840 ms on reaching a level of 100 kA, after which the discharge attains a new quasi-stationary state with a minimum energy density. Termination of the current drop is probably related to the diffusion loss of impurity from the plasma. This is evidenced by a decrease in the loop voltage at a constant current observed in the final stage of evolution. It is also not excluded that the main part of the discharge current in this stage is carried by the runaway electrons. Note that saturation of the loop voltage in the time period from 835 to 840 ms is obviously determined by overloading of the analog-to-digital converter (ADC) registers. A maximum signal detected at the output of the smoothening filter with a time constant of 30 ms corresponds to a loop voltage of about 6 V.

The results of experiments with a large amount of heavy impurity (KCl) injected into the tokamak plasma demonstrated, besides the complete removal of the thermal plasma energy component, the removal of more than 75% of the poloidal magnetic field energy. We observed two pulses of hard X-ray radiation in the stage of the discharge current decay, which is evidence of intensive runaway electron production in the course of the discharge quenching. It is important to note the

rapid impurity penetration into the central regions of the plasma column.

Acknowledgments. The authors are grateful to the staff of T-10 for their help in experiments and the opportunity to work with the data base.

This work was supported by the Ministry of Science and Technology of the Russian Federation "Post-Graduate Support" Program (project no. 375), INTAS Foundation (grants 95-0575 and 97-11004), and the Russian Foundation for Basic Research (project no. 99-02-1764).

REFERENCES

1. *Physics and Plasma Operation Studies*, ITER Report S CA4 RE2.
2. B. V. Kuteev, V. Yu. Sergeev, and S. Sudo, Nucl. Fusion **10**, 1167 (1995).
3. S. Putvinski, N. Fujisawa, D. Post, *et al.*, J. Nucl. Mater. **241**–**243**, 316 (1997).
4. G. Pautasso, K. Buchl, J. C. Fuchs, *et al.*, Nucl. Fusion **36**, 1291 (1996).
5. R. Yoshini, S. Tokuda, and Y. Kawano, Nucl. Fusion **39**, 151 (1999).
6. S. C. Jardin, G. L. Schmidt, E. F. Fredrickson, *et al.*, Nucl. Fusion **40**, 923 (2000).
7. V. M. Timokhin, V. Yu. Sergeev, and B. V. Kuteev, Fiz. Plazmy **27** (3), 1 (2001) [Plasma Phys. Rep. **27**, 181 (2001)].
8. S. M. Egorov, B. V. Kuteev, I. V. Miroshnikov, *et al.*, Nucl. Fusion **32**, 2025 (1992).
9. Yu. A. Sokolov, Pis'ma Zh. Éksp. Teor. Fiz. **29**, 244 (1979) [JETP Lett. **29**, 218 (1979)].

Translated by P. Pozdeev

Technical Physics Letters, Vol. 27, No. 9, 2001, pp. 798–800. Translated from Pis'ma v Zhurnal Tekhnicheskoĭ Fiziki, Vol. 27, No. 18, 2001, pp. 89–94.

On the Mechanism of the Electron-Impact Excitation of $4d^95s^2\ ^2D_{5/2,\,3/2}$ Upper Laser Levels in Cadmium Ions

A. N. Gomonai and A. I. Imre

Institute of Electron Physics, National Academy of Sciences of Ukraine, Uzhgorod, Ukraine

e-mail: dep@mail.uzhgorod.ua

Received March 20, 2001

Abstract—The energy dependence of the effective cross sections for the electron-impact excitation of $4d^95s^2\ ^2D_{5/2,\,3/2} - 4d^{10}5p\ ^2P^0_{1/2,\,3/2}$ laser transitions in cadmium ions was studied by a high-precision spectroscopic technique using crossed electron and ion beams. The absolute effective cross sections for the laser line excitation at λ = 441.6 and 325.0 nm have the peak values 2.5×10^{-16} and 1.3×10^{-16} cm^2, respectively. It is shown that population of the $4d^95s^2\ ^2D_{5/2,\,3/2}$ upper laser levels by the electron impact on cadmium ions in the $4d^{10}5s\ ^2S_{1/2}$ ground state takes place predominantly due to the resonance processes; that is, it proceeds via atomic and ionic autoionization states. © *2001 MAIK "Nauka/Interperiodica".*

Among metal-vapor lasers, devices based on the helium–cadmium mixture, offer one of the most stable types widely used in a number of applications. Using blue (λ = 441.6 nm) or ultraviolet (325.0 nm) emission lines of cadmium ions, it is possible to obtain stable lasing at a low excitation threshold [1]. The upper and lower levels in these laser transitions correspond to the $4d^95s^2\ ^2D_{5/2,\,3/2}$ and $4d^{10}5p\ ^2P^0_{1/2,\,3/2}$ excited states of cadmium ions. The most probable mechanism of lasing for both lines is believed to involve excitation of the upper level due to the energy transferred from metastable He (2^3S_1) atoms to cadmium ions in the course of the Penning ionization process [2]. Besides this mechanism, the process of charge exchange during collisions of Cd atoms with He^+ or He_2^+ ions and the excitation of $4d^95s^2\ ^2D_{5/2,\,3/2}$ levels during the electron-impact Cd *d*-shell ionization were also taken into consideration [3].

However, Goto *et al*. [4–6] suggested that the dominating mechanism of the upper laser level population is related to a two-step process. In the first step, cadmium atoms are ionized by the electron impact, and in the second step, the resulting ions are excited from the $4d^{10}5s\ ^2S_{1/2}$ ground state to the long-living $4d^95s^2\ ^2D_{5/2,\,3/2}$ states. The energy dependence of the effective cross sections for excitation of the 441.6 and 325.0 nm laser lines and the 214.4 and 226.5 nm resonance lines in cadmium ions was studied by optical methods in the crossed beams featuring electron–ion collisions [5, 6]. These measurements gave enormously large values of the absolute excitation cross sections for the 441.6 and 325.0 nm laser lines (5×10^{-15} and 3×10^{-15} cm^2, respectively), which were about two times greater than the values for the resonance lines. This was interpreted as evidence in favor of the two-step excitation of the upper laser levels being the dominating mechanism of generation in lasers employing helium–cadmium mixtures.

It must be noted, however, that the experiments reported in [5, 6] were conducted in a narrow energy interval (7–18 eV) at a large energy scan step (0.5–1 eV) and were characterized by large errors (±45%); the measurements used electron beams with a considerable energy scatter and (what we believe to be the most significant disadvantage) were performed with high anode voltages (~100 V) in the ion source. The last circumstance leads to the effective excitation of Cd atoms in the ion source, with the formation of cadmium ions in the long-living $4d^95s^2\ ^2D_{5/2,\,3/2}$ states (with the lifetimes τ = 830 and 300 ns). Not experiencing radiative decay during transit, these ions arrive at the collision zone in the excited state. Although the fraction of such excited ions relative to particles in the ground state is small, the former ions considerably increase the overall radiation background. This may significantly influence the precision of the useful signal separation and the accuracy of the effective excitation cross section determination.

In this context, it was of interest to study the energy dependence of the effective electron-impact excitation cross sections for the 441.6 and 325.0 nm laser lines (corresponding to the transitions from $4d^95s^2\ ^2D_{5/2,\,3/2}$ to $4d^{10}5p\ ^2P^0_{1/2,\,3/2}$ resonance levels of cadmium ions) at a higher precision in order to elucidate the mechanism of population of the upper laser levels in helium–cadmium lasers. Below, we report on the results of such an investigation.

The experimental setup used in our experiments was described in detail elsewhere [7]. The ion source, oper-

ating in a low-voltage discharge regime, produced a beam of ions with an energy of 640 eV and a total ion current of (6–8) × 10^{-7} A. The discharge voltage ($U_d \le$ 12 V) was selected so as to be definitely below the excitation energy (17.6 eV) of the lowest long-living $4d^9 5s^2\ ^2D_{5/2,\,3/2}$ states of cadmium ions. This significantly reduced the radiation background related to the radiative decay of these states. A three-anode electron gun formed a ribbon electron beam with an energy of 7–50 eV, a beam current of 7–12 × 10^{-5} A, and an energy inhomogeneity (full width at half maximum of the electron energy distribution curve) of $\Delta E_{1/2}$ = 0.4 eV. The electron and ion beams crossed at right angle in the collision zone in a vacuum of 10^{-8} Torr.

The spectral analysis of the radiation was performed with a large-aperture diffraction monochromator of the MDR-2 type (1200 lines/mm) with a reciprocal linear dispersion of $d\lambda/dl \sim 2$ nm/mm. The radiation was detected by an FEU-140 ("Foton") cooled photoelectron multiplier with a dark background count level of 1–2 cps. The useful signal (0.5–3 cps) was accumulated in the cycle regime over a period of 600–800 s and separated from background using a lock-in technique based on the modulation of both beams by rectangular pulses shifted by 1/4 of the modulation period. The signal to background level ratio varied from 1/15 to 1/30.

The process of experimental data accumulation and processing was automated using a system implementing CAMAC moduli controlled by a personal computer. The system ensured controlled variation of the electron acceleration voltage, exposure time at each energy point, and the total number of experimental point and measurement cycles as well as the monitoring and recording of the electron and ion beam currents, photomultiplier response signal, and the number of pulses in the modulation quarter-periods. The electron energy scale was calibrated to within ±0.1 eV using a threshold region of the cadmium intercombination line excitation at λ = 326.1 nm, for which the spectroscopic excitation threshold is known with high precision.

Our detailed investigation of the electron-impact excitation of the laser transitions from $4d^9 5s^2\ ^2D_{5/2,\,3/2}$ levels of cadmium ion, with the emission measured at λ = 441.6 and 325.0 nm for the primary electron beam energy varied from 7 to 50 eV, included (i) measurement of the energy dependence of the relative effective excitation cross sections; (ii) study of the laser radiation energy transfer from the observation region, depending on the electron state lifetime, ion velocity, and slit width in the direction of ion motion; and (iii) determination of the absolute excitation cross sections. The polarization of the radiation was not taken into account. Calculations showed that the radiative transitions with λ = 441.6 and 325.0 nm take place only in 16 and 38% of ions in the collision zone. The maximum spectral sensitivity of the measuring equipment (2 × 10^{-4} count/photon) was observed at 380 nm.

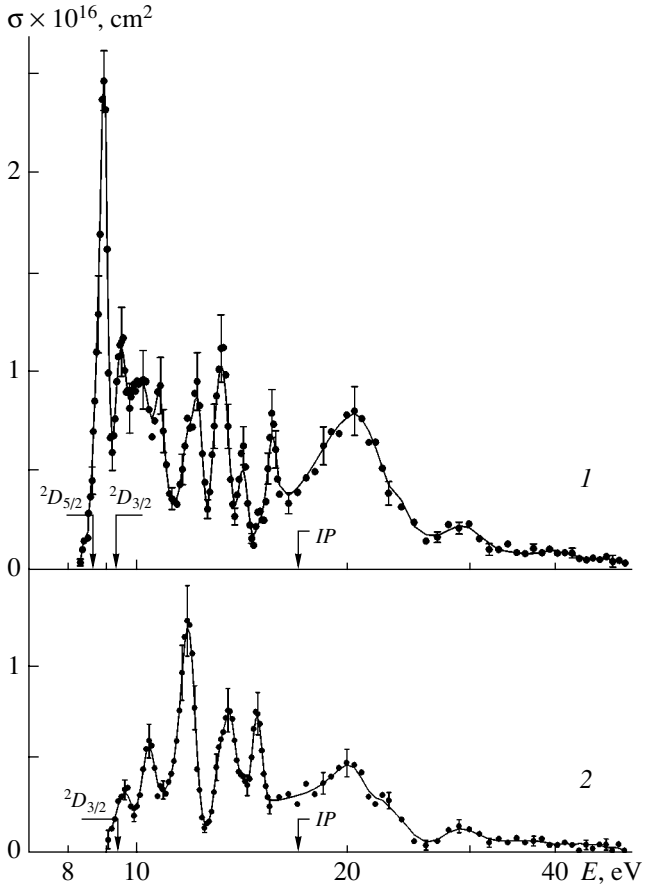

The energy dependence of the absolute effective cross sections for excitation of the helium–cadmium laser lines with (*1*) λ = 441.6 nm ($4d^9 5s^2\ ^2D_{5/2} \longrightarrow 4d^{10} 5p\ ^2P^0_{3/2}$ transition) and (*2*) λ = 325.0 nm ($4d^9 5s^2\ ^2D_{3/2} \longrightarrow 4d^{10} 5p\ ^2P^0_{1/2}$ transition); IP is the ionization potential.

The experimental results are presented in the figure. The vertical bars at the experimental points indicate mean-square errors (±15–20%) of the relative measurements. The absolute values of the effective excitation cross sections were determined with an error not exceeding ±15%.

As can be seen from the presented data, the excitation functions reveal a clearly pronounced structure related to the capture of primary electrons by cadmium ions with the formation of atomic ($4d^9 nln_1l_1n_2l_2$) and ionic ($4d^9 nln_1l_1$) autoionization states of these ions. The electron decay of these states (direct or via cascade transitions) leads to a considerable additional population of the $4d^9 5s^2\ ^2D_{5/2,\,3/2}$ levels. Therefore, the resonance excitation dominates in this process and suppresses direct excitation of these levels. Note that the resonance excitation dominates in the entire range of electron energies studied rather than in a narrow near-threshold region.

The maximum effective electron-impact excitation cross sections of the and $4d^9 5s^2\ ^2D_{5/2} \longrightarrow 4d^{10}5p\ ^2P^0_{3/2}$ and $4d^9 5s^2\ ^2D_{3/2} \longrightarrow 4d^{10}5p\ ^2P^0_{1/2}$ laser transitions are 2.5×10^{-16} and 1.3×10^{-16} cm^2, respectively, which amounts to approximately one-third of the maximum cross sections for excitation of the $4d^{10}5p\ ^2P^0_{1/2, 3/2}$ resonance doublet components studied in [8] and 1/20 of the corresponding values reported in [5, 6]. The total electron-impact excitation cross section for the laser transitions studied agrees well with the results of the *R*-matrix calculations of the excitation cross sections of the $4d^{10}5s\ ^2S$–$4d^9 5s^2\ ^2D$ transition [9]. At present, these calculations provide a most adequate description of the electron scattering from complex multicomponent systems such as the cadmium ion.

In concluding, it must be noted that population of the $4d^9 5s^2\ ^2D_{5/2, 3/2}$ upper laser levels upon the electron impact on cadmium ions in the ground state proceeds predominantly at the expense of resonance processes, that is, via atomic and ionic autoionization states. In a plasma, the resonance contribution to the effective cross sections of these levels is significantly averaged over the Maxwell distribution of the electron energies, which may considerably decrease the values (~10^{-17} cm^2). This indicates that a two-step process involving the cadmium atom ionization and the $4d^9 5s^2\ ^2D_{5/2, 3/2}$ ion level excitation from the ground state by the electron impact, apparently cannot be considered (because of a low efficiency of the second stage) as the dominating mechanism of the excited level population in helium–cadmium lasers, as was proposed by Goto *et al.* [4–6].

REFERENCES

1. *Handbook of Lasers*, Ed. by A. M. Prokhorov (Sov. Radio, Moscow, 1978), Vol. 1.
2. S. V. Makarov, Yu. N. Novoselov, and V. V. Osipov, Kvantovaya Élektron. (Moscow) **17** (8), 974 (1990).
3. R. S. Jensen and W. R. Bennet, IEEE J. Quantum Electron. **QE-4** (5), 356 (1968).
4. T. Goto and T. Sakurai, J. Phys. D **15** (12), 2413 (1982).
5. K. Hane, T. Goto, and S. Hattori, Phys. Rev. A **27** (1), 124 (1983).
6. K. Hane, T. Goto, and S. Hattori, J. Phys. B **16**, 629 (1983).
7. A. N. Gomonai and A. I. Imre, Ukr. Fiz. Zh. **41** (11-12), 1032 (1996).
8. A. N. Gomonai, A. I. Imre, V. S. Vukstich, *et al.*, in *Contributed Papers of the XXI International Conference on the Physics of Electronic and Atomic Collision, XXI ICPEAC, Sendai, Japan, 1999*, p. 342.
9. O. I. Zatsarinnyi and L. A. Bandurina, Opt. Spektrosk. **89** (4), 546 (2000) [Opt. Spectrosc. **89**, 498 (2000)].

Translated by P. Pozdeev